Influences of Mesoscale Variations in Land Surface Albedo on Large-Scale Averaged Heat Fluxes

by
Humberto Rodriguez

Department of Atmospheric Science
Colorado State University
Fort Collins, Colorado

Roger A. Pielke, P.I.
NSF Grant #ATM-8915265

Colorado State University

Department of Atmospheric Science

Paper No. 514

INFLUENCE OF MESOSCALE VARIATIONS IN LAND SURFACE ALBEDO ON LARGE-SCALE AVERAGED HEAT FLUXES

Humberto Rodriguez

Department of Atmospheric Science
Colorado State University
Fort Collins, Colorado
Fall 1992

Atmospheric Science Paper No. 514

ABSTRACT

INFLUENCE OF MESOSCALE VARIATIONS IN LAND SURFACE ALBEDO ON LARGE-SCALE AVERAGED HEAT FLUXES

Real albedo data from a region of 100×100 km^2 located in the Coconino Plateau in northern Arizona have been used in RAMS to simulate the effects that mesoscale variations in land surface albedo have on the domain-averaged vertical heat fluxes. GOES-6 VIS satellite imagery data were used to obtain two samples of albedo data, one for the winter (10 February 1986) and one for the summer (7 June 1986). A total of 8 3-D simulations were carried out using RAMS, 4 runs for the winter and 4 for the summer. For each season, two albedo variations were set up in the model: (i) Mean albedo depending on time but with no spatial variation $[\overline{A}(t)]$, and (ii) Albedo varying as a function of space and time $[A(x,y,t)]$, that is, the actual albedo. Moreover, the effect of these albedos was also simulated over two topography types: (i) A flat terrain (NOTOPO), and (ii) Complex terrain (TOPO), or real topography. The grid spacing used in the domain was 1 km ($\Delta x = \Delta y = 1$km) and no synoptic wind was assumed.

In this study, the main attributes of shapes, vertical distribution and time of maximum occurrence of the vertical fluxes are discussed. In addition, quantitative values of the heat fluxes are given for the entire domain for each season and study case. The three-dimensional model results showed that for both types of albedo and terrain variations, the production of the domain-averaged mesoscale vertical heat flux ($< w'\theta' >_D$) and the domain-averaged subgrid-scale vertical heat flux ($< \overline{w''\theta''} >_D$) both had important contributions to the sensible heating of the atmosphere. However, as main features, it was found that: (i) The TOPO cases (complex terrain) for both types of albedo variations

$[\overline{A}(t)$ *and* $A(x,y,t)]$ reached the greatest values of heat flux. (*ii*) The terrain and albedo variations, independently produce mesoscale vertical heat fluxes that are on the same order, but at higher model levels, than simulated for the turbulent heat fluxes. (*iii*) The topography effects working together with the albedo variability enhance the production of heat fluxes, and (*iv*) The profiles of the mesoscale heat fluxes ($< w'\theta' >_D$) and subgrid-scale heat fluxes ($< \overline{w''\theta''} >_D$) showed similar shapes but with different vertical structure.

The results demonstrated that as consequence of the albedo and terrain variability a thermal-forced mesoscale circulation was generated which in turn contributed in the transfer of surface heat fluxes to the atmosphere. Therefore, the inclusion of the albedo discontinuities and terrain variability into the general circulation models as well as into the operational numerical weather prediction model is suggested in order to improve results since these models do not yet resolve these features.

Humberto Rodriguez
Department of Atmospheric Science
Colorado State University
Fort Collins, Colorado 80523
Fall 1992

ACKNOWLEDGEMENTS

I would like to thank several people who helped me during the course of this research. First of all, I express thanks to my Committee members, Professors Roger A. Pielke, Thomas H. Vonder Haar, and Ingrid Burke for their advice and helpful comments to improve this work. For Professor Roger A. Pielke, who was my adviser, special recognition and my sincere gratitude for his support and counsel which were very important to finish this research and my program in the Department of Atmospheric Science at CSU. Also, I would like to thank Joseph Eastman for his help and assistance in the use of the RAMS model and some programs that were used in this work. Thanks to Nan McClurg who gave me the facilities to work at CIRA Ground Station. Kelly Dean is thanked for providing the GOES-6 VIS satellite pictures and for his help in obtaining the albedo maps. The help of Robert Walko in the computer tasks in RAMS is also recognized and thanked. G. Garrett Campbell and Roger Stocker are acknowledged for their important comments and discussions about the albedo data.

In México, there are also many people who encouraged me and helped me during the course of my graduate study at CSU. I am very grateful to the people of Servicios a la Navegación en el Espacio Aéreo Mexicano (SENEAM) where the Aviation Weather Service (Centro de Análisis y Pronóstico-CAP) is located for their support. In addition, I would like to thank The Instituto Politécnico Nacional (IPN) and Cecyt $N°10$ (Area de Meteorología) for their help. I express my thanks to all people in México who backed me and made possible traveling to USA, special recognition to Ing. Roberto Kobeh González and Ing. Luis J. García Pérez, main executives of SENEAM for supporting and believing in me.

Also, I am indebted to my family and friends who supported me during the course of my program at CSU. My respect and love to my wife Elvia, my daughters Angélica

and Carmela, and my son Sabas for their understanding. Thanks to my parents Celia and Juan, and to my mother-in-law Soledad for their prayers and love. I express also sincere thanks to Abraham González Ruiz who is my "compadre" and my best friend for his help. I appreciated the kindness of Dr. Joseph Smagorinsky, Dr. Julian Adem, Dr. Ernesto Jauregui, and Dr. Enrique Camarillo who gave me recommendation letters to CSU and valuable advice.

Finally, special recognition to Pielke's Administrative Staff: Dallas McDonald, Bryan Critchfield, and Tony Smith who helped me by typing some papers and assisted me with the LATEX program. In particular, the help of Dallas McDonald is very appreciated for typing the final form of this thesis. Many of the computer calculations and plots were performed using the capabilities of the National Center for Atmospheric Research (NCAR). This research was supported by the National Science Foundation under Grant # ATM-8915265.

TABLE OF CONTENTS

1 INTRODUCTION **1**

2 BRIEF LITERATURE REVIEW **4**

3 DATA ANALYSIS **17**
3.1 Study Region and Time of Year 17
3.2 The Albedo Data 20
3.2.1 Introduction 20
3.2.2 The Satellite Data 21
3.2.3 Methodology 21
3.2.4 Summer and Winter Albedo Statistics 27

4 THE RAMS SIMULATIONS **33**
4.1 The CSU RAMS Model 33
4.2 Evaluation of Mesoscale and Subgrid Scale Heat Fluxes 33
4.2.1 RAMS Initialization and Model Set Up 36
4.3 The 3-D Simulations 36
4.3.1 The Horizontal Circulation ($\vec{V}_h$) 38
4.3.2 The Vertical Velocity (w) 39
4.3.3 The Z_i of the PBL 46

5 DISCUSSION OF VERTICAL HEAT FLUXES **53**
5.1 Vertical Heat Fluxes: Winter Case 53
5.2 Vertical Heat Fluxes: Summer Case 57

6 SUMMARY AND CONCLUSIONS **62**
6.1 Summary 62
6.2 Conclusions 63
6.3 Future Work 63

REFERENCES **64**

LIST OF FIGURES

2.1 Diagram indicating the major components of the Manabe's model. 6
2.2 Diurnal variation of the energy fluxes at the surface as computed at a grid point in a 10-level atmospheric model during a 24-hour forecast for 21 August 1965. 8
2.3 Wet and dry soil albedo vs. zenith angle for the four experiments carried out on May, July, September, and December 1973 at Phoenix, Arizona. 9
2.4 Predicted sensible heat fluxes (W m^{-2}) as a function of soil type. 11
2.5 Comparison between simulated (solid lines) and observed (dashed lines) surface of sensible (a), and latent (b) heat fluxes over the Landes forest on June 16. 14
2.6 The Bowen ratio at the ground for dry and moist atmosphere profiles 16

3.1 The region labeled A_1 is the study site. It covers an area of 100×100 km^2. . . 18
3.2 (a) Topography of northern Arizona and southern Utah, and (b) terrain characteristics of the study site (A_1). 19
3.3 GOES-6 visible image for 10 February 1986 at 1800 UTC. 22
3.4 GOES-6 visible image for 7 June 1986 at 1800 UTC. 23
3.5 Geometrical configuration for earth, sun, and satellite. 25
3.6 Surface albedo distribution in the rectangular area in Figure 3.1 for 10 February 1986. 29
3.7 Surface albedo distribution in the rectangular area in Figure 3.1 for 7 June 1986. 30

4.1 Subjective analysis of streamlines of the horizontal flow ($\vec{V}_h$) for the winter case at 1300 LST at height $Z = 28.3$ m for area A_1. 40
4.2 Subjective analysis of streamlines of the horizontal flow ($\vec{V}_h$) for the summer case at 1300 LST at height $Z = 28.3$ m for area A_1. 41
4.3 Maximum intensities of $\vec{V}_h$ at levels $Z_1 = 60$ m and $Z_7 = 1548$ m for area A_1. . 42
4.4 East-west cross sections of w (along 35.46°N) for the winter case at 1300 LST for area A_1. 44
4.5 East-west cross sections of w (along 35.46°N) for the summer case at 1300 LST for area A_1. 45
4.6 Maximum intensities of vertical velocity (w) at model level $Z_1 = 60$ m for area A_1. 47
4.7 Maximum intensities of vertical velocity (w) at model level $Z_6 = 1191$ m for area A_1. 48
4.8 Maximum intensities of vertical velocity (w) at model level $Z_8 = 1995$ m for area A_1. 49
4.9 Time cross sections of the maximum average Z_i for the entire domain (A_1). . . 51

5.1 Time cross sections of the domain-averaged mesoscale vertical heat fluxes and domain-averaged subgrid-scale heat fluxes for area A_1 for the winter case at model levels $Z_1 = 60$ m, $Z_2 = 135$ m, $Z_3 = 346$ m, $Z_4 = 676$ m, $Z_5 = 904$ m, $Z_6 = 1191$ m, and $Z_7 = 1548$ m. 55
5.2 Time cross sections of the domain-averaged mesoscale vertical heat fluxes and domain-averaged subgrid-scale heat fluxes for area A_1 for the winter case at model levels $Z_1 = 60$ m, $Z_2 = 135$ m, $Z_3 = 346$ m, $Z_4 = 676$ m, $Z_5 = 904$ m, $Z_6 = 1191$ m, and $Z_7 = 1548$ m. 56
5.3 Time cross sections of the domain-averaged mesoscale and subgrid-scale vertical heat fluxes for the summer case for area A_1 at model levels $Z_1 = 60$ m, $Z_2 = 135$ m, $Z_3 = 346$ m, $Z_4 = 676$ m, $Z_5 = 904$ m, $Z_6 = 1191$ m, and $Z_7 = 1548$ m. 58
5.4 Time cross sections of the domain-averaged mesoscale vertical heat fluxes and the domain-averaged subgrid-scale heat fluxes for area A_1 for the summer case at model levels $Z_1 = 60$ m, $Z_2 = 135$ m, $Z_3 = 346$ m, $Z_4 = 676$ m, $Z_5 = 904$ m, $Z_6 = 1191$ m, and $Z_7 = 1548$ m. 60

LIST OF TABLES

2.1 Average albedos (A) for various terrestrial surfaces and clouds determined by satellite TIROS. 5

3.1 Surface albedo statistics for the rectangular area in Figure 3.1 (Utah and Arizona regions) for 10 February 1986. 28
3.2 Surface albedo statistics for the rectangular area in Figure 3.1 (Utah and Arizona regions) for 7 June 1986. 28
3.3 Surface albedo statistics for area A_1, 10 February 1986. 31
3.4 Surface albedo statistics for area A_1, 7 June 1986. 31

4.1 Model characteristics used in RAMS for the study site A_1. 37
4.2 Simulations performed in RAMS for the study site A_1. 37
4.3 Absolute maximum speeds of $\vec{V}_h$ over the entire domain for the winter and summer cases for area A_1, at model levels $Z_1 = 60$ m and $Z_7 = 1548$ m. . . 39
4.4 Absolute maximum speeds of w for the entire domain (A_1) for the winter and summer cases, and heights and time at which they were reached. 50
4.5 Absolute maximum values of $< Z_i >_D$ for the entire domain (A_1) for winter and summer cases, and time at which they occurred. 52

5.1 Absolute maximum values of the domain-averaged vertical heat fluxes ($< w'\theta' >_{D_{max}}$) for the winter and summer cases over the entire domain (A_1). 61
5.2 Absolute maximum values of the domain-averaged subgrid-scale heat fluxes ($< \overline{w''\theta''} >_{D_{max}}$) for the winter and summer cases over the entire domain (A_1). 61

Chapter 1

INTRODUCTION

On the average, approximately 50% of the solar radiation that reaches the top of our atmosphere reaches the surface of the earth, and about 25% of the incident radiation is absorbed by clouds and the atmosphere (Perkey, 1988). Consequently, we can consider the atmosphere as a fluid that is being warmed from below instead of a fluid being warmed by direct absorption of solar radiation. Thus, the atmosphere gets heat from the earth's surface to warm its lower layers. When solar radiation reaches the surface, several physical processes take place which affect the energy balance of the surface. For instance, some regions can absorb or reflect more solar energy than others, due to albedo differences of those regions.

The albedo of the earth's surface (A) is defined as the ratio of reflected solar energy (I_r), to incident solar energy (I_o). That is:

$$A = \frac{I_r}{I_o} \tag{1.1}$$

This relationship must be taken into account when the heat budget of the earth is assessed since it determines the incoming solar energy available to heat the surface layer (Kuhn and Suomi, 1958). In mesoscale meteorology, albedo usually refers to the reflectance of solar radiation (Pielke, 1984), both direct and diffuse. Albedo has large spatial and temporal variability. For instance, fresh snow can reflect up to 95% of the solar radiation that reaches it, whereas dark soil reflects only 5% (Pielke, 1984). The earth and its atmosphere have a combined albedo averaging 30% (Ahrens, 1982). Albedo variability takes place because each element on earth's surface has an albedo value that depends on its own characteristics. Also, it depends on the angle at which solar radiation

is incident on the surface and the slope orientation of the surface (Pielke, 1984; Lipton, 1991). Albedo variability has an important impact on weather and climate and it must be taken into account in General Circulation Models (GCM) (Pielke et al., 1991).

During the Earth Radiation Budget Science 1978 workshop (NASA Conference Publication 2100, 1979), it was pointed out that variations in surface albedo are associated with changes in vegetative cover and wetness. It was also suggested that albedo values, or absorbed solar radiation for clear sky conditions can be used to monitor various spatial and temporal variations in the surface energy budget over land areas. Lately many modeling studies have provided convincing evidence that changes in landscape have a major impact on land-atmosphere interactions and on climate as well. For instance, changes in vegetation (most areas are vegetated) arise as one of the most important components in the process since vegetation plays an important role in the hydrologic cycle, which in turn is related to climate (Anthes, 1984; Segal et al., 1988 and 1989; Avissar and Pielke, 1989; Pielke et al., 1990; Pielke and Avissar, 1991). When the earth's surface characteristics are modified, albedo is also modified and the fluxes of energy toward lower troposphere are necessarily affected.

This work demonstrates the roles that albedo variability has in the atmospheric response, such as producing variations in sensible heat flux which can result in horizontal mesoscale circulation due to resultant large horizontal temperature variations in the boundary layer. To do this, two cases are studied; one in the winter and one for summer. Albedo values were obtained using 1 km pixel visible (VIS) imagery data from GOES for an area of 100×100 km^2 of northern Arizona. The methodology for obtaining albedo values and the analysis of albedo are explained in Chapter 3, where the bidirectional reflectance model derived from GOES (Minnis and Harrison, 1984) were used. Chapter 4 deals with the 3-D simulations that were carried out using the Regional Atmospheric Modeling System (RAMS) developed at CSU. In this chapter, four sets of simulations are presented. Each set contains winter and summer cases in which two runs were done, one using real topography data and the other assuming a flat terrain. In two experiments the albedo was set up as function of time taking into account its mean value $[\overline{A}(t)]$. In

the other experiments the albedo was set up in RAMS as a function of space and time $[A(x, y, t)]$. Therefore, a total of 8 runs were performed, 4 for summer and 4 for winter. Also, in Chapter 4 the vertical velocity (w) fields and the plots of the horizontal wind ($\overline{V}_h$) are displayed. In Chapter 5 the vertical heat fluxes are discussed and finally, in Chapter 6 the summary and conclusions are given.

Chapter 2

BRIEF LITERATURE REVIEW

Certainly, there are many papers that demonstrate the importance of albedo as a variable that contributes to weather and climate in an important way (Fritz, 1948; Kung, 1964; Otterman, 1974, 1977, 1981, 1984, 1985; Idso et al., 1975; McCumber and Pielke, 1981; Pielke et al., 1990, Bastable et al., 1992). There is interest in obtaining accurate measurements of this variable. For instance, Richardson (1930) using a photometer to make measurements of the reflectivity of woodland, fields, and suburbs between London and St. Albans in England. Fritz (1948) performed measurements of the upward and downward components of solar radiation flying in a B-29 airplane on 22 March 1947 over the center of USA. He found that albedo depends on the wetness of the soil as well as vegetation ground cover. Sutcliffe (1956) demonstrated the importance of albedo in the energy balance and its relationship with non-precipitating clouds. Kuhn and Suomi (1958) carried out albedo measurements in the Great Plains as part of the Tornado Research Project. With the development of new technology, albedo measurements were taken using meteorological satellites in addition to those obtained by airplanes and photometers. For example, Conover (1965) determined the average albedos for various clouds and terrestrial surfaces (Table 2.1) using satellite pictures from TIROS.

Manabe (1969), taking advantage of new and better computers, incorporated into a general circulation numerical model the effect of hydrology of the earth's surface. That study considered the evaporation from a sufficiently wet land surface that included a surface covered by dense vegetation. He also calculated the zonal mean values of both sensible and latent heat fluxes at the earth's surface (Figure 2.1).

Sasamori (1970) developed a numerical model similar to the one used by Manabe (1969). In this case the model simulated the exchange of heat and moisture between the

Table 2.1: Average albedos (A) for various terrestrial surfaces and clouds determined by satellite TIROS. n represents the number of reflecting points measured in each set of pictures and MCO means "mostly cloud covered" (after Conover, 1965).

Surface	n	$A(\%)$
Cumulonimbus-large and thick	8	92
Cumulonimbus-small, top 6 km	1	86
Cirrostratus-thick with lower clouds and preci.	7	74
Cirrostratus alone, over land	1	32
Cirrus alone, over land	2	36
Stratus-thick, approx. 0.5 km, over ocean	14	64
Stratus-thin, over ocean	2	42
Stratocum. masses within cloud sheet over ocean	4	60
Stratocumulus-MCO, over land	3	68
Cumulus and Stratocumulus-MCO, over land	4	69
Cumulus of fair weather-MCO, over land	2	29
Mostly snow-covered mts.above,timer,3-7days old	3	59
Sand-White Sands, New Mexico	1	60
Sand-valleys, plains and slopes	5	27
Sand and brushwood	2	17
Coniferous forest	4	12
Great Salt Lake	2	9
Ocean-Pacific	2	7
Ocean-Gulf of Mexico	6	9
Ocean-Gulf of Mexico-sunglint	3	17

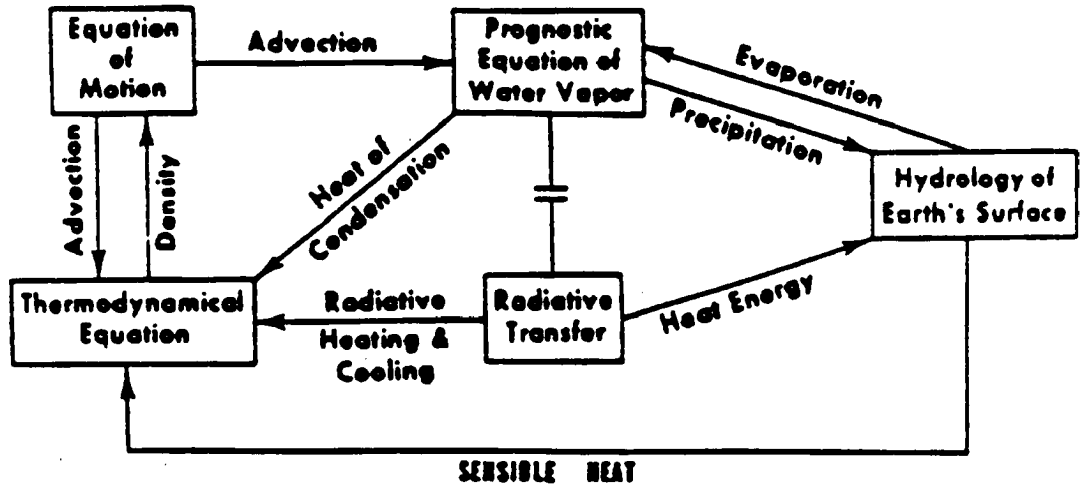

Figure 2.1: Diagram indicating the major components of the Manabe's model (after Manabe, 1969).

atmosphere and the soil. It was applied to study the energy balance of the soil surface with specific concern for soil wetness. Sasamori's model was able to show clearly the different characteristics of the surface energy balance depending on soil wetness. He found that if the soil is sufficiently wet, most of the net radiative energy is transformed into latent heat released to the atmosphere. On the other hand, if the surface is dry or with deficient water, the latent heat becomes negligible and most of the net radiation is transformed into sensible heat. Gadd and Keers (1970) studied the surface exchanges of sensible and latent heat in a 10-level atmospheric model. They calculated the fluxes of energy across the surface using an empirical bulk-aerodynamic relationship (Figure 2.2). Idso et al. (1975) showed that simple measurements of bare soil albedo can provide an estimation of soil water content for various land surfaces. From four experiments carried out on Avondale loam soil at Phoenix, Arizona in May, July, September, and December 1973, he found that the shape of the albedo curves for wet and dry conditions were the same for all four times of the year. He also found that wet soil had smaller albedo values than dry soil. Therefore, he inferred that albedo is dependent on the moisture content of the surface, and is thus dependent on vegetation cover (Figure 2.3).

Charney (1975), in an study of the dynamics of deserts and drought in the Sahel, Africa, stated that a self-induction effect through albedo enhancement takes place in deserts. Low rainfall causes low vegetation cover. Since dry sandy and rocky soil has higher albedo than soil covered by vegetation, desert surfaces become hotter than surrounding areas. Deserts emit more terrestrial radiation to space and they contribute to a net radiative heat loss compared to their surroundings. In reference to albedo associated with different types of surfaces, Otterman (1977) found that the albedo of crops and vegetation varies according to the seasons, due to changes in moisture content. He demonstrated that different land uses destabilize soil which in turn affects albedo in two ways: By microscale effects that increase the albedo due to a lack of plants; and by macroscale effects that create areas of bright sand dunes that can cover the vegetation. Mahrer and Pielke (1978) applied a three dimensional numerical model to study the mesoscale effect of the albedo contrast between the Negev and Sinai areas. They found for dry conditions

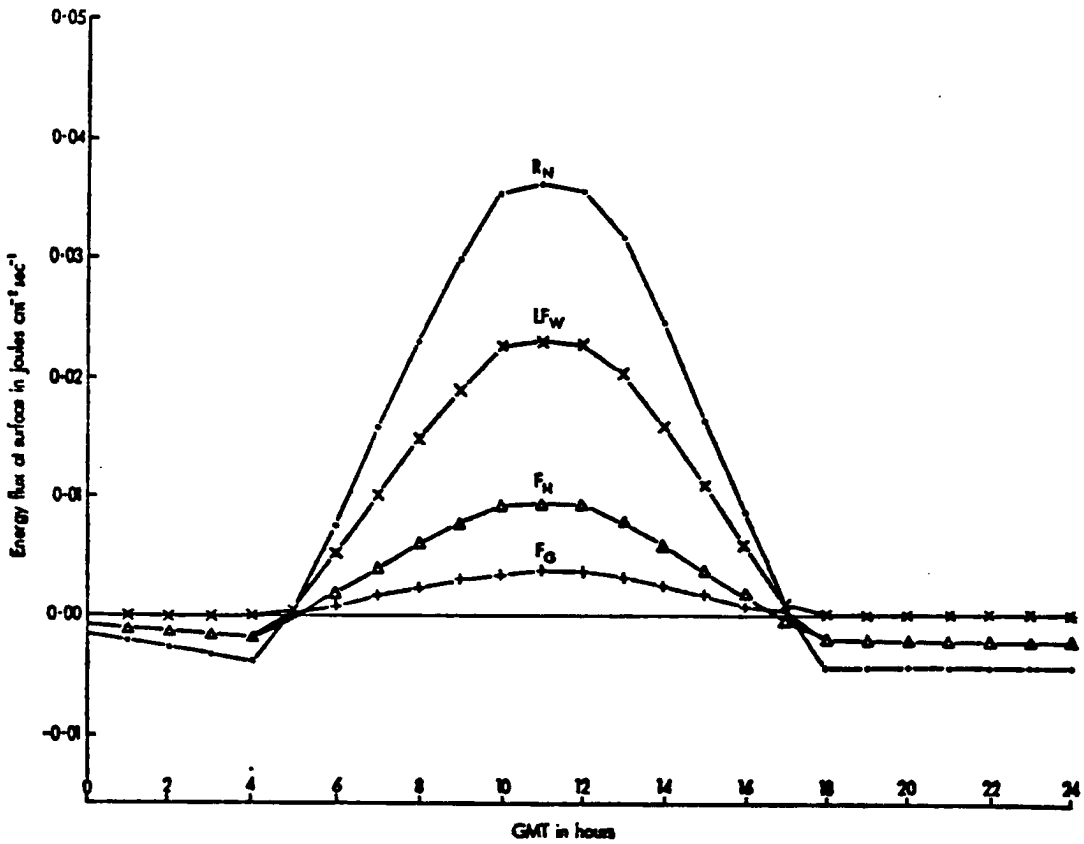

Figure 2.2: Diurnal variation of the energy fluxes at the surface as computed at a grid point in a 10-level atmospheric model during a 24-hour forecast for 21 August 1965. R_N represents the net vertical flux of solar and long-wave radiative energy at the surface, LF_W is the latent heat flux, F_H depicts the sensible heat flux, and F_G displays the heat flux into the ground (after Gadd and Keers, 1970).

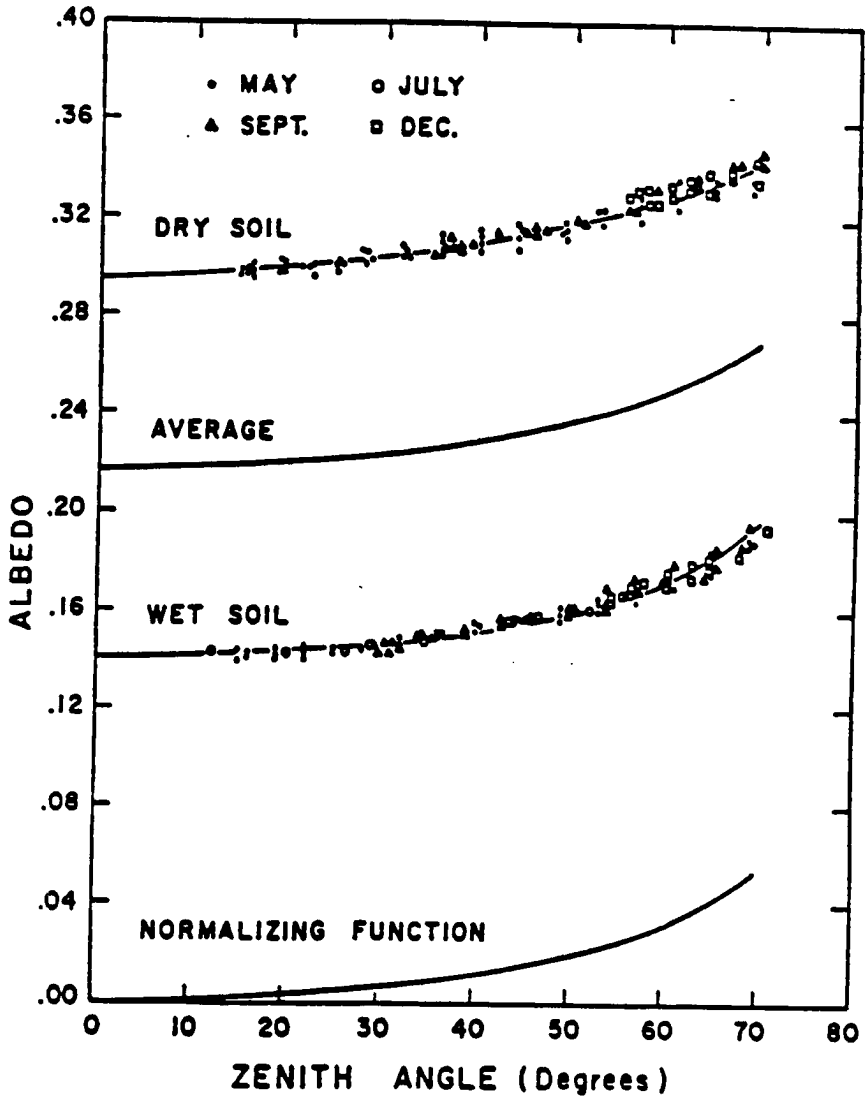

Figure 2.3: Wet and dry soil albedo vs. zenith angle for the four experiments carried out on May, July, September, and December 1973 at Phoenix, Arizona (after Idso et al., 1975).

that the predicted surface temperatures in the Negev were significantly higher than Sinai. However, when low moisture content was used, 5% of relative humidity for the Negev, they noticed that no ground temperature gradients were developed. Mahrer and Pielke concluded that the results are very sensitive to soil wetness, and even small values of moisture are enough to completely mask the albedo influences.

In recent studies, investigators have been evaluated how different types of surfaces with different albedo, modify thermal fluxes. McCumber and Pielke (1981) simulated the effect of surface fluxes of heat and moisture using a one-dimensional mesoscale numerical model (Figure 2.4). They developed a parameterization for bare soil that takes into account 11 types of soil. They showed that the most important characteristic of the soil is its moisture, which regulates the strength of the heat fluxes between the atmosphere and the ground. Otterman (1981) in his study about man's impact on the surface in arid regions concluded that anthropogenic effects can result in an increase of albedo by a factor of two-thirds, or by nearly 0.2. Three years later, Otterman (1984) developed a model in which he simulated a surface consisting of a soil-plane and protruding vertical plant elements, such as needles of pine trees or stalks of a wheat field. He found that the model reproduces quite well the dependence of albedo on the solar zenith angle and the overall light trapping characteristics of such a complex surface.

Sud and Smith (1984), using a modified climate GCM simulated the surface fluxes and cloudiness in the Planetary Boundary Layer (PBL) and its effect on the rest of the atmosphere. They considered an idealized averaged grid-volume by assuming that the surface bulk Richardson number changes within a grid box conforming to a Gaussian frequency distribution.Also, they pointed out that the PBL processes are affected by changes in surface albedo, which depends on soil moisture. Otterman (1985) continued assessing the surface albedo in semi-desert regions using satellite (NOAA-6) measurements of surface albedo and temperatures in an arid steppe located in northern Sinai considering the vegetation in a fenced-off area surrounded by bare sandy soil. He found from the thermal infrared measurements that the temperatures in the band of $11\mu m$ were higher in the exclosure than those measured over the bare sands outside. He suggested that the

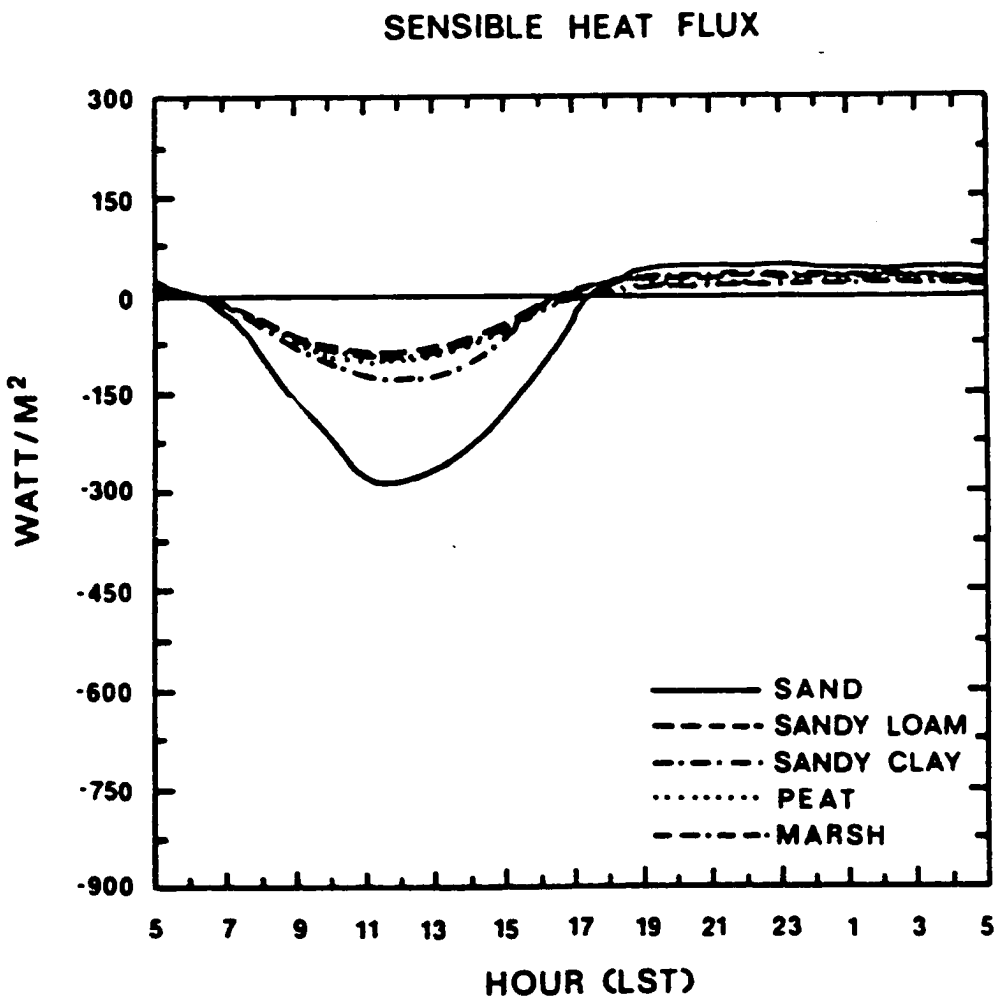

Figure 2.4: Predicted sensible heat fluxes (W m^{-2}) as a function of soil type. Notice that fluxes directed toward the atmosphere are negative (after McCumber and Pielke, 1981).

magnitude of the sensible heat fluxes from the vegetated area are controlled by albedo. This means that vegetation may reduce the surface albedo and increase the flux of sensible heat to the atmosphere.

Wetzel and Chang (1987) examined the effect of natural soil heterogeneities on evapotranspiration and presented simple expressions for the evapotranspiration parameter for the cases of vegetation cover and bare soil. They used a simple evapotranspiration model that assimilated some of the known properties of spatial heterogeneity of surface soil moisture and NDVI (Normalized Difference Vegetation Index) data. They realized that within each soil texture class, typical variations of soil properties are larger than the differences between classes. Also, they learned that the soil moisture variations were found to be significant even for a single type of soil. In addition, Wetzel (1987) developed a simple statistical method to estimate the soil moisture using GOES-VISSR infrared data. He used a linear regression to relate soil moisture to surface temperature and other variables. His results agree with observed data for the five days of clear sky conditions that he chose over Kansas and Nebraska. From these studies it can be inferred that soil moisture and its distribution is a significant component that affects the albedo, therefore, it is important that grid in numerical models (GCM) points improve their resolution and include considerations of surface soil heterogeneity (Wetzel and Chang, 1987), since both temperature and water vapor mixing ratio can vary over relatively short distances due to variability of the land surface (Wetzel, 1990).

Mahrt (1987) proposed a new formulation for surface fluxes in numerical models of atmospheric flow. He assumed idealized spatial distributions of the Richardson number over a grid area. In this way, the proposed formulation relates the area-averaged flux to the area-averaged gradient.

Segal et al. (1988) demonstrated how vegetated areas modify surface thermal fluxes as compared to those of an equivalent bare soil surface even when both were under the same environmental conditions. Pielke and Avissar (1989) explained the physical linking that exists between the surface and atmosphere. They utilized the earth's global energy budget equation to perform this analysis. This relationship can be written as:

$$\sigma T_E^4 = S(1 - A)/4, \tag{2.1}$$

In Equation (2.1) $\sigma = 5.67 \times 10^{-8}$ W m$^{-2}K^{-4}$, S is the solar constant ($S = 1380$ W m^{-2}), A is albedo and T_E is the temperature of the earth assuming that it radiates as a blackbody. Pielke and Avissar (1990) stated that the surface heat and moisture budgets are functions of several parameters in which the albedo plays an important role. For instance, it can be shown how even for small changes in the landscape, the albedo is modified. Differentiating Equation (2.1) with respect to A and taking increments for the variables T and A, Equation (2.1) can be approximated as:

$$\Delta T_E = -15.21 \times 10^8 (K^4) \frac{\Delta A}{T_E^3} \tag{2.2}$$

For a temperature of $273.5°K$ which is a reasonable global temperature of the earth (MacCracken and Budyko, 1990; Kelly et al., 1982), Equation (2.2) becomes:

$$\Delta T_E = -74.34 \Delta A \tag{2.3}$$

Assuming that only land albedo (δA_l) changes, we have that $\Delta A = \delta A_l f$ where f is the fraction of the earth that is land ($f = 0.25$) (Pielke and Avissar, 1990). Thus, Equation (2.3) becomes:

$$\Delta T_E = -74.34 \frac{\delta A_l}{4} = -18.6 \delta A_l \tag{2.4}$$

From Equation (2.4) it can be seen that for a 10% increase in the albedo of land $\Delta T_E = -1.86°$C. And for a 1% increase $\Delta T_E = -0.18°$C. These calculations show clearly how sensitive the atmosphere is even for small changes in the albedo.

Recently, André et al. (1990) studied estimated area-average heat surface fluxes over non-homogeneous terrain using data from the HAPEX-MOBILHY (Hydrologic Atmospheric Pilot Experiment and Modelisation du Bilian Hydrique) program which took place in southwestern France during 1985 and 1986 (André et al., 1986), (Figure 2.5). They found that there are two types of non-homogeneous land surfaces: (i) the "disorga-

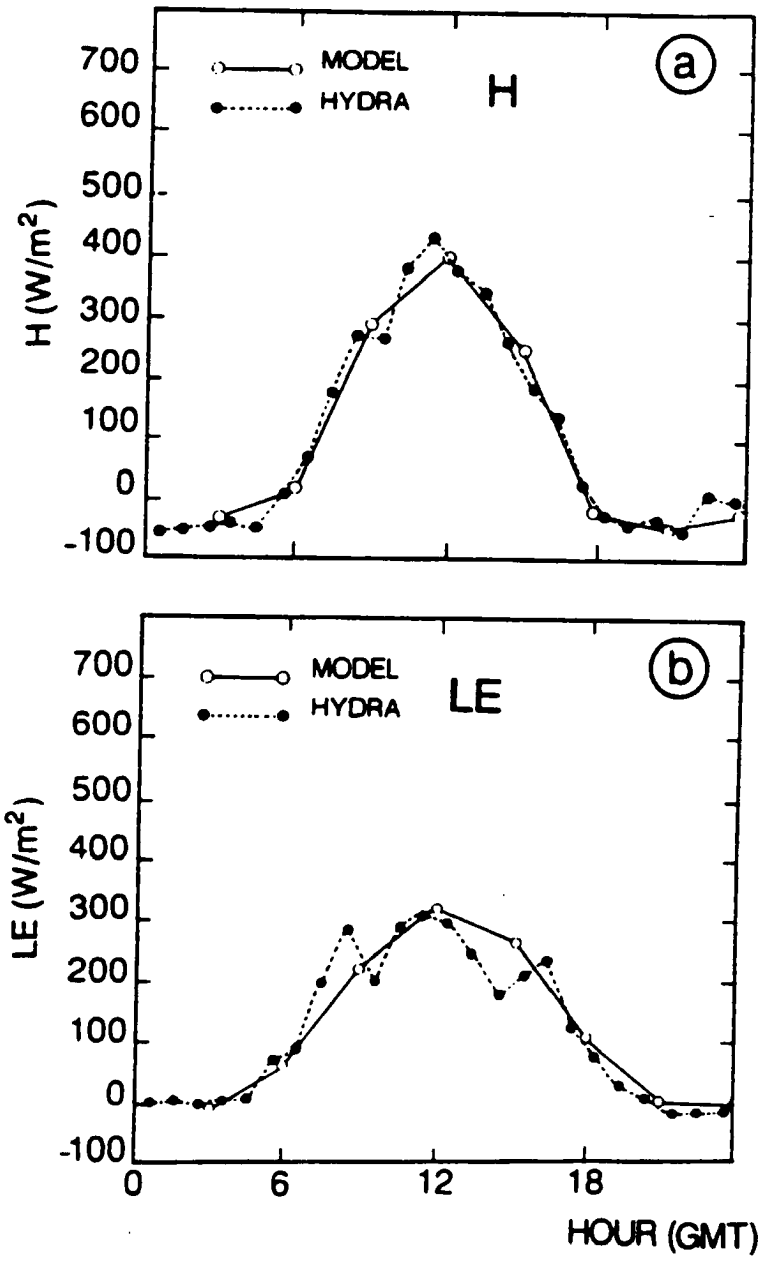

Figure 2.5: Comparison between simulated (solid lines) and observed (dashed lines) surface of sensible (a), and latent (b) heat fluxes over the Landes forest on June 16 (after André et al., 1990).

nized" land surfaces, for which the characteristic horizontal scale is smaller than 10 km, so that no apparent coherent response can be traced in the atmosphere since the boundary-layer turbulence averages everything out; (*ii*) the "organized" land surfaces, for which the characteristic length is greater than 10 km, so that the atmosphere develops a coherent response at the mesoscale. They suggest that this threshold scale (10 km) is related to the depth of the ABL (Atmospheric Boundary Layer) which is about 1 km. Thus, the ABL takes approximately ten times its length to adjust fully to a new equilibrium state. Avissar and Pielke (1991), using a sophisticated land surface parameterization emphasized the role of plant stomata on the control of the Bowen ratio (β) on mesoscale atmospheric circulations since it can generate large variations in sensible and latent heat fluxes at the earth's surface. The Bowen ratio is defined as follows (Segal et al., 1989):

$$\beta = \frac{H_s}{\lambda E} \tag{2.5}$$

Here H_s is the sensible heat flux and λE is the latent heat flux at surface (λ = *latent heat of vaporization*). In general β is small over moist land and large over dry areas (Figure 2.6).

Pielke et al. (1991) calculated the mesoscale and turbulent heat fluxes that result from idealized landscape spatial variability. They concluded that the influence of mesoscale landscape variability on the atmosphere must be parameterized in large-scale atmospheric model simulations including GCMs. Also, they found that mesoscale heat fluxes are often of the same order of magnitude or larger than the turbulent fluxes. The mesoscale fluxes also have a different vertical structure. Similar results were found by Dalu and Pielke (1992) when they evaluated the vertical heat fluxes associated with the mesoscale flow generated by thermal inhomogeneities in the PBL in the absence of a synoptic wind. Klaassen (1992) evaluated the fluxes of heat and momentum using a surface-layer model for flat regions with regularly spaced step changes in the stomata resistance and surface roughness. Based on his simulations, he concluded that very widely spaced heterogeneities in vegetation height influence regional fluxes.

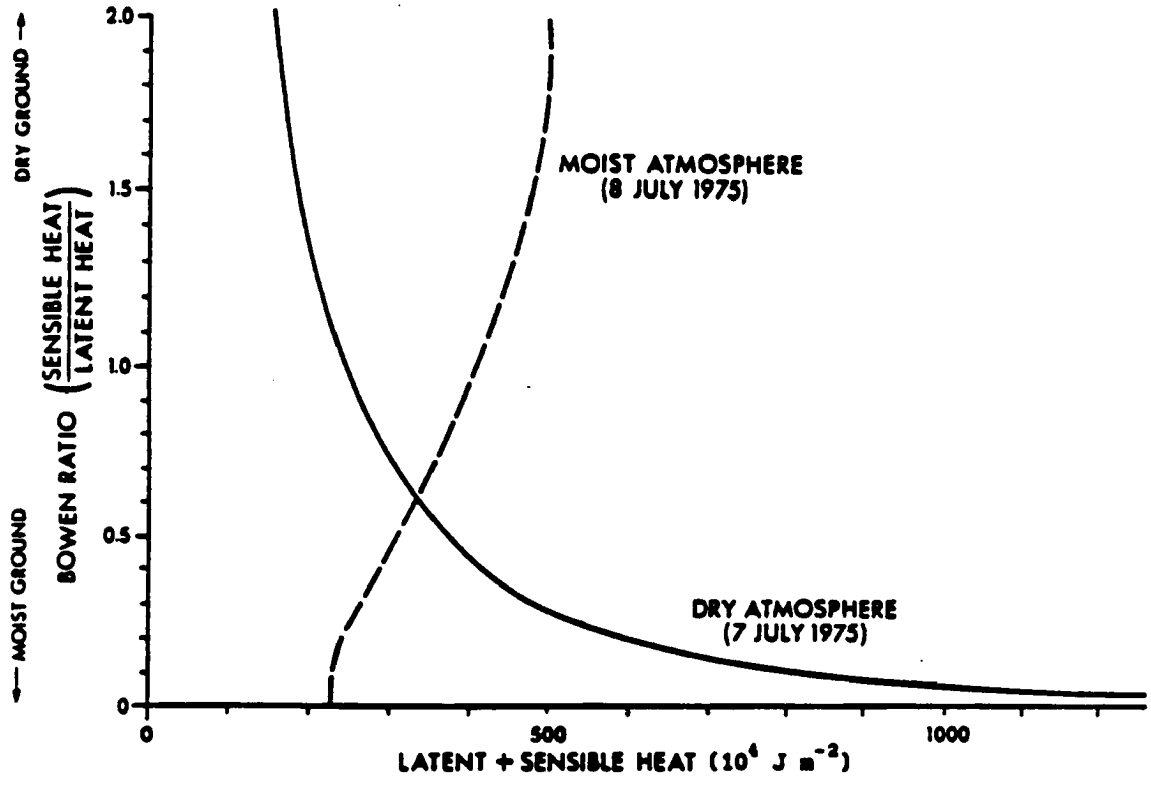

Figure 2.6: The Bowen ratio at the ground for dry and moist atmosphere profiles (after Rabin, 1977).

Chapter 3

DATA ANALYSIS

3.1 Study Region and Time of Year

The study site is located in northern Arizona just south of the Grand Canyon National Park and it was selected from a larger region formed mainly by the states of Utah and Arizona (Figure 3.1). The study region (A_1 in Figure 3.1) with an area of 100×100 km^2 is centered near 35.47 N−112.15 W and is part of the Coconino Plateau. To the east are the Rocky Mountains. This area has a generalized pattern of vegetation formed mainly by pinyon-juniper, ponderosa pine, and chaparral species (Geological Survey, 1970). The land uses are classified as forest and woodland grazed, open woodland grazed, subhumid grassland, and semiarid grazing land. In general the Coconino Plateau soils are constituted of fine sandy loam, gravelly sandy clay loam, stony loam, gravelly fine sandy loam, and gravelly sandy loam (Soil Survey, 1983). With respect to climate, data recorded in the period 1951–1975 at Seligman, Ariz. showed that in February average temperature is 4.61°C, average precipitation is 16.25 mm, and average snowfall is 35.56 mm. For June, average temperature is 19.72°C and average precipitation is 15.49 mm (National Climate Center, 1979). This study area was chosen because it has large horizontal variations in topography (Figures 3.2a and b). For instance, can be found variations from 1100 m to 2400 m, mainly over its south region which can be tested against its large albedo variability in the RAMS simulations to assess the relative contributions of both topography and albedo variability to the area-averaged heat fluxes. This domain size permits meso-β scale atmospheric phenomena which range from 20 to 200 km in horizontal extent (Orlanski, 1975). The topography data was obtained from NCAR.

Two test cases were chosen, one winter and one summer. The date for the winter case was 10 February 1986; the summer case was 7 June 1986. We expect differences

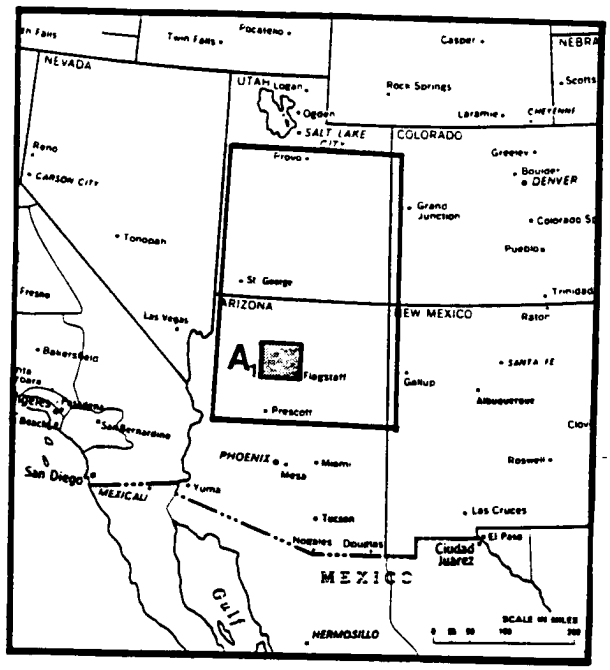

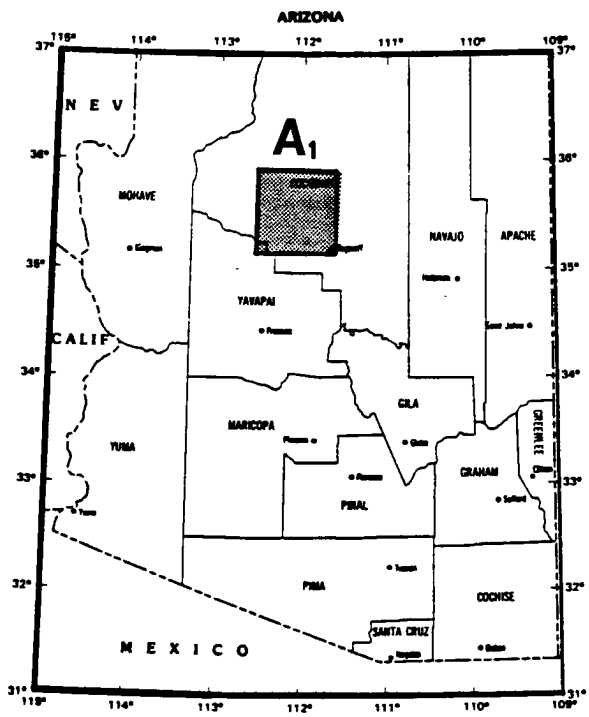

Figure 3.1: The region labeled A_1 is the study site. It covers an area of 100×100 km^2.

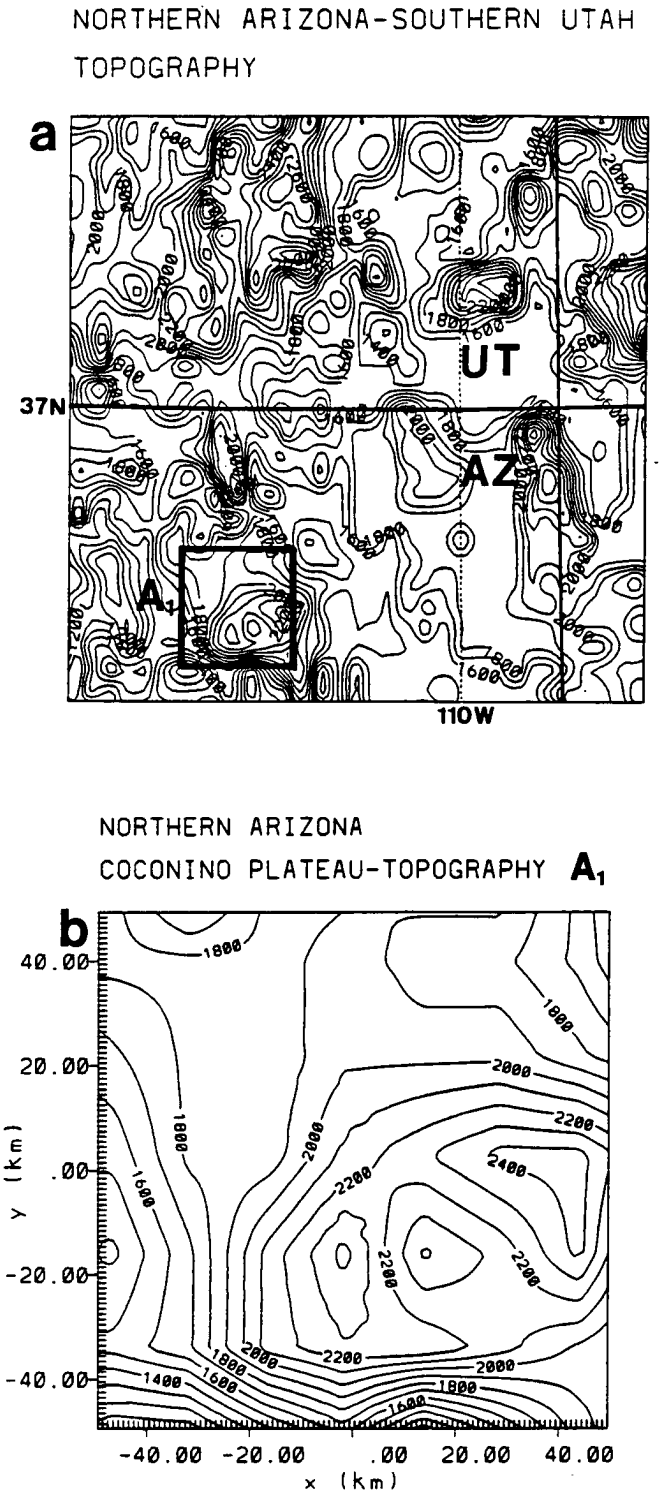

Figure 3.2: (a) Topography of northern Arizona and southern Utah, and (b) terrain characteristics of the study site (A_1). The contour intervals are 100 m. Topography data obtained from NCAR.

in the albedo between seasons because of the angle of the solar radiation, plant activity, moisture at the surface of the soil. This study assesses how the summer case and winter case albedos for the actual complex terrain and an equivalent idealized flat terrain are capable of generating significant mesoscale circulations. We also consider the expected importance of these effects in GCMs.

3.2 The Albedo Data

3.2.1 Introduction

Meteorological satellites are useful in obtaining surface albedo data. For instance, data have been obtained from TIROS satellite pictures (Conover, 1965) to calculate the albedo for different terrestrial surfaces and clouds. Surface albedos in the northern hemisphere have been inferred from the satellites ESSA, ITOS, and NOAA series (Kukla and Kukla, 1974). Vonder Haar and Ellis (1974) calculated the planetary albedo using data from satellites TIROS 4 and NIMBUS 3 series for a period of 1962-1970 to create an *Atlas of Radiation Budget Measurements From Satellites.* Otterman and Fraser (1976) computed the reflectivities and albedo for some arid regions of Africa, Asia, and Central America using data from satellite LANDSAT Multispectral Scanner digital tapes. Rockwood and Cox (1978) developed a technique using simultaneous satellite and aircraft data that permits the magnitude and gradient of the earth's surface albedo to be inferred from satellite measurements of the earth-atmosphere system brightness. They used the visible (VIS) brightness observations from the SMS-1 geosynchronous satellite taken during the GARP Atlantic Tropical Experiment (GATE) in 1974. Mekler and Joseph (1983) developed an empirical method to measure the spectral surface albedo using imagery from LANDSAT. Minnis and Harrison (1984) developed a method to use shortwave radiances to estimate radiant exitances with bidirectional reflectance models derived from GOES for ocean, land, and clouds. Pinty et al. (1985) used radiances from satellite METEOSAT to estimate the surface albedo in the African Sahel. Otterman (1985) used data from NOAA-6 satellite to determine the surface albedo and temperatures in a semi-desert region of the northern Sinai. He assessed the effects of vegetation recovery in a fenced-off

area. Estimated errors for all these calculations are in the range of ±10% (Gautier et al., 1980; Mekler and Joseph, 1983; Pinty et al., 1985).

3.2.2 The Satellite Data

Visible imagery from GOES-6 for the dates 10 February 1986 and 7 June 1986 were used to calculate albedo in the rectangular region (Figure 3.1). These images have 1 km pixel data and cover a domain of 512×512 km^2, centered near 37 N – 111 W. This area occupies most of Arizona and Utah. These images were selected on the basis of clear sky conditions, though some clouds were present. For instance, the picture of 10 February 1986 (Figure 3.3) at 1800 UTC shows some clouds mainly over its southeastern region. Also, for 7 June 1986 (Figure 3.4) at 2200 and 2300 UTC some cumulus clouds were present. However, in general, the cloud effect for both dates was relatively unimportant.

3.2.3 Methodology

Imagery analysis was conducted using the capabilities of the CIRA (Cooperative Institute for Research in the Atmosphere) Ground Station located at Colorado State University (CSU). For the two dates, 18 images were obtained, 9 for the winter date and 9 for the summer date which matched every hour from 1500 UTC to 2300 UTC. Using a program written by G. Garrett Campbell (1992, personal communication), albedo images were developed for each VIS picture. The program converts VIS counts (0-255) into albedo images using the ERBE (Earth Radiation Budget Experiment) bidirectional model, and Minnis and Harrison (1984) calibration tables. Thus, the visible (VIS) brightness counts (D) from GOES are converted to broadband shortwave (L_{sw}) radiances using spectral calibration functions determined empirically from Nimbus-7 ERB and GOES-E measurements over ocean, land and cloud surfaces. That is, Nimbus 7 ERB shortwave ($0.2 - 4.8\mu m$) scanning radiometer data were matched with GOES VIS ($0.55 - 0.75\mu m$) measurements of approximately the same scene obtained within 15 minutes of each other (Minnis and Harrison, 1984c). Radiances with appropriate anisotropic corrections were then used to calculate the shortwave (M_{sw}) radiant exitances (fluxes) by way of integration over the upward hemisphere. To estimate the radiant exitances a bidirectional reflectance

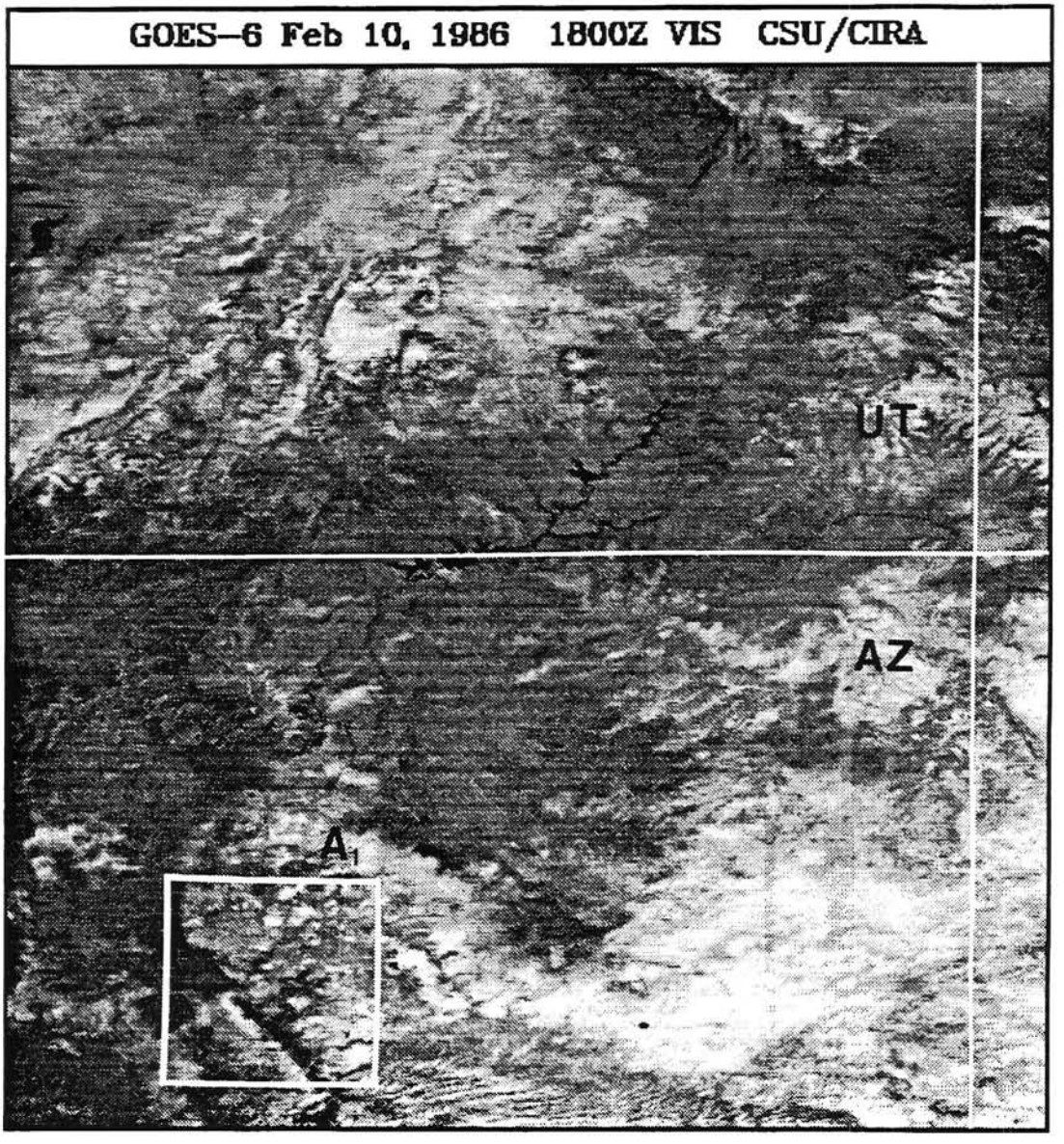

Figure 3.3: GOES-6 visible image for 10 February 1986 at 1800 UTC. The small area labeled A_1 is the study region.

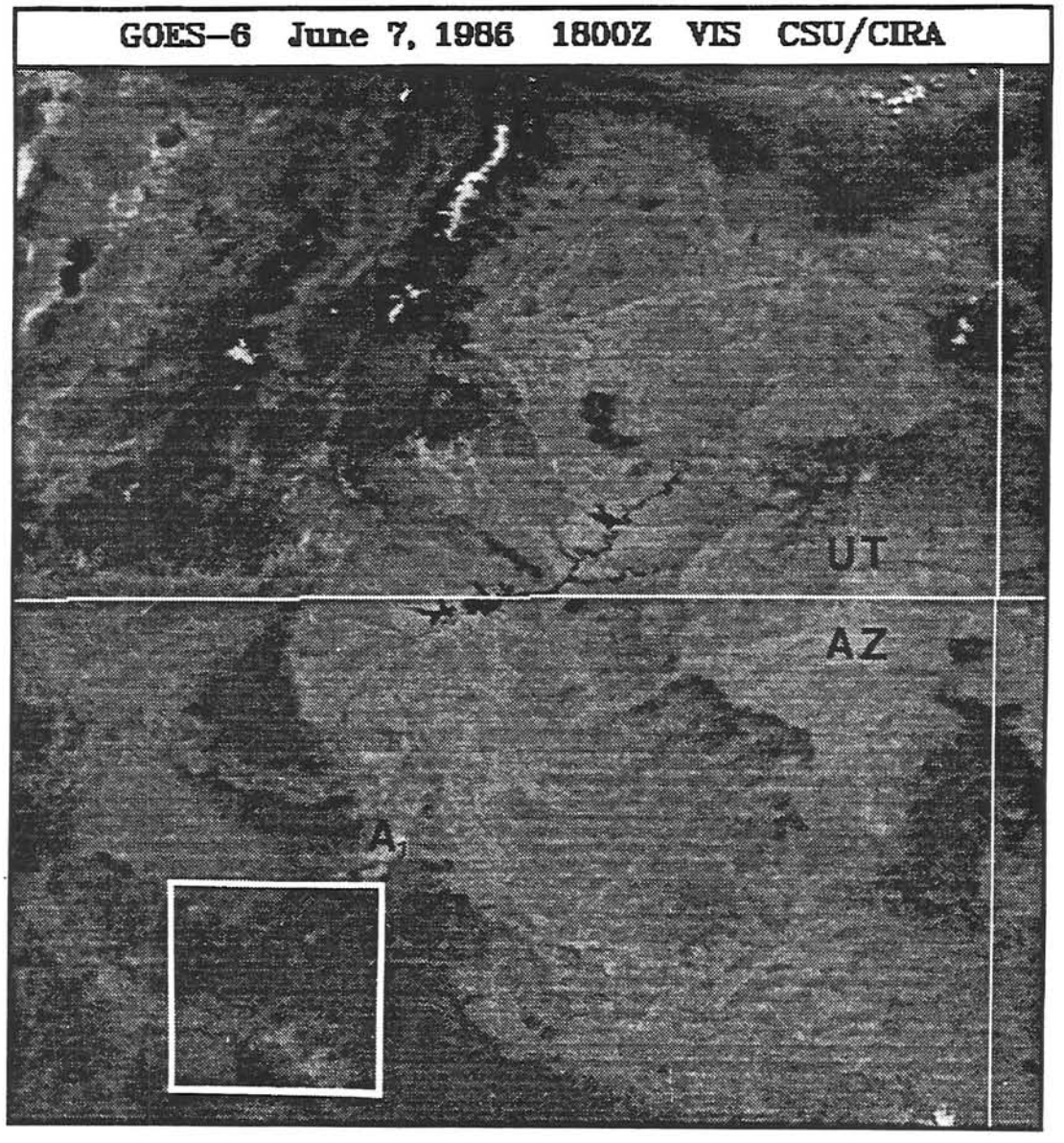

Figure 3.4: GOES-6 visible image for 7 June 1986 at 1800 UTC. The small area labeled A_1 is the study region.

model (BDR) derived from GOES was used. Sikula and Vonder Haar (1972) stated that bidirectional reflectance patterns of the surface must be taken into account to obtain real albedo data since the reflecting surface has different albedos for different angles of view for a given solar incident angle. They defined the bi-directional and directional reflectances as follows:

$$\rho(\zeta,\theta,\psi) = \frac{reflected\ radiation\ in\ the\ direction\ \theta,\psi_2}{incident\ radiation\ from\ a\ given\ \zeta,\psi_1} = bi-directional\ reflectance \tag{3.1}$$

$$r(\zeta) = \frac{reflected\ radiation\ in\ all\ directions}{incident\ radiation\ from\ a\ given\ \zeta,\psi_1} = directional\ reflectance \tag{3.2}$$

where ρ is a property of the surface with units of $steradians^{-1}$, ζ is the solar zenith angle, ψ_1 the solar azimuth angle, θ is the satellite zenith angle, ψ_2 the satellite azimuth angle, and $\psi = \psi_1 - \psi_2$ is the relative solar azimuth angle (Figure 3.5). Those two reflectances are related by the equation

$$r(\zeta) = \int_0^{2\pi} \rho(\zeta,\theta,\psi) cos\theta d\Omega = \int_0^{2\pi}\int_0^{\pi/2} \rho(\zeta,\theta,\psi) cos\theta sin\theta d\theta d\psi_2 \tag{3.3}$$

In a similar way, Minnis and Harrison (1984) defined a bidirectional reflectance (BDR) model which consisted of anisotropic reflectance correction factors $\chi(K,\zeta,\theta,\psi)$ that were used to determine the radiant exitance for a given surface type K as:

$$M_{sw}(\phi,\lambda,K,\zeta) = \frac{\pi L_{sw}(\phi,\lambda,\zeta,\theta,\psi)}{\{K(\phi,\lambda),\zeta,\theta,\psi\}} \tag{3.4}$$

Where χ represents the anisotropic factors and the broadband shortwave radiances (L_{sw}) for land given by:

$$L_{sw} = 1.92(D^2 - 6.25)^{0.5} + 0.0616(D^2 - 6.25) \tag{3.5}$$

Also, they defined the shortwave radiant exitance $[M(\phi,\lambda,\zeta)]$, or flux as:

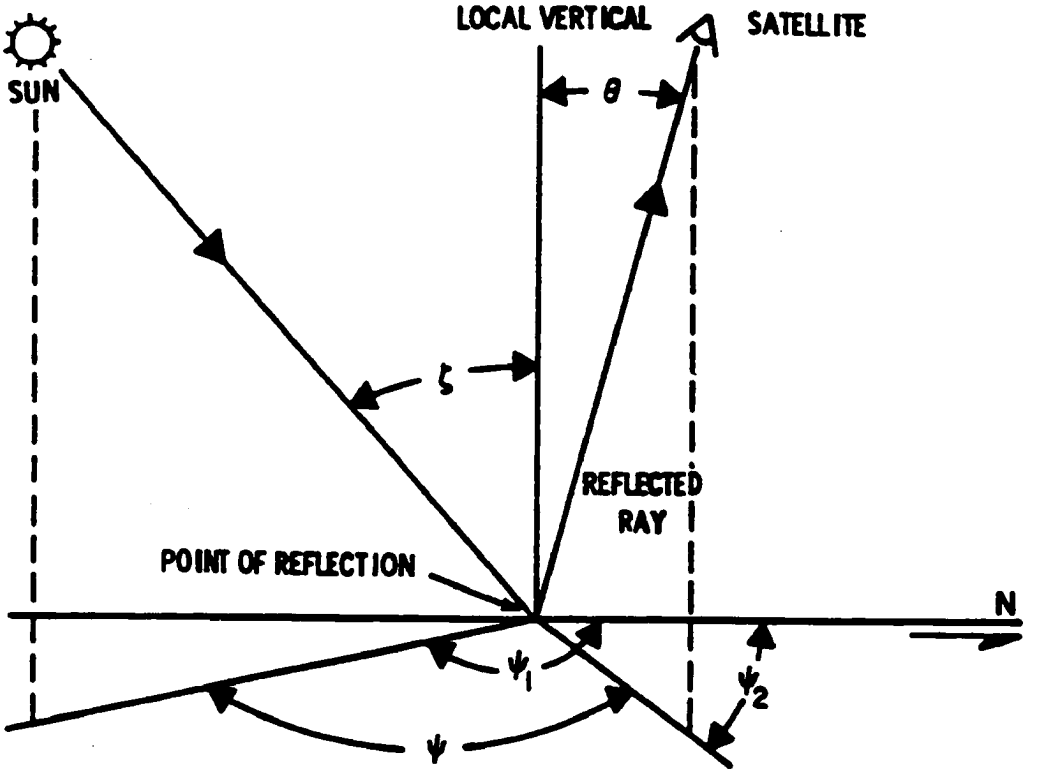

Figure 3.5: Geometrical configuration for earth, sun, and satellite. ζ is the solar zenith angle, θ is the satellite zenith angle, ψ_1 is the solar azimuth angle, ψ_2 is the satellite azimuth angle, and ψ is the relative solar azimuth angle (after Sikula and Vonder Haar, 1972).

$$M(\phi,\lambda,\zeta) = \int_0^{2\pi}\int_0^{\pi/2} L_{sw}(\phi,\lambda,\zeta,\theta,\psi)cos\theta sin\theta d\psi. \tag{3.6}$$

More details about bidirectional reflectance models can be found in the papers of Minnis and Harrison, (1984a, 1984c), and also in the paper of Sikula and Vonder Haar (1972). In this study the concepts of BDR were included in a program (Campbell,1992) to calculate albedo at a certain time (t), by means of the relationship:

$$A(t) = \frac{\pi L_{sw}}{S[BDR(n)]} \tag{3.7}$$

Here S is the solar constant and n represents the model number based on ERBE scene types (ERBE, 1985). A value $n = 2$ means that surface type is land with a cloud cover percent less than about 5%. When $n = 3$ the ERBE scene type is snow. In the present study the scene type 2 (land) was used for the 7 June 1986 date. Scene type 3 (snow) was chosen for the winter case since a few days previous to February 10, a deep cold low brought some snow to the region. Nevertheless, the model 2 (land) also was tested for the winter case, but little difference was found between both model numbers. Albedo calculations are exposed to some error since the scene types are difficult to match with the real conditions. Cloud cover is also one of the factors that affects surface albedo. However, geostationary satellites such as the GOES (Geostationary Operational Environmental Satellite) series are among the most effective existing remote sensing devices to obtain measurements of the albedo (Pinker et al., 1986). In addition, the GOES series seem to have an important advantage over the polar orbiting satellites because they can provide almost continuous coverage. The polar orbiting satellites have only one or two observations per day. This low temporal resolution limits the evaluation of planetary radiation budget parameters from space (Pinker et al., 1986). On the other hand, GOES calibrations can be improved using methods based on numerical solutions to the radiative transfer equation (Smith and Vonder Haar, 1983; Pinker et al., 1986). In general, not only the GOES series but other satellites as well, as discussed previously, have an error of $\pm 10\%$ (Gautier et al., 1980; Mekler and Joseph,1983; Pinty et al., 1985). In our case, the errors were about the same order of magnitude. For instance, for albedo values of 0.40 the error is ± 0.04 (Campbell,

1992). Therefore, the albedo values obtained here are appropriated samples to be used in the RAMS simulations.

3.2.4 Summer and Winter Albedo Statistics

Albedo data for the larger region (marked as a rectangular box in Figure 3.1) were obtained first. Secondly, the goal was to obtain a representative smaller area of 100×100 km^2 that should have both large albedo variability and complex terrain with important elevation gradients. The area A_1 (Figure 3.1), was the specific region chosen for detailed analysis. Albedo statistics for the rectangular area in Figure 3.1 were calculated for: Mean albedo ($\overline{A}$), standard deviation (σ_A), maximum (A_{max}), and minimum (A_{min}) albedo values (Tables 3.1 and 3.2). The mean and standard deviation were calculated using the formulas:

$$\overline{A} = \frac{1}{n}\sum a_{(i,j)} \tag{3.8}$$

$$\sigma_A = [\frac{n\sum a_{(i,j)}^2 - (\sum a_{(i,j)})^2}{n(n-1)}]^{1/2} \tag{3.9}$$

where $a_{(i,j)}$ represents albedo at the point (i,j) of the grid and n is the number of points.

Using the facilities of NCAR (National Center for Atmospheric Research) and a program written by Kelly Dean (1992, personal communication), plots of the albedo distribution were obtained from which the distribution at 1800 UTC (1100 LST) for winter and summer cases are shown (Figures 3.6 and 3.7).

The detailed study area (A_1) was chosen to compute albedo values and insert them into the Regional Atmospheric Modeling System (RAMS) to simulate the atmospheric response to these albedo variations. This smaller region also has a pixel size of 1 km, thus, the grid in RAMS has $\Delta x = \Delta y = 1$ km. Note that the values in the area A_1 are similar (Tables 3.3 and 3.4), and therefore representative of the larger area albedo statistics

Table 3.1: Surface albedo statistics for the rectangular area in Figure 3.1 (Utah and Arizona regions) for 10 February 1986. Here $\overline{A}$ is the mean albedo, σ_A is the standard deviation, A_{min} is the minimum albedo, and A_{max} is the maximum albedo. The symbol $(*)$ means that albedo statistics for 0800 LST was estimated by extrapolation because errors in the satellite data.

Time(LST)	$\overline{A}(\%)$	$\sigma_A(\%)$	$A_{min}(\%)$	$A_{max}(\%)$
0800(*)	47.75	12.39	24.96	82.51
0900	44.81	12.06	22.48	80.51
1000	41.87	11.73	21.00	78.51
1100	40.54	11.30	20.40	74.61
1200	39.38	10.68	18.45	70.82
1300	38.39	10.20	19.91	68.07
1400	37.62	10.05	18.97	67.81
1500	37.43	09.63	19.01	66.74
1600	38.94	09.54	21.32	74.27

Table 3.2: Surface albedo statistics for the rectangular area in Figure 3.1 (Utah and Arizona regions) for 7 June 1986. Here $\overline{A}$ is the mean albedo, σ_A is the standard deviation, A_{min} and A_{max} are the minimum and maximum albedo values respectively.

Time(LST)	$\overline{A}(\%)$	$\sigma_A(\%)$	$A_{min}(\%)$	$A_{max}(\%)$
0800	33.68	6.41	21.32	62.25
0900	28.07	5.34	17.77	51.88
1000	30.28	5.63	19.04	56.74
1100	25.70	4.58	15.90	48.93
1200	21.12	3.65	13.09	37.61
1300	20.94	3.83	12.84	55.13
1400	29.36	5.79	17.95	78.09
1500	28.82	5.99	17.78	93.03
1600	26.15	6.69	16.54	90.04

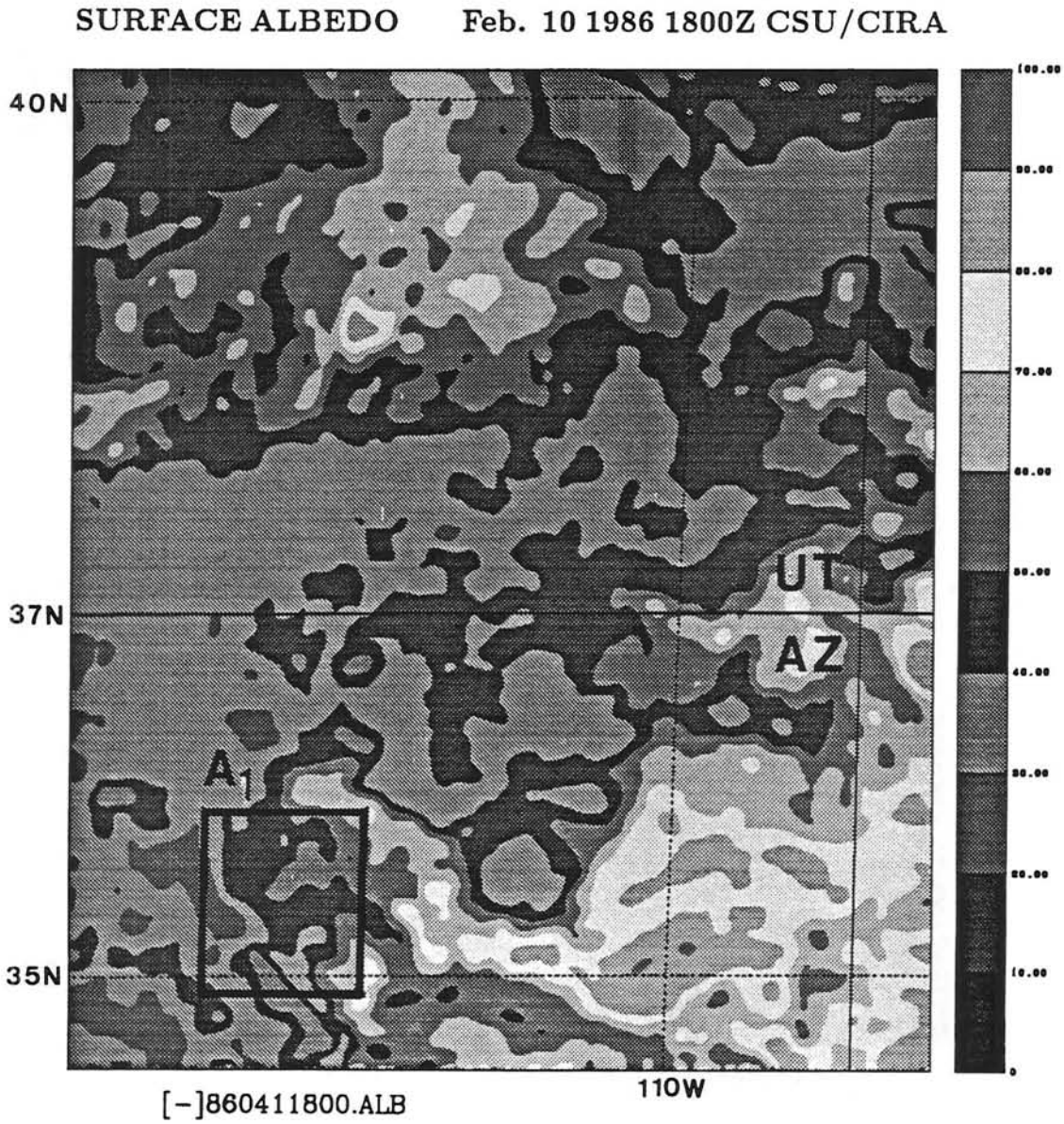

Figure 3.6: Surface albedo distribution in the rectangular area in Figure 3.1 for 10 February 1986. The small square labeled A_1 is the study site. Increments of the scale are in 10%.

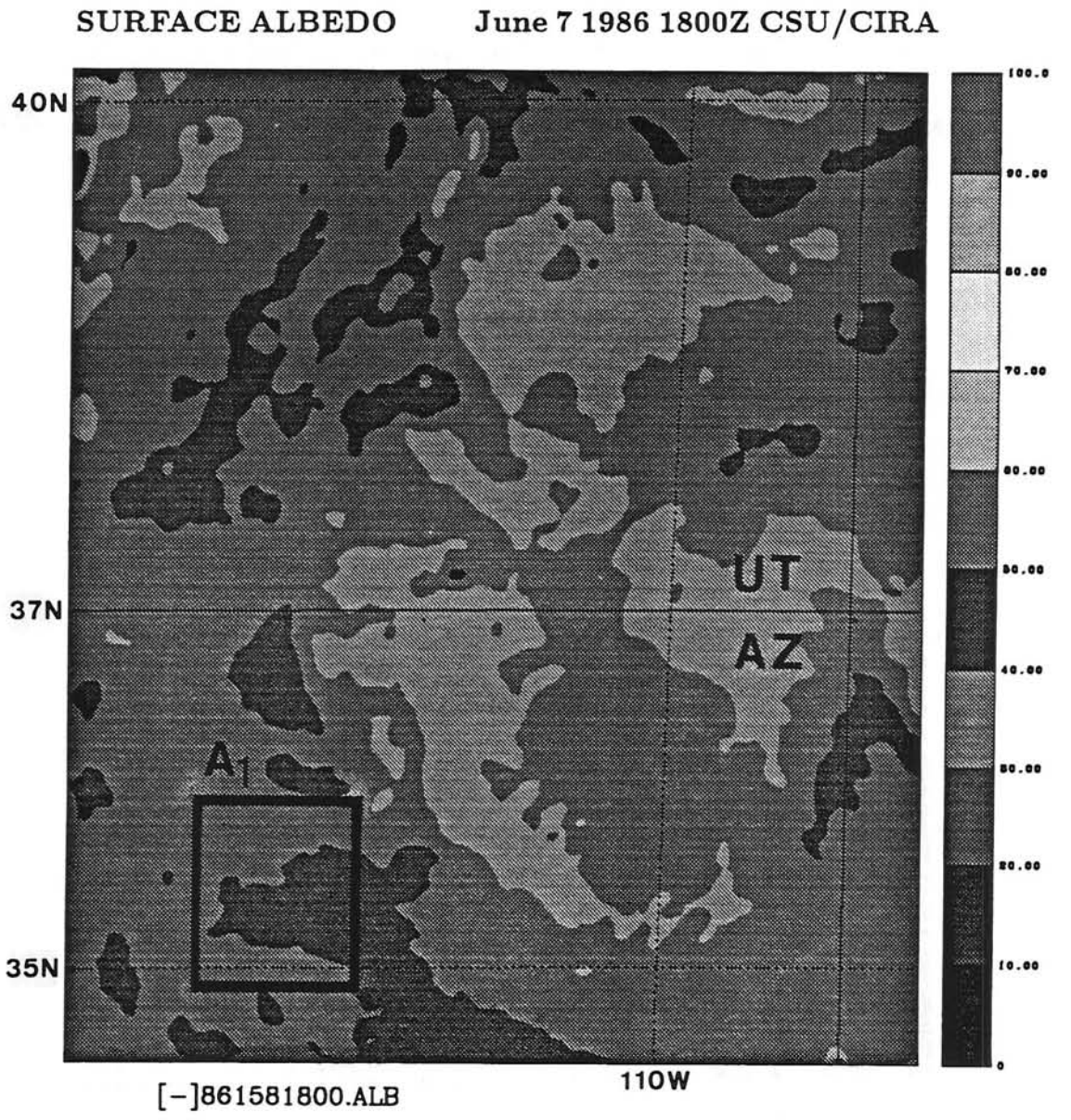

Figure 3.7: Surface albedo distribution in the rectangular area in Figure 3.1 for 7 June 1986. The small square labeled A_1 is the study site. Increments of the scale are in 10%.

(Tables 3.1 and 3.2). The smaller area A_1 was required because the larger domain could not be simulated with RAMS because of computer memory limitations.

Table 3.3: Surface albedo statistics for area A_1, 10 February 1986. Here $\overline{A}$ is the mean albedo, σ_A is the standard deviation, A_{min} is the minimum albedo and A_{max} is the maximum albedo. The symbol (*) for time 0800 LST means that the albedo values were estimated by extrapolation due to errors in the satellite data.

Time(LST)	$\overline{A}(\%)$	$\sigma_A(\%)$	$A_{min}(\%)$	$A_{max}(\%)$
0800(*)	49.06	13.88	19.10	80.07
0900	47.55	13.42	19.64	79.61
1000	46.04	12.96	21.36	79.15
1100	44.62	13.09	21.02	78.27
1200	42.65	13.09	20.78	78.87
1300	41.71	13.80	19.17	81.29
1400	39.57	12.88	18.38	71.66
1500	41.14	12.71	19.49	72.84
1600	42.71	12.53	19.66	73.36

Table 3.4: Surface albedo statistics for area A_1, 7 June 1986. Here $\overline{A}$ is the mean albedo, σ_A is the standard deviation, A_{min} and A_{max} are the minimum and maximum albedo values respectively.

Time(LST)	$\overline{A}(\%)$	$\sigma_A(\%)$	$A_{min}(\%)$	$A_{max}(\%)$
0800	31.65	4.68	18.58	48.36
0900	28.48	4.66	17.92	42.24
1000	27.34	4.23	17.16	38.56
1100	26.19	3.82	16.86	36.06
1200	21.40	2.94	14.05	29.39
1300	21.17	3.00	13.60	29.26
1400	24.82	3.69	16.11	35.42
1500	28.47	4.55	18.26	41.82
1600	32.12	5.19	20.09	49.88

A scaling factor was applied to the hours 1500 LST and 1700 LST in the data sets in order to minimize the effect of cloud contamination. For instance, the data for June case at 1500 LST presented higher values than the previous and subsequent hours. Thus, to downgrade those values we multiplied them by a factor of 0.845 to have congruence in the data set. Similar procedures were used for the hour 1700 LST. This adjustment was

necessary because clouds increased the albedo for that hour in comparison with the rest of the afternoon hours. The mean albedo average for the period 0800-1600 LST was around 43.89% for the winter, and 26.84% for the summer cases, respectively (Tables 3.3 and 3.4). These averaged albedos are close to the values given by the albedo climatology for the northern hemisphere for this geographic area (Ellis and Vonder Haar, 1976). Therefore, they are considered as a representative samples of the cold and warm seasons for this region.

This large seasonal differences take place due to several factors. For instance, changes in vegetative cover and wetness of the soil (NASA Conference Publication 2100, 1979), which could be generalized as changes in landscape due to marked differences in weather and climate conditions. Another important factor is the effect of solar zenith angle (ζ). For example, in our case, this effect can be calculated for both seasons at 1800 UTC using the following relationships (Vonder Haar, 1991):

$$cos\zeta = sin\phi sin\delta + cos\phi cos\delta cost$$

$$\delta = (-23°27')cos[\frac{2\pi}{365.25}(JD + 9)]$$

where ζ is the solar zenith angle, ϕ is the latitude, δ is the declination angle, t is the hour angle, and JD is the Julian day. At the center of area A_1 we have that ϕ=35.47°N latitude and 112.15°W longitude. For the winter case we have that $GD = 41$, therefore, the solar zenith angle for 10 February 1986 was $\zeta_{feb} = 59.46°$. For the summer case, $GD = 158$ resulted in a solar zenith angle of $\zeta_{jun} = 22.9°$. These solar zenith angles affected the absolute albedo values with an increment of about 3% in winter and about 1% in summer (Idso, 1975).

Chapter 4

THE RAMS SIMULATIONS

4.1 The CSU RAMS Model

The Colorado State University (CSU) RAMS model resulted from two earlier atmospheric modeling programs conducted independently by Drs. William Cotton and Roger Pielke since the early 1970's (Tremback and Walko, 1991; Pielke et al., 1992; Cotton et al., 1992). The two previous modeling contributions to RAMS were the cloud model developed under the direction of Dr. Cotton and the mesoscale model developed under the direction of Dr. Roger A. Pielke. The RAMS development began in 1986 with the goal of a unified multi-purpose modeling system. From that time, several versions of RAMS have been created always with the idea of improving its capabilities. Presently the RAMS development is conducted primarily by Drs. Craig J. Tremback and Robert L. Walko (Tremback and Walko, 1991). This model is considered as a general and flexible modeling system rather than a single purpose model since current research includes atmospheric scales ranging from $\Delta x = 100$ m, which are the scale of large eddy simulations, to scales of large convective systems where $\Delta x = 100$ km (Tremback et al., 1986). This comprehensive meteorological modeling system (RAMS) at CSU contains many options and a range of applications from which we can cite applications to large eddy simulations (LES), simulations of thunderstorms, mesoscale convective systems, and mesoscale atmospheric dispersion (Pielke et al., 1992). In this study the version of RAMS called 2c (Tremback and Walko, 1991) is used in the simulations, with a 1 km $\times$1 km grid.

4.2 Evaluation of Mesoscale and Subgrid Scale Heat Fluxes

The evaluation of vertical heat fluxes from earth's surface to the atmosphere are of prime importance to planetary boundary layer (PBL) studies since they are directly related

to the mixed layer depth and cloud formation. Many researchers have parameterized the PBL as related to surface heat fluxes (Deardorff, 1966, 1972, 1974; Saltzman and Ashe, 1976; Brook, 1978; Louis, 1979; Frank and Emmitt, 1981; Nicholls and Smith, 1982; Businger, 1982; Sud and Smith, 1984; Troen and Mahrt, 1986; Mahrt, 1986, 1987; Pielke et al., 1991; and others).

In this study, since the RAMS simulations were carried out over a nonhomogeneous surface for complex and flat terrain, the vertical heat fluxes were calculated following the method used by Pielke et al., (1991). They considered that the domain-averaged total vertical heat flux is represented by the sum of the resolvable mesoscale circulation ($w'\theta'$) and the subgrid-scale contributions ($\overline{w''\theta''}$) as follows:

$$< w'\theta' >_D + < \overline{w''\theta''} >_D \tag{4.1}$$

They defined the domain average used for cyclic lateral boundary conditions as:

$$< w >_D = \frac{1}{N_x} \sum_{i=1}^{N_x} w_i \tag{4.2}$$

And,

$$< \theta >_D = \frac{1}{N_x} \sum_{i=1}^{N_x} \theta_i \tag{4.3}$$

Here $< >_D$ indicates the domain average, w_i and θ_i represent these quantities at grid points, and N_x is the total numbers of horizontal points in the domain. Finally. Pielke et al. (1991) defined the resolvable ($< w'\theta' >_D$) heat flux as:

$$< w'\theta' >_D = < (w - < w >_D)(\theta - < \theta >_D) >_D \tag{4.4}$$

and the subgrid-scale ($< \overline{w''\theta''} >_D$) heat flux will be evaluated with a relationship defined according to Pielke (1984) as follows:

$$< \overline{w_s''\theta_s''} >_D = - < u_*\theta_* >_D \tag{4.5}$$

where $\overline{w_s''\theta_s''}$ is the subgrid-scale heat flux at surface, u_* is the *friction velocity*, and θ_* is called the *flux temperature*. When the surface layer is superadiabatic ($\frac{\partial\overline{\theta}}{\partial z} < 0$) a simplified boundary layer formulation can be used to estimate the fluxes; this formulation is called a *jump* model (Deardorff, 1974; Pielke, 1984). In this model, the potential temperature has a discontinuity just at the top of the boundary layer (Z_i). Between the surface and this height (Z_i) the subgrid-scale heat fluxes are assumed to change linearly with the height, reaching its minimum value at Z_i. To obtain the heat flux at Z_i in terms of the surface heat flux, the closure assumption (Deardorff, 1974; Pielke, 1984) often made is:

$$< \overline{w_{Z_i}''\theta_{Z_i}''} >_D = -\alpha < \overline{w_s''\theta_s''} >_D = +\alpha < u_*\theta_* >_D \tag{4.6}$$

Here $\alpha = 0.2$ and $\overline{w_{Z_i}''\theta_{Z_i}''}$ is the heat flux at Z_i. The domain-averaged subgrid-scale heat fluxes [$< \overline{w_Z''\theta_Z''} >_D$] at some level Z can be written as a function of the domain-averaged heat flux at surface [$< \overline{w_s''\theta_s''} >_D$] and the domain-averaged height of the planetary boundary layer ($< Z_i >_D$), by means of the following linear relationship:

$$< \overline{w_Z''\theta_Z''} >_D = -\frac{< \overline{w_s''\theta_s''} >_D [Z(\alpha+1) - < Z_i >_D]}{< Z_i >_D} \tag{4.7}$$

In Equation (4.7), two boundary conditions take place:

$$(i)\ When\ Z = 0,\ < \overline{w_0''\theta_0''} >_D = < \overline{w_s''\theta_s''} >_D$$

that is the heat flux at surface, and

$$(ii)\ When\ Z = Z_i,\ < \overline{w_{Z_i}''\theta_{Z_i}''} >_D = -\alpha < \overline{w_s''\theta_s''} >_D$$

which is the heat flux at Z_i that was previously stated in Equation (4.6). Using Equation (4.7), by linear interpolation, the domain-averaged subgrid-scale vertical heat fluxes are calculated.

4.2.1 RAMS Initialization and Model Set Up

To perform the 3-D simulations, the RAMS was initialized in its nonhydrostatic and horizontally homogeneous form. The Klemp-Wilhelmson (1978a,b) lateral boundary conditions and a wall on top were assumed. The surface layer and soil parameterizations were activated using the soil model of Tremback-Kessler (1985). The horizontal grid increments were 1 km and the vertical grid was stretched by a factor of 1.25 to obtain 25 vertical levels. The lowest level was -25.3 m and the highest 14625.6 m. In addition, initial thermodynamic composite soundings for winter and summer cases were obtained using data from 72374 (INW) Flagstaff, AZ; 72476 (GJT) Grand Junction, CO; 72486 (ELY) Ely, NV; and 72572 (SLC) Salt Lake City, UT at 1200 UTC for 10 February 1986 and 7 June 1986. In these averaged soundings, temperature inversions were excluded and no synoptic wind was assumed. These conditions were necessaries in order to have: First, an atmosphere with an standard lapse rate of temperature (temperature decreasing with the high). Secondly, the no synoptic wind assumption was considered to avoid the effect of advection of other meteorological variables such as pressure, temperature and moisture. The most important model characteristics are summarized in Table 4.1.

The soil type selected for the simulations was sandy clay loam, one of the dominant soil types of the Coconino Plateau. However, other types such as sand, sandy clay, and clay were also tested in RAMS resulting in almost the same patterns, shapes, and order of magnitude of the predicted fields of $\vec{V}_h$, θ, and w. This apparent lack of sensitivity to soil type can be explained since, the input values of albedo are a function of space and time $[A(x, y, t)]$ such that the albedo already represents the major effect of the different types of soils when dry conditions exist.

4.3 The 3-D Simulations

A total of 8 three-dimensional (3-D) runs were performed using RAMS; 4 runs for the winter case and 4 for the summer case (Table 4.2). In both cases the topography (complex terrain) and real albedo values were taking into account. These real albedo values (as function of time and space) were also used for the case when a flat terrain was

Table 4.1: Model characteristics used in RAMS for the study site A_1.

Parameter	Characteristic
Δx,Δy	1 km
Δt	10 s
Horizontal domain	100×100 km^2
Vertical levels	25
Atmosphere	Nonhydrostatic, horizontally homogeneous
Lateral boundary conditions	Klemp-Wilhelmson (1978a,b)
Upper boundary conditions	Wall on top
Albedo	$\overline{A}(t)$ and $A(x,y,t)$
Soil type	Sandy clay loam
Soil model	Tremback-Kessler (1985)
Soil Moisture	Summer 10% saturated, Winter 5% sat.
Radiation Type	Mahrer-Pielke (1977)
Synoptic wind	0 m s^{-1}
Turbulence closure	Smagorinsky Deformation K (Tripoli,1986)
Initialization	Average Soundings from GJT,SLC,ELY,INW
Initial time	1500 UTC (0800 LST)
Run time	9 hours

assumed. The fields predicted were $\vec{V}_h$, w, and θ from which the vertical heat fluxes were calculated.

On average, a total of 80 plots (graphics) of the meteorological variables were obtained per run, this means about 640 plots for all simulations. Because of these large amount of figures, in this chapter only the most important features of the horizontal wind ($\vec{V}_h$) and vertical velocity (w) are presented. Composite figures for these two variables will be displayed for each season for the different albedo variabilities for complex and for flat terrain. For instance, the distribution of vertical velocity (w) will be depicted for the different cases that correspond to the same hour of simulation. The wind vector field will be displayed to show horizontal circulation. Notice that the initial time for winter, is one hour later than the others because the satellite data from 0800LST was discarded due to errors in the satellite data (Table 4.2).

In general, the distribution of the variables w and $\vec{V}_h$ will be depicted on the vertical cross section (x,z) and over horizontal (x,y) planes respectively. For the vertical cross section the plane (x,z) was placed at $y = -0.5$ km from the center of the domain, just

Table 4.2: Simulations performed in RAMS for the study site A_1.

Run No.	Space Dim.	Case	Topography type	Albedo	Initial time(LST)
1	3-D	winter	complex	$\bar{A}(t)$	0800
2	3-D	winter	flat	$\bar{A}(t)$	0800
3	3-D	summer	complex	$\bar{A}(t)$	0800
4	3-D	summer	flat	$\bar{A}(t)$	0800
5	3-D	winter	complex	$A(x,y,t)$	0900
6	3-D	winter	flat	$A(x,y,t)$	0900
7	3-D	summer	complex	$A(x,y,t)$	0800
8	3-D	summer	flat	$A(x,y,t)$	0800

along the latitude of 35.46°N. For the cases when a flat terrain was assumed, the elevation of the surface was placed at 1852 m, the average of all elevations in the entire domain.

4.3.1 The Horizontal Circulation ($\vec{V}_h$)

In general, the TOPO cases showed more organized circulation and wind patterns than the NOTOPO events for both seasons (Figures 4.1b, 4.1d, 4.2b, and 4.2d). The patterns of streamlines in the TOPO events showed well defined and larger confluence and difluence lines than the NOTOPO cases. Most of the flow at this time was simulated as blowing from the northwest, however, east and southeasterly flow was present over the south and southeast region of the domain, just over the area where the variation in elevation was higher (Figure 3.2). Nevertheless, in the summer case, the NOTOPO cases displayed more symmetric shapes of circulation than the TOPO events (Figures 4.2a and 4.2c). In the winter case, the circulation for the NOTOPO $A(x,y,t)$ (Figure 4.1c) depicted lesser areas with well defined circulation than the summer case. Furthermore, for the NOTOPO case and mean albedo as a function of time but with no spatial variation (Figure 4.1a), the pattern depicted a constant flow from the north northwest direction (NNW) with very weak intensity. This kind of steady flow was predicted by RAMS because it randomly perturbs momentum fluxes when the wind is near zero. These random momentum fluxes directly feed into the heat fluxes as we'll see later.

Maximum intensities of $\vec{V}_h$ at levels $Z_1 = 60$ m and $Z_7 = 1548$ m for the winter (Figures 4.3a and b) and summer cases (Figures 4.3c and d) were also calculated. These

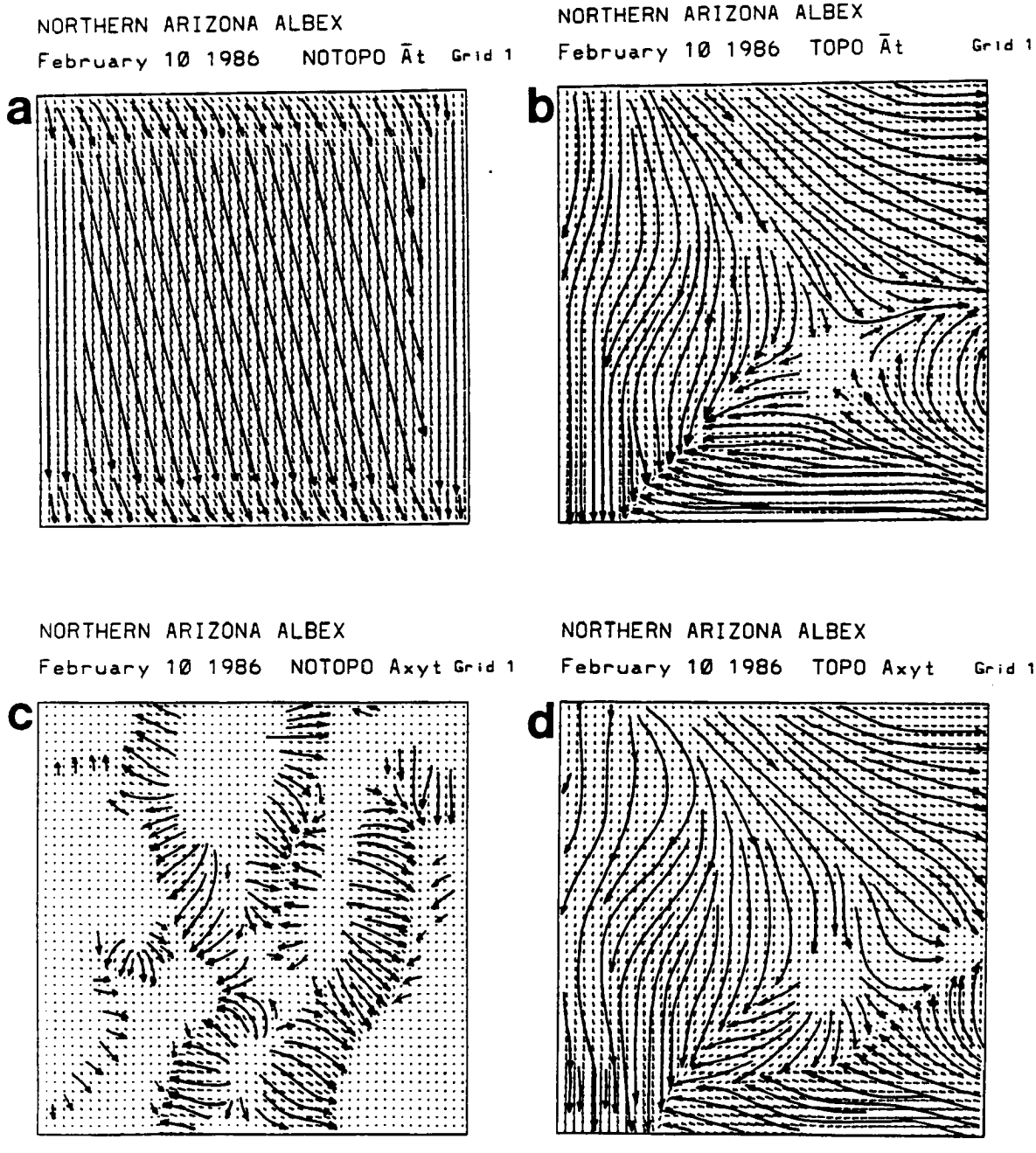

Figure 4.1: Subjective analysis of streamlines of the horizontal flow ($\vec{V}_h$) for the winter case at 1300 LST at height $Z = 28.3$ m for area A_1: (a) NOTOPO $\overline{A}(t)$, (b) TOPO $\overline{A}(t)$, (c) NOTOPO $A(x, y, t)$, and (d) TOPO $A(x, y, t)$.

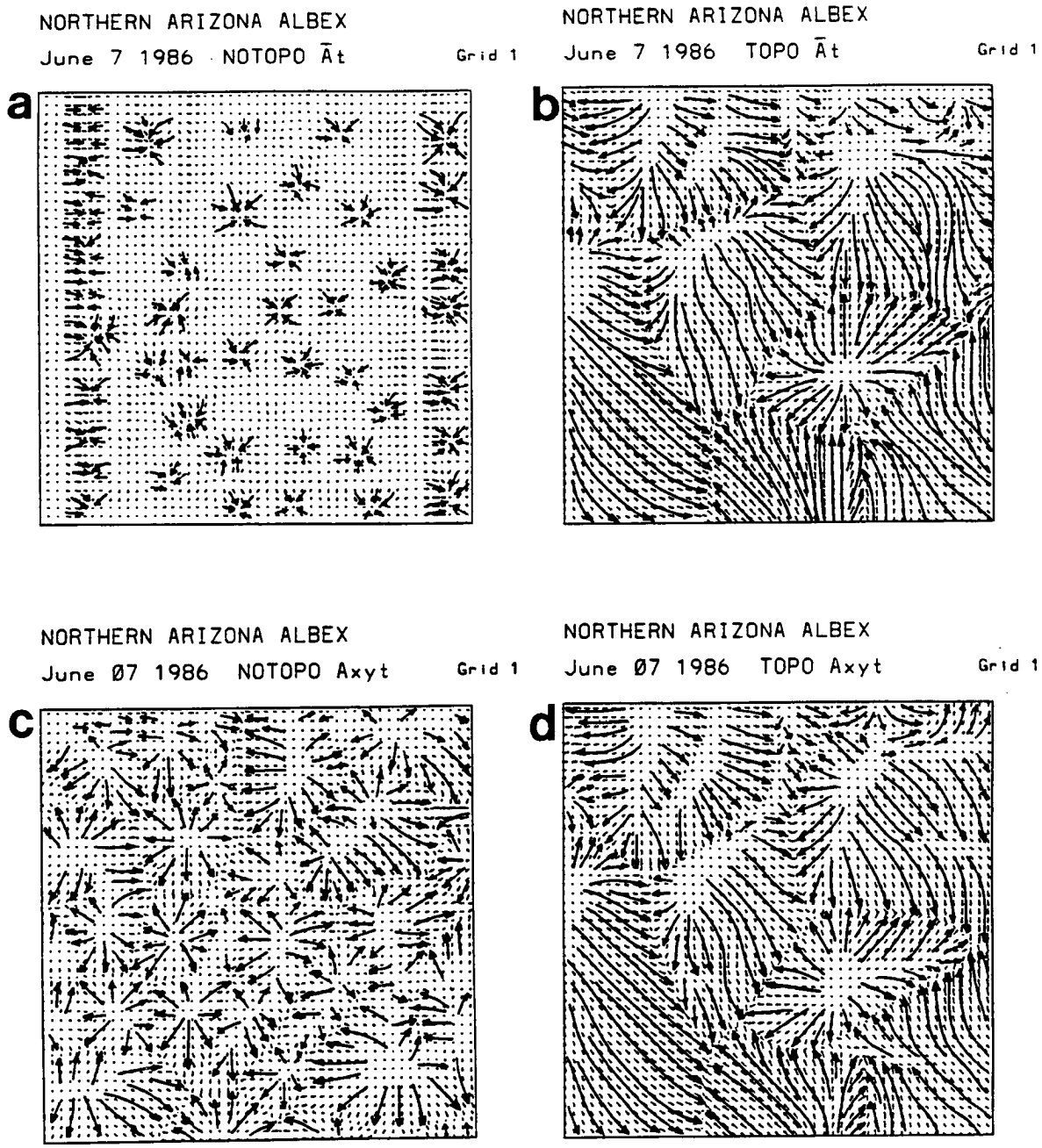

Figure 4.2: Subjective analysis of streamlines of the horizontal flow ($\vec{V}_h$) for the summer case at 1300 LST at height $Z = 28.3$ m for area A_1: (a) NOTOPO $\overline{A}(t)$, (b) TOPO $\overline{A}(t)$, (c) NOTOPO $A(x, y, t)$, and (d) TOPO $A(x, y, t)$.

levels were chosen in order to give an a idea of the magnitude of the horizontal circulation close to the surface (Z_1) and at some level with a height somewhat above the surface (Z_7). In general, the profiles of maximum speeds showed that the TOPO cases reached greater values of $|\vec{V}_h|$ compared with the NOTOPO cases, with the exception of the NOTOPO $A(x,y,t)$ event for the summer case, which had the maximum peak. For both seasons, the magnitude of $\vec{V}_h$ were about the same order, that is, around 10-15 m s^{-1} for the TOPO cases and both types of albedo variations. The NOTOPO cases had the smallest values. For instance, the NOTOPO $\overline{A}(t)$ case for the winter case achieved intensities less than 0.5 m s^{-1} (Table 4.3).

Table 4.3: Absolute maximum speeds of $\vec{V}_h$ over the entire domain for the winter and summer cases for area A_1, at model levels $Z_1 = 60$ m and $Z_7 = 1548$ m. Here $\overline{A}(t)$ is the mean albedo varying as a function of time and $A(x,y,t)$ is the real albedo.

Case	Topo. Type	Albedo	$\|\vec{V}_{h_{max}}\|$(m s^{-1})Z_1	$\|\vec{V}_{h_{max}}\|$(m s^{-1})Z_7
Winter	Complex	$\overline{A}(t)$	11.25	14.69
Winter	Flat	$\overline{A}(t)$	00.23	00.09
Winter	Complex	$A(x,y,t)$	12.40	12.56
Winter	Flat	$A(x,y,t)$	06.25	04.22
Summer	Complex	$\overline{A}(t)$	13.84	12.70
Summer	Flat	$\overline{A}(t)$	09.20	05.06
Summer	Complex	$A(x,y,t)$	13.88	12.37
Summer	Flat	$A(x,y,t)$	16.26	09.88

4.3.2 The Vertical Velocity (w)

As we saw in the previous section, as a consequence of the differences in heating of the earth's surface, which is controlled in the model by albedo and terrain variability, significant horizontal circulations were generated in most of the cases. These circulations produce vertical velocity (w) that will be evaluated in this section for the winter and summer cases. Where albedo varied as a function of space and time over a flat surface, there were more organized cells than the other cases (Figure 4.4c). The TOPO events for both types of albedo variations displayed weak convective plumes with depths no more than 1 km (Figures 4.4b and d). The NOTOPO $\overline{A}(t)$ event depicted the weakest vertical

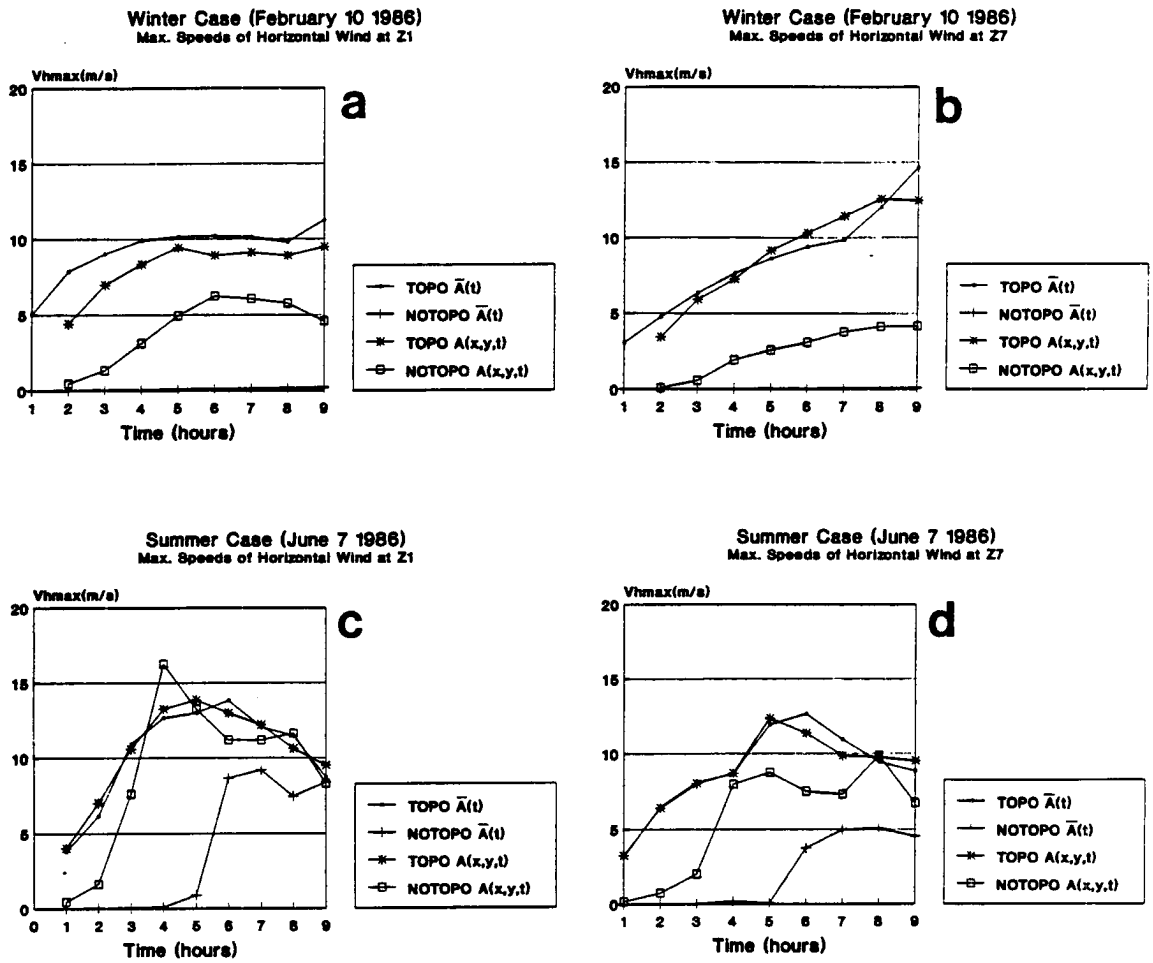

Figure 4.3: Maximum intensities of $\vec{V}_h$ at levels $Z_1 = 60$ m and $Z_7 = 1548$ m for area A_1: (a)-(b) winter case and (c)-(d) summer case.

motion and few traces of cells were present not only at this time but for all periods of the simulation (Figure 4.4a).

In the summer case, in general, complex and flat terrain displayed stronger vertical motions than the winter case (Figure 4.5). Also, they showed a greater number of deeper cells that expanded the boundary layer to as much as 3.5 km of height. This marked difference was expected, however, the interesting point of comparison is with respect to the albedo variations over complex and flat terrain in the same season. For instance, for albedo variations as a function of space and time (Figures 4.5c and d), the TOPO and NOTOPO cases showed differences in the number of plumes. The NOTOPO case developed almost twice the number of cells than those generated over complex terrain. However, the maximum intensities of w for the NOTOPO case were smaller than the TOPO case. This feature was also observed for the case when the mean albedo varied as a function of time but no spatial variation. In this point, even though the NOTOPO $\overline{A}(t)$ case does not show important w intensities (Figure 4.5a), one hour later (1400 LST) it developed several well defined circulation eddies. Remember that the development of circulation for this case is a result of the imposition in RAMS of an algorithm to produce random heat flux values when the wind is very light. Over time, the results are circulations that develop in a similar manner to large eddy simulations (e.g., Hadfield et al., 1991). Another interesting feature was the heights reached for the plumes. In general, the cells in the NOTOPO cases reached deeper heights than the TOPO cases. For example, in the TOPO cases the maximum depth reached was 2.7 km at 1400 LST. Meanwhile in the NOTOPO case it was about 3.0 km at the same hour.

The magnitudes of w at level $Z_1 = 60$ m were less than 1 m s^{-1} in both seasons (Figure 4.6). At model level $Z_6 = 1191$ m, the magnitudes of w reached significant values mainly for the TOPO cases for both types of albedo variations (Figure 4.7). The order of magnitude for the maximum values was about 3 m s^{-1} for the winter case and around 7 m s^{-1} for the summer case. That is, the speeds in the summer case were about two times larger than the winter case. In addition, the atmosphere responds with significant ascent after the first hour for the summer case (Figure 4.7b); meanwhile in the winter case,

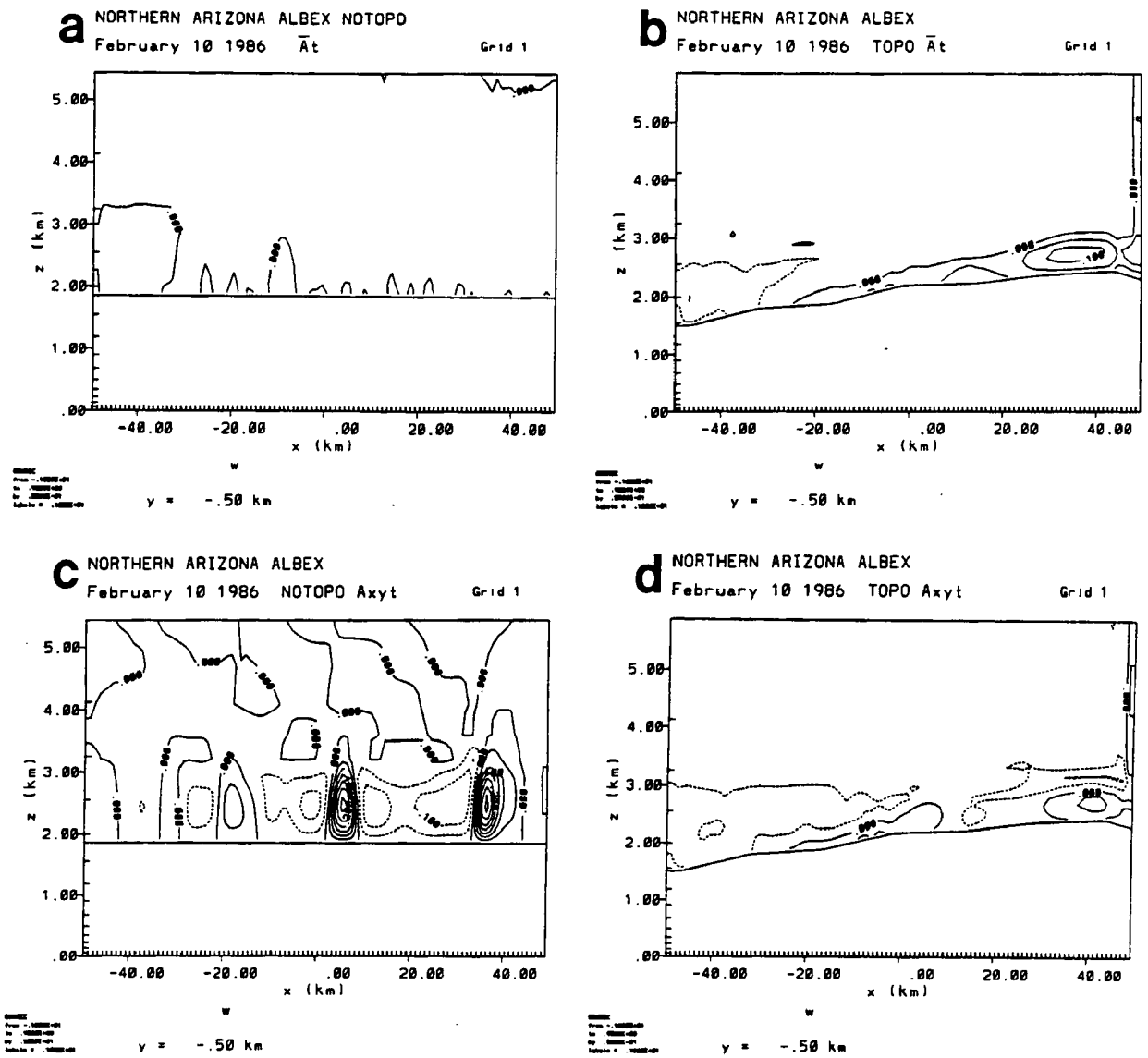

Figure 4.4: East-west cross sections of w (along 35.46°N) for the winter case at 1300 LST for area A_1: (a) NOTOPO $\overline{A}(t)$, (b) TOPO $\overline{A}(t)$, (c) NOTOPO $A(x,y,t)$, and (d) TOPO $A(x,y,t)$. The contour intervals are 5 cm s^{-1}.

motion and few traces of cells were present not only at this time but for all periods of the simulation (Figure 4.4a).

In the summer case, in general, complex and flat terrain displayed stronger vertical motions than the winter case (Figure 4.5). Also, they showed a greater number of deeper cells that expanded the boundary layer to as much as 3.5 km of height. This marked difference was expected, however, the interesting point of comparison is with respect to the albedo variations over complex and flat terrain in the same season. For instance, for albedo variations as a function of space and time (Figures 4.5c and d), the TOPO and NOTOPO cases showed differences in the number of plumes. The NOTOPO case developed almost twice the number of cells than those generated over complex terrain. However, the maximum intensities of w for the NOTOPO case were smaller than the TOPO case. This feature was also observed for the case when the mean albedo varied as a function of time but no spatial variation. In this point, even though the NOTOPO $\overline{A}(t)$ case does not show important w intensities (Figure 4.5a), one hour later (1400 LST) it developed several well defined circulation eddies. Remember that the development of circulation for this case is a result of the imposition in RAMS of an algorithm to produce random heat flux values when the wind is very light. Over time, the results are circulations that develop in a similar manner to large eddy simulations (e.g., Hadfield et al., 1991). Another interesting feature was the heights reached for the plumes. In general, the cells in the NOTOPO cases reached deeper heights than the TOPO cases. For example, in the TOPO cases the maximum depth reached was 2.7 km at 1400 LST. Meanwhile in the NOTOPO case it was about 3.0 km at the same hour.

The magnitudes of w at level $Z_1 = 60$ m were less than 1 m s^{-1} in both seasons (Figure 4.6). At model level $Z_6 = 1191$ m, the magnitudes of w reached significant values mainly for the TOPO cases for both types of albedo variations (Figure 4.7). The order of magnitude for the maximum values was about 3 m s^{-1} for the winter case and around 7 m s^{-1} for the summer case. That is, the speeds in the summer case were about two times larger than the winter case. In addition, the atmosphere responds with significant ascent after the first hour for the summer case (Figure 4.7b); meanwhile in the winter case,

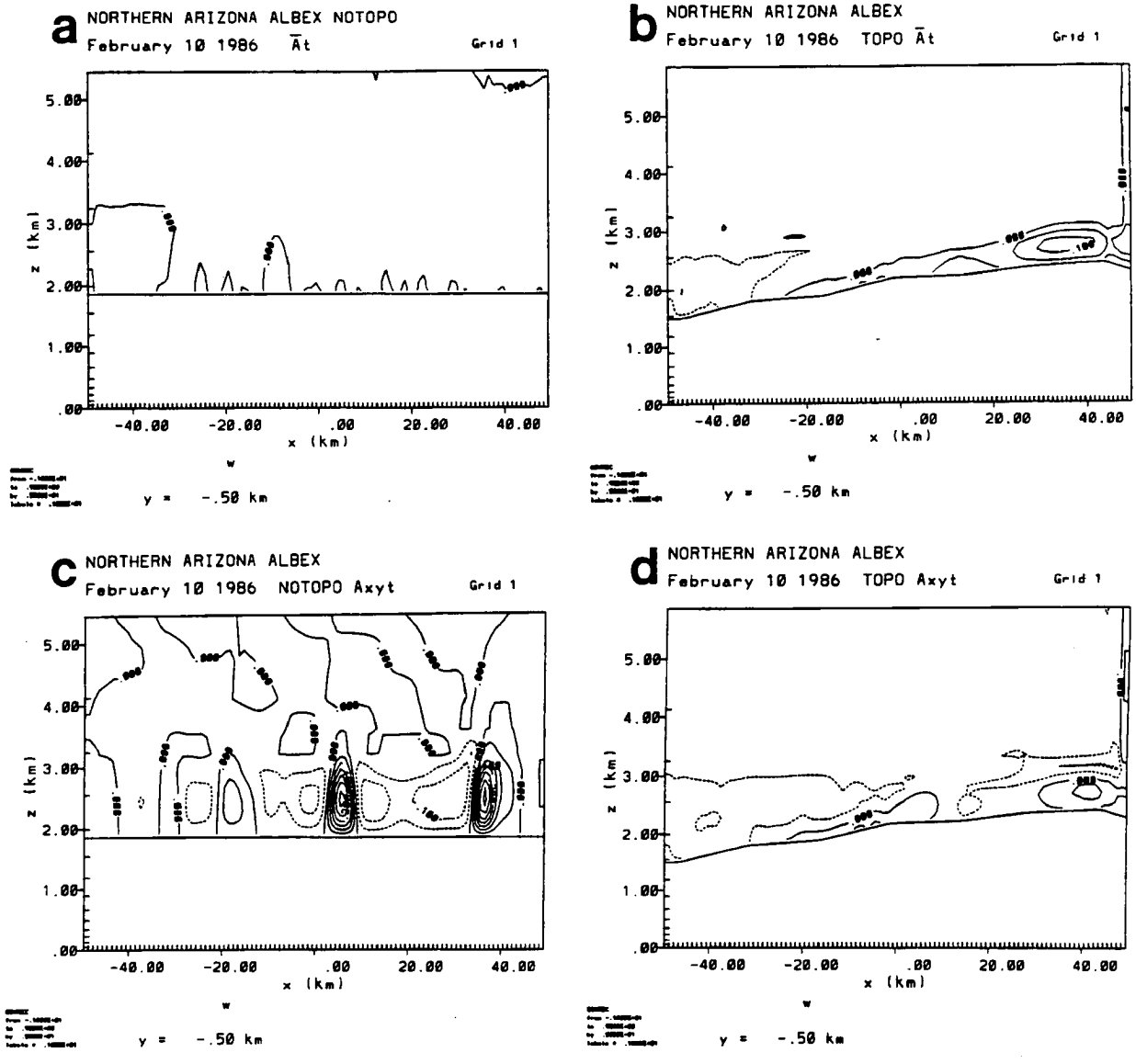

Figure 4.4: East-west cross sections of w (along 35.46°N) for the winter case at 1300 LST for area A_1: (a) NOTOPO $\overline{A}(t)$, (b) TOPO $\overline{A}(t)$, (c) NOTOPO $A(x, y, t)$, and (d) TOPO $A(x, y, t)$. The contour intervals are 5 cm s^{-1}.

motion and few traces of cells were present not only at this time but for all periods of the simulation (Figure 4.4a).

In the summer case, in general, complex and flat terrain displayed stronger vertical motions than the winter case (Figure 4.5). Also, they showed a greater number of deeper cells that expanded the boundary layer to as much as 3.5 km of height. This marked difference was expected, however, the interesting point of comparison is with respect to the albedo variations over complex and flat terrain in the same season. For instance, for albedo variations as a function of space and time (Figures 4.5c and d), the TOPO and NOTOPO cases showed differences in the number of plumes. The NOTOPO case developed almost twice the number of cells than those generated over complex terrain. However, the maximum intensities of w for the NOTOPO case were smaller than the TOPO case. This feature was also observed for the case when the mean albedo varied as a function of time but no spatial variation. In this point, even though the NOTOPO $\overline{A}(t)$ case does not show important w intensities (Figure 4.5a), one hour later (1400 LST) it developed several well defined circulation eddies. Remember that the development of circulation for this case is a result of the imposition in RAMS of an algorithm to produce random heat flux values when the wind is very light. Over time, the results are circulations that develop in a similar manner to large eddy simulations (e.g., Hadfield et al., 1991). Another interesting feature was the heights reached for the plumes. In general, the cells in the NOTOPO cases reached deeper heights than the TOPO cases. For example, in the TOPO cases the maximum depth reached was 2.7 km at 1400 LST. Meanwhile in the NOTOPO case it was about 3.0 km at the same hour.

The magnitudes of w at level $Z_1 = 60$ m were less than 1 m s^{-1} in both seasons (Figure 4.6). At model level $Z_6 = 1191$ m, the magnitudes of w reached significant values mainly for the TOPO cases for both types of albedo variations (Figure 4.7). The order of magnitude for the maximum values was about 3 m s^{-1} for the winter case and around 7 m s^{-1} for the summer case. That is, the speeds in the summer case were about two times larger than the winter case. In addition, the atmosphere responds with significant ascent after the first hour for the summer case (Figure 4.7b); meanwhile in the winter case,

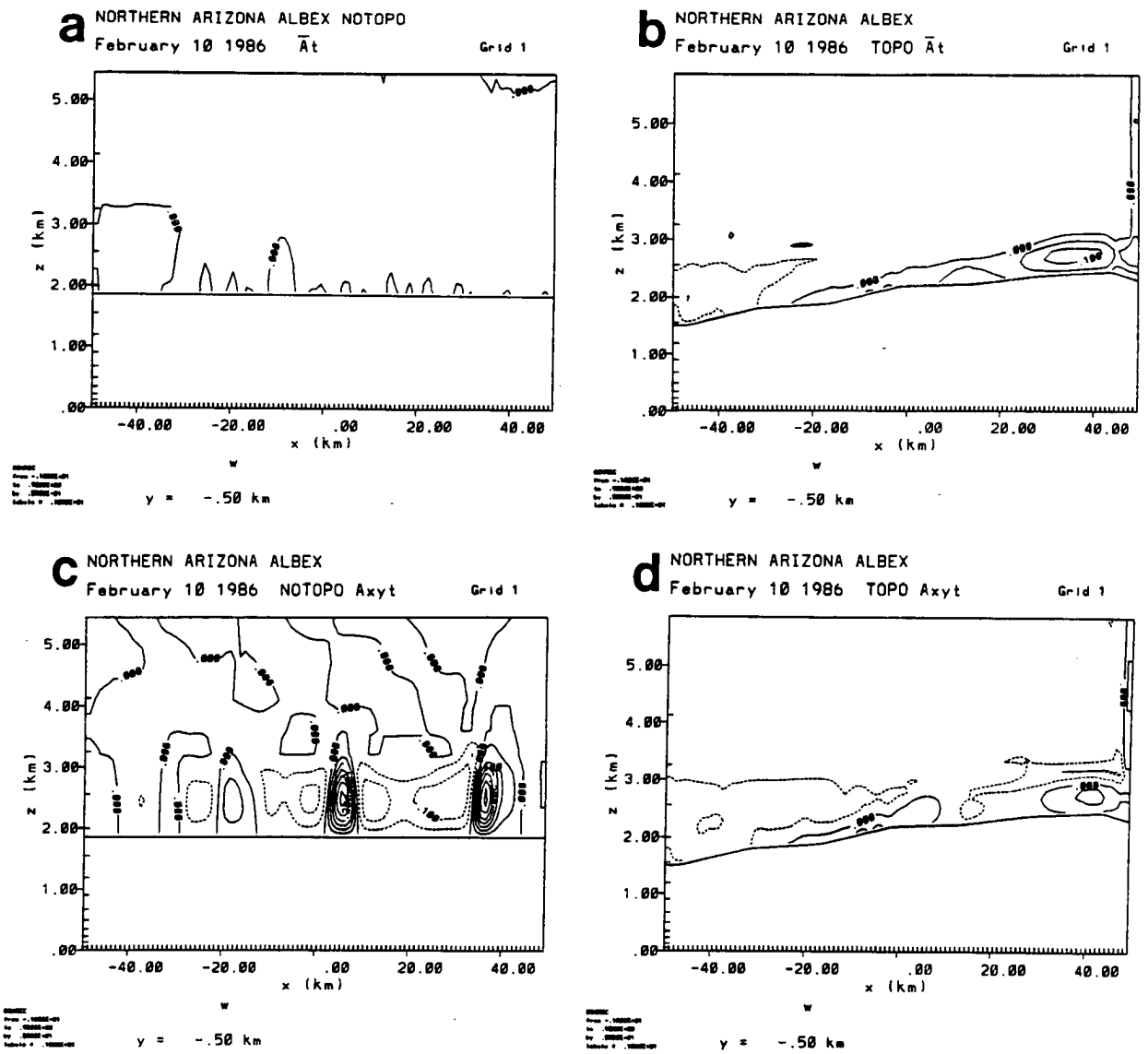

Figure 4.4: East-west cross sections of w (along 35.46°N) for the winter case at 1300 LST for area A_1: (a) NOTOPO $\overline{A}(t)$, (b) TOPO $\overline{A}(t)$, (c) NOTOPO $A(x,y,t)$, and (d) TOPO $A(x,y,t)$. The contour intervals are 5 cm s^{-1}.

motion and few traces of cells were present not only at this time but for all periods of the simulation (Figure 4.4a).

In the summer case, in general, complex and flat terrain displayed stronger vertical motions than the winter case (Figure 4.5). Also, they showed a greater number of deeper cells that expanded the boundary layer to as much as 3.5 km of height. This marked difference was expected, however, the interesting point of comparison is with respect to the albedo variations over complex and flat terrain in the same season. For instance, for albedo variations as a function of space and time (Figures 4.5c and d), the TOPO and NOTOPO cases showed differences in the number of plumes. The NOTOPO case developed almost twice the number of cells than those generated over complex terrain. However, the maximum intensities of w for the NOTOPO case were smaller than the TOPO case. This feature was also observed for the case when the mean albedo varied as a function of time but no spatial variation. In this point, even though the NOTOPO $\overline{A}(t)$ case does not show important w intensities (Figure 4.5a), one hour later (1400 LST) it developed several well defined circulation eddies. Remember that the development of circulation for this case is a result of the imposition in RAMS of an algorithm to produce random heat flux values when the wind is very light. Over time, the results are circulations that develop in a similar manner to large eddy simulations (e.g., Hadfield et al., 1991). Another interesting feature was the heights reached for the plumes. In general, the cells in the NOTOPO cases reached deeper heights than the TOPO cases. For example, in the TOPO cases the maximum depth reached was 2.7 km at 1400 LST. Meanwhile in the NOTOPO case it was about 3.0 km at the same hour.

The magnitudes of w at level $Z_1 = 60$ m were less than 1 m s^{-1} in both seasons (Figure 4.6). At model level $Z_6 = 1191$ m, the magnitudes of w reached significant values mainly for the TOPO cases for both types of albedo variations (Figure 4.7). The order of magnitude for the maximum values was about 3 m s^{-1} for the winter case and around 7 m s^{-1} for the summer case. That is, the speeds in the summer case were about two times larger than the winter case. In addition, the atmosphere responds with significant ascent after the first hour for the summer case (Figure 4.7b); meanwhile in the winter case,

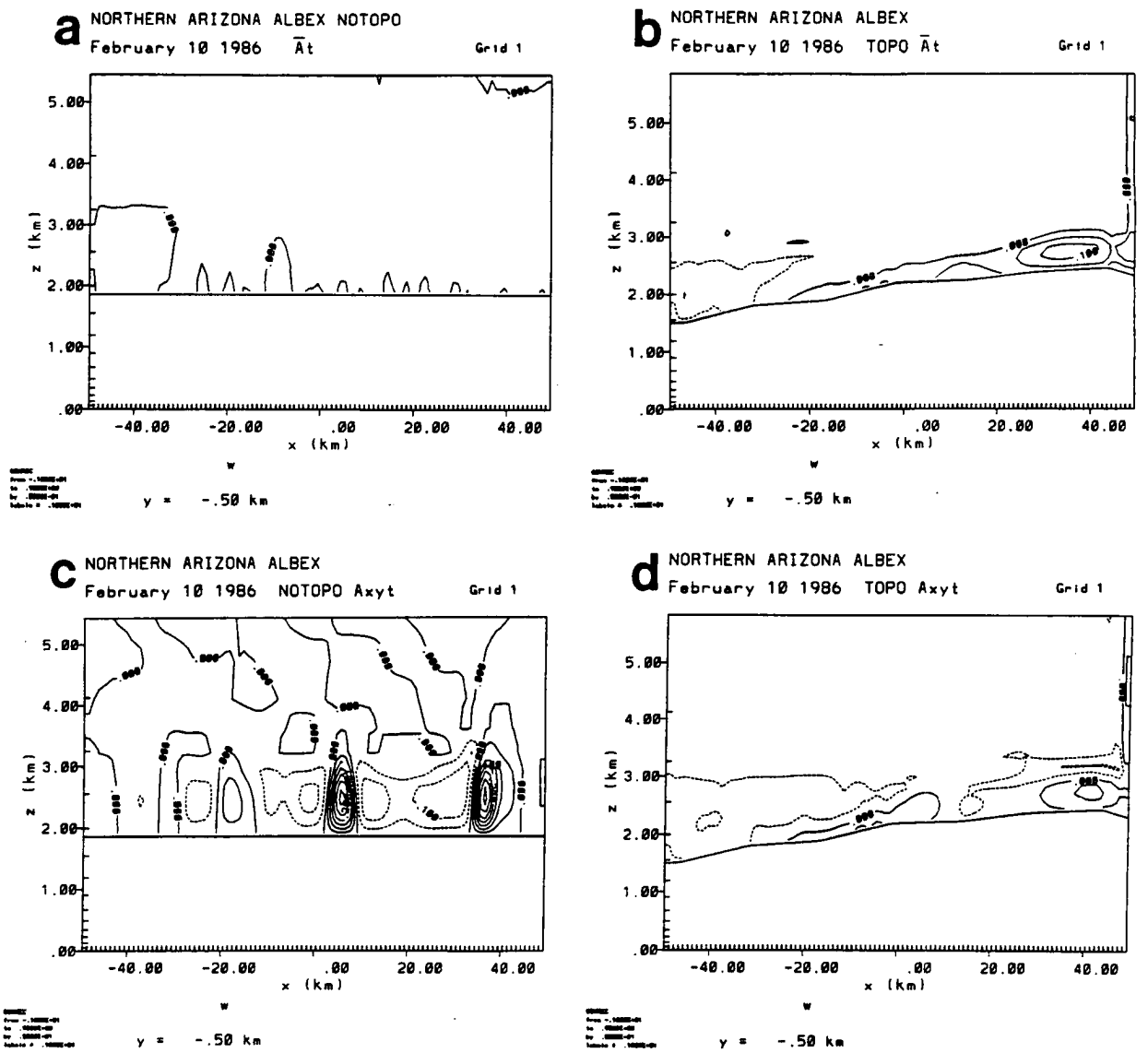

Figure 4.4: East-west cross sections of w (along 35.46°N) for the winter case at 1300 LST for area A_1: (a) NOTOPO $\overline{A}(t)$, (b) TOPO $\overline{A}(t)$, (c) NOTOPO $A(x, y, t)$, and (d) TOPO $A(x, y, t)$. The contour intervals are 5 cm s^{-1}.

motion and few traces of cells were present not only at this time but for all periods of the simulation (Figure 4.4a).

In the summer case, in general, complex and flat terrain displayed stronger vertical motions than the winter case (Figure 4.5). Also, they showed a greater number of deeper cells that expanded the boundary layer to as much as 3.5 km of height. This marked difference was expected, however, the interesting point of comparison is with respect to the albedo variations over complex and flat terrain in the same season. For instance, for albedo variations as a function of space and time (Figures 4.5c and d), the TOPO and NOTOPO cases showed differences in the number of plumes. The NOTOPO case developed almost twice the number of cells than those generated over complex terrain. However, the maximum intensities of w for the NOTOPO case were smaller than the TOPO case. This feature was also observed for the case when the mean albedo varied as a function of time but no spatial variation. In this point, even though the NOTOPO $\overline{A}(t)$ case does not show important w intensities (Figure 4.5a), one hour later (1400 LST) it developed several well defined circulation eddies. Remember that the development of circulation for this case is a result of the imposition in RAMS of an algorithm to produce random heat flux values when the wind is very light. Over time, the results are circulations that develop in a similar manner to large eddy simulations (e.g., Hadfield et al., 1991). Another interesting feature was the heights reached for the plumes. In general, the cells in the NOTOPO cases reached deeper heights than the TOPO cases. For example, in the TOPO cases the maximum depth reached was 2.7 km at 1400 LST. Meanwhile in the NOTOPO case it was about 3.0 km at the same hour.

The magnitudes of w at level $Z_1 = 60$ m were less than 1 m s^{-1} in both seasons (Figure 4.6). At model level $Z_6 = 1191$ m, the magnitudes of w reached significant values mainly for the TOPO cases for both types of albedo variations (Figure 4.7). The order of magnitude for the maximum values was about 3 m s^{-1} for the winter case and around 7 m s^{-1} for the summer case. That is, the speeds in the summer case were about two times larger than the winter case. In addition, the atmosphere responds with significant ascent after the first hour for the summer case (Figure 4.7b); meanwhile in the winter case,

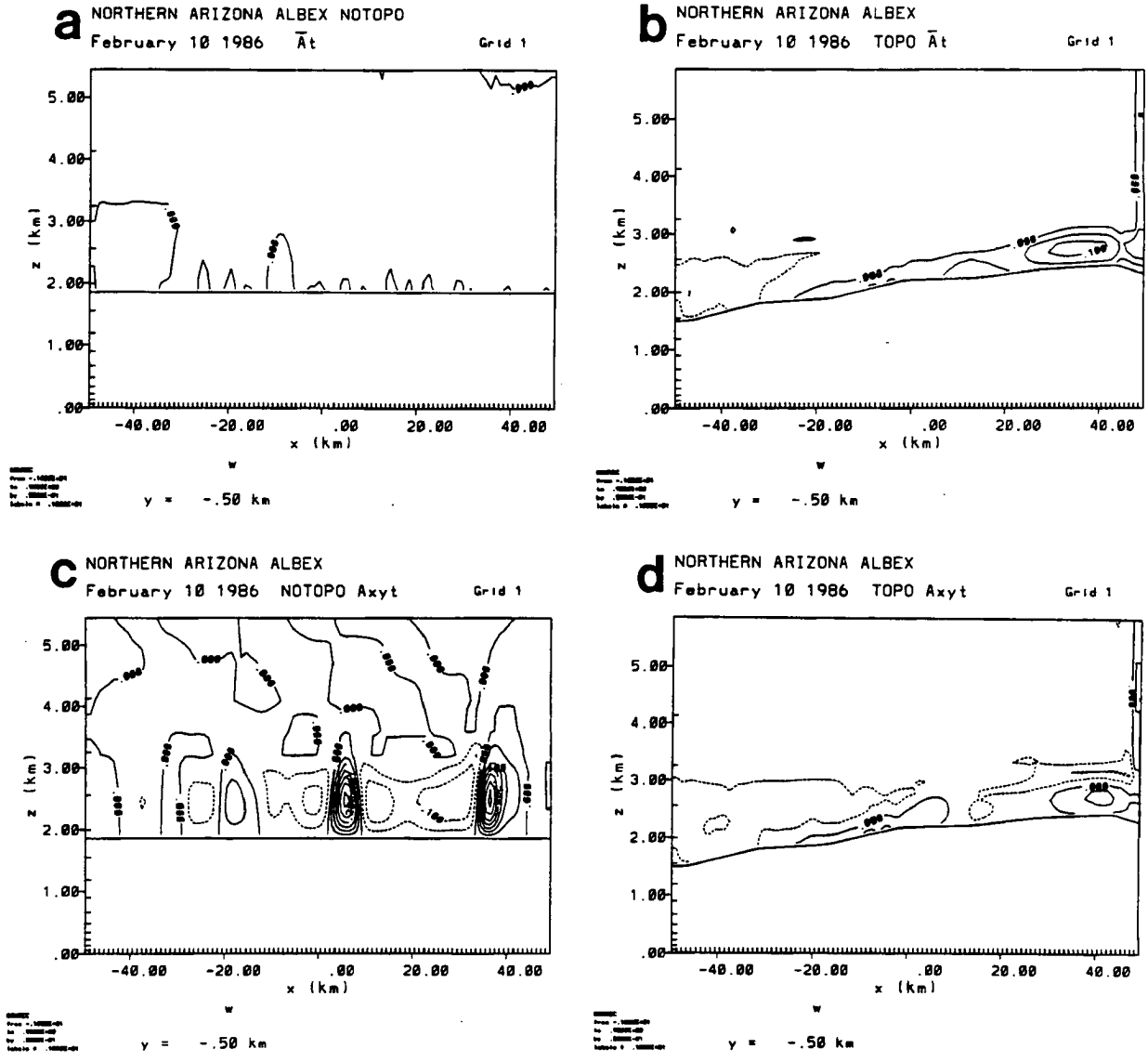

Figure 4.4: East-west cross sections of w (along 35.46°N) for the winter case at 1300 LST for area A_1: (a) NOTOPO $\overline{A}(t)$, (b) TOPO $\overline{A}(t)$, (c) NOTOPO $A(x, y, t)$, and (d) TOPO $A(x, y, t)$. The contour intervals are 5 cm s^{-1}.

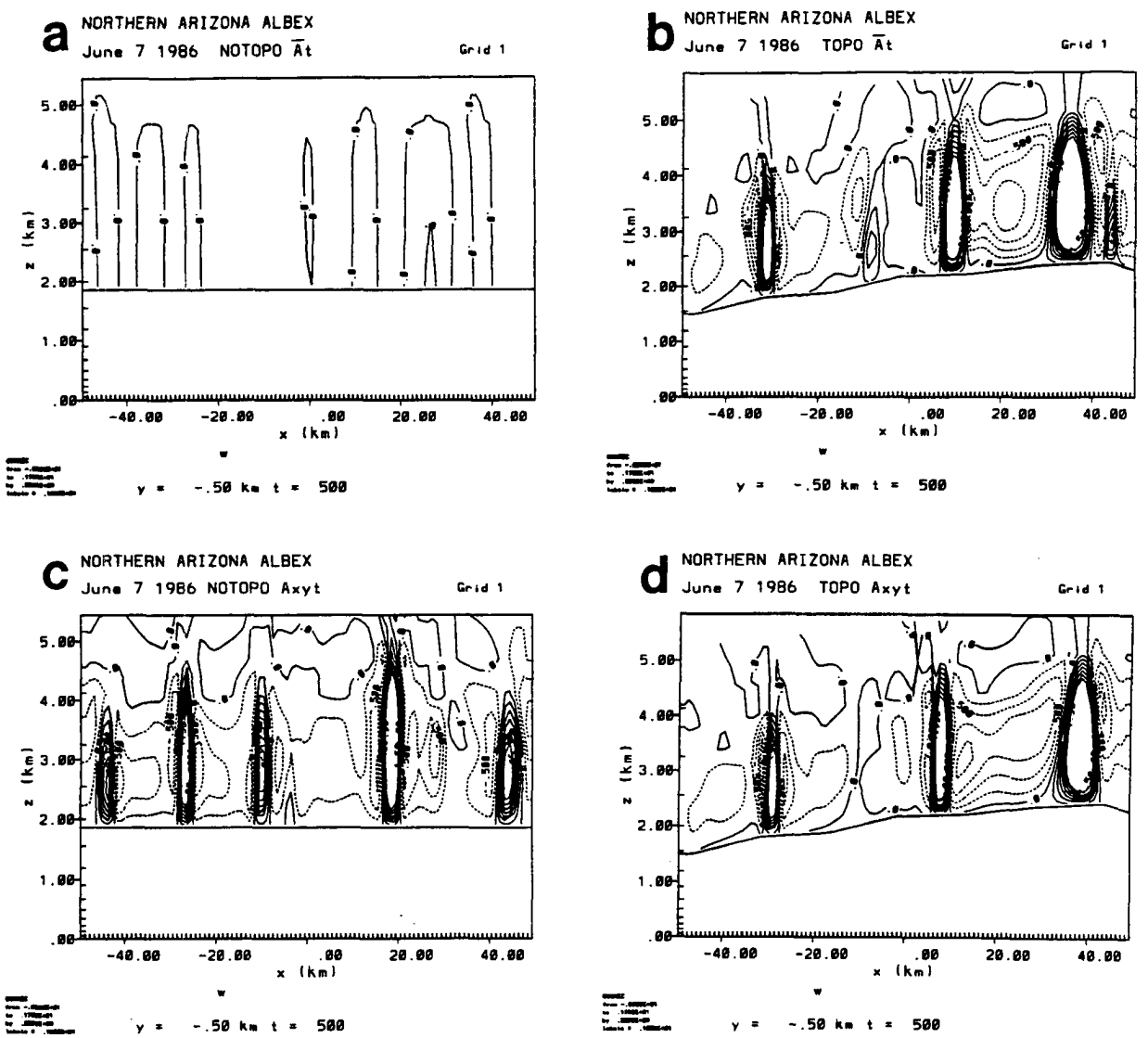

Figure 4.5: East-west cross sections of w (along 35.46°N) for the summer case at 1300 LST for area A_1: (a) NOTOPO $\overline{A}(t)$, (b) TOPO $\overline{A}(t)$, (c) NOTOPO $A(x,y,t)$, and (d) TOPO $A(x,y,t)$. Contour intervals are 25 cm s^{-1}.

it required about three hours to achieve significant values in heat fluxes. (Figure 4.7a). The maximum intensity of w in the winter case at model level $Z_8 = 1995$ m decreased to values less than 1 m s^{-1} (Figure 4.8). Meanwhile, in the summer case the magnitudes of w remained at about 7 m s^{-1}. This result was expected since in the summer the vertical currents are deeper than in the winter. The time at which the maximum peaks occurred was 6 and 7 hours after the initial time; this time is coincident with the period of maximum heating of the earth's surface.

In general, we can say that the maximum magnitudes of vertical motion during the summer case were about twice the intensity displayed for the winter case (Table 4.4). Vertical velocities in thermals can reach about 5 m s^{-1} or more, however, most updraft are of the order of 1 to 2 m s^{-1} (Stull, 1988). On the other hand, since the first hours of simulation, the summer case showed greater changes in the intensity of w with time than those displayed in the winter case. This means that the atmosphere achieves an earlier response in the summer case than in the winter due to greater availability of sensible heat from solar radiation. Note that vertical motion on the same order of magnitude is achieved independently with both terrain variability and albedo variability.

Table 4.4: Absolute maximum speeds of w for the entire domain (A_1) for the winter and summer cases, and heights and time at which they were reached. For flat an complex terrain and albedo variations of: $\overline{A}(t)$ mean albedo and $A(x,y,t)$ real albedo.

Case	Topography Type	Albedo	w_{max}(m s^{-1})	$Z(m)$	Time (LST)
Winter	Complex	$\overline{A}(t)$	3.68	904	1400
Winter	Flat	$\overline{A}(t)$	0.01	492	1500
Winter	Complex	$A(x,y,t)$	3.61	904	1400
Winter	Flat	$A(x,y,t)$	2.29	904	1400
Summer	Complex	$\overline{A}(t)$	6.76	1191	1300
Summer	Flat	$\overline{A}(t)$	6.06	1995	1400
Summer	Complex	$A(x,y,t)$	7.66	1548	1300
Summer	Flat	$A(x,y,t)$	7.31	1548	1400

4.3.3 The Z_i of the PBL

The top of the boundary layer (BL) usually is represented by the symbol Z_i and it is the height at which the inversion of potential temperature starts (Deardorff, 1972,

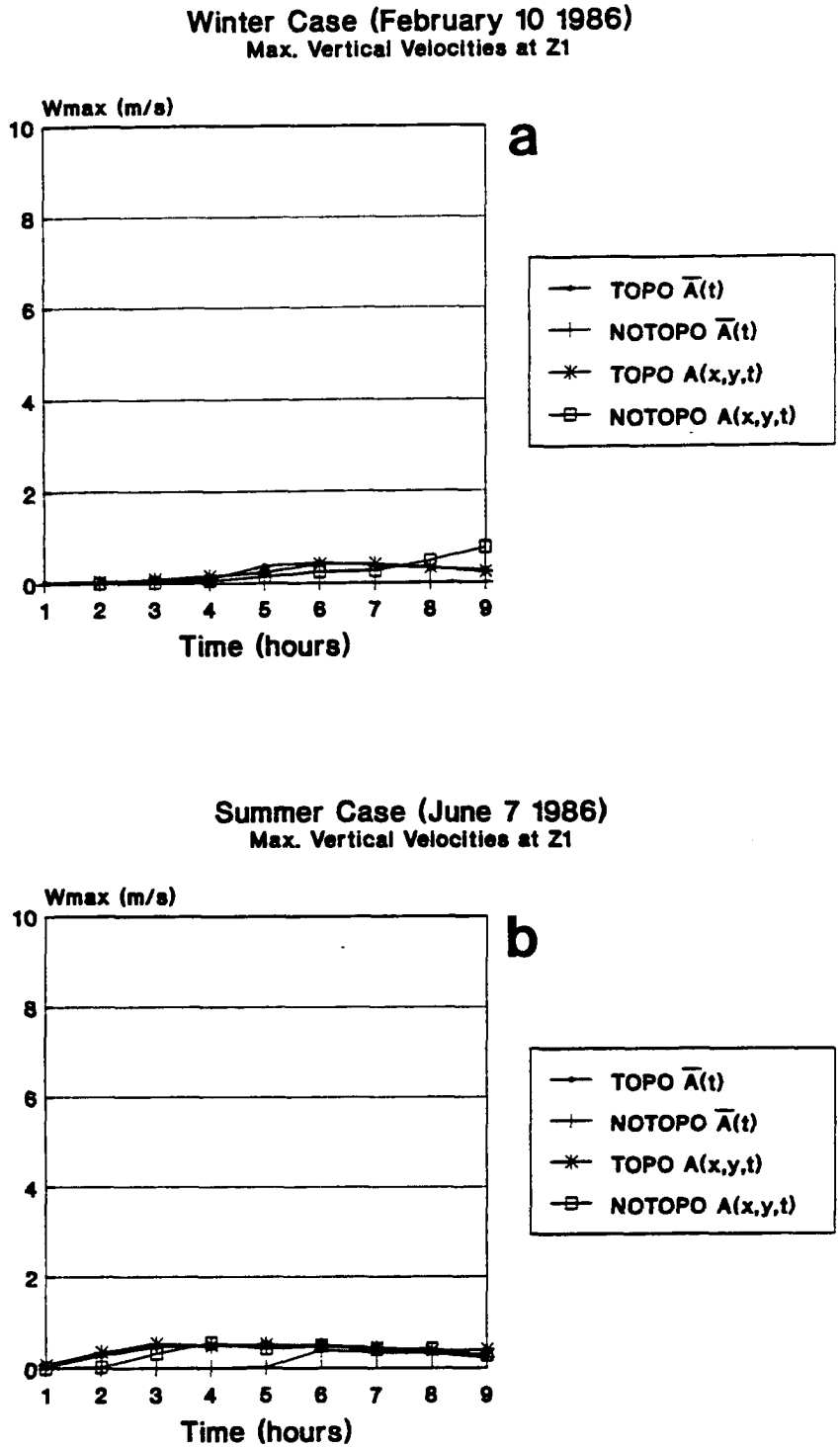

Figure 4.6: Maximum intensities of vertical velocity (w) at model level $Z_1 = 60$ m for area A_1: (a) winter case, and (b) summer case.

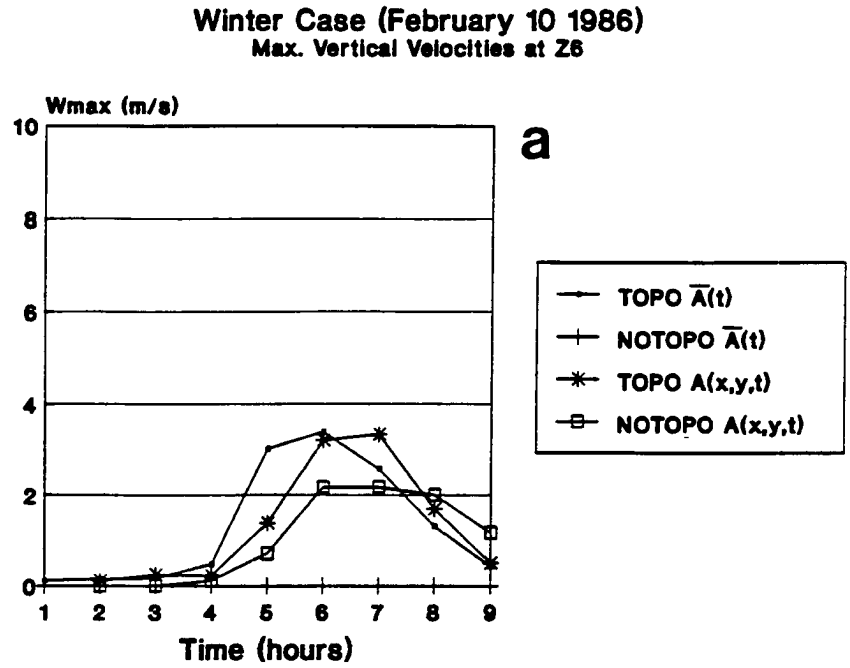

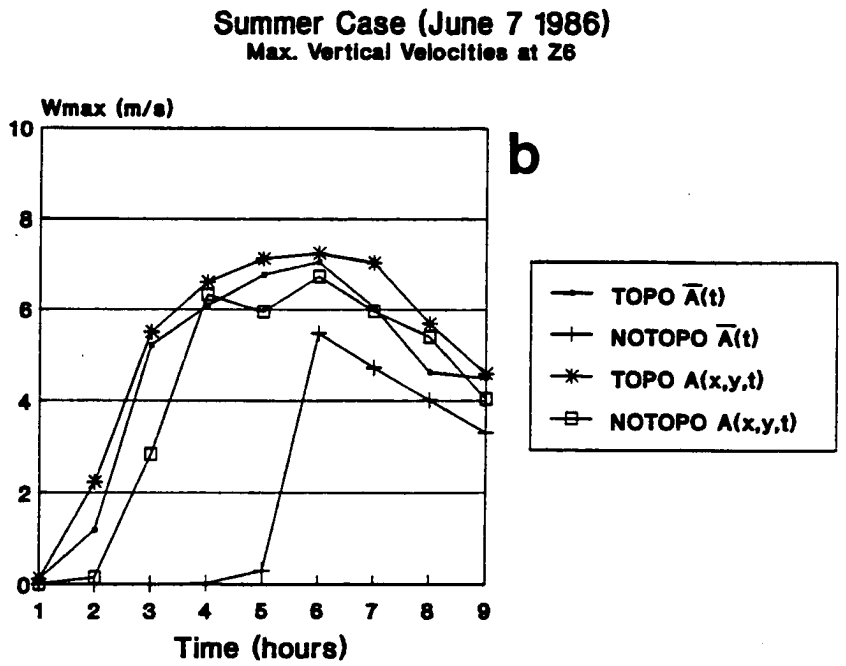

Figure 4.7: Maximum intensities of vertical velocity (w) at model level $Z_6 = 1191$ m for area A_1: (a) winter case, and (b) summer case.

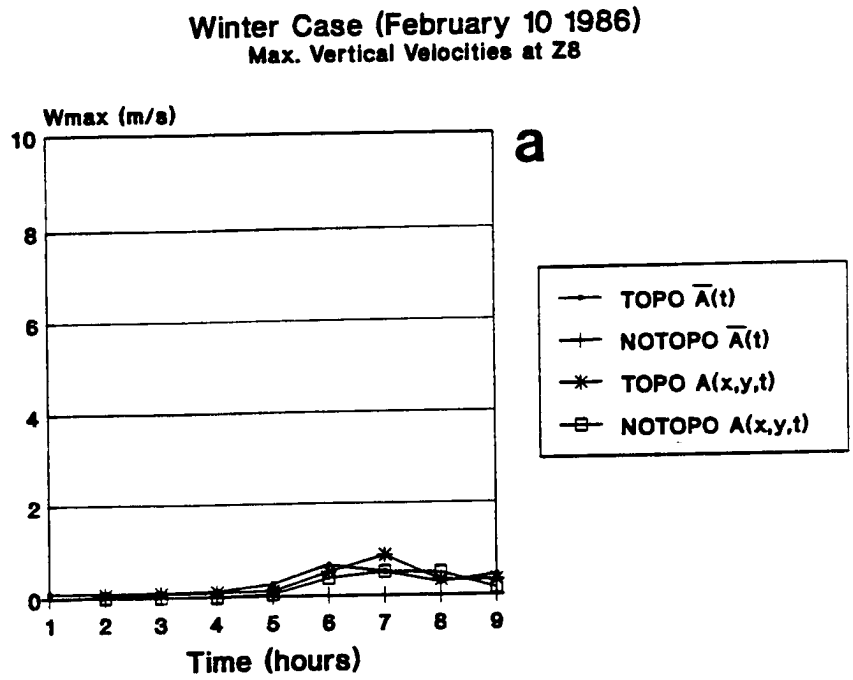

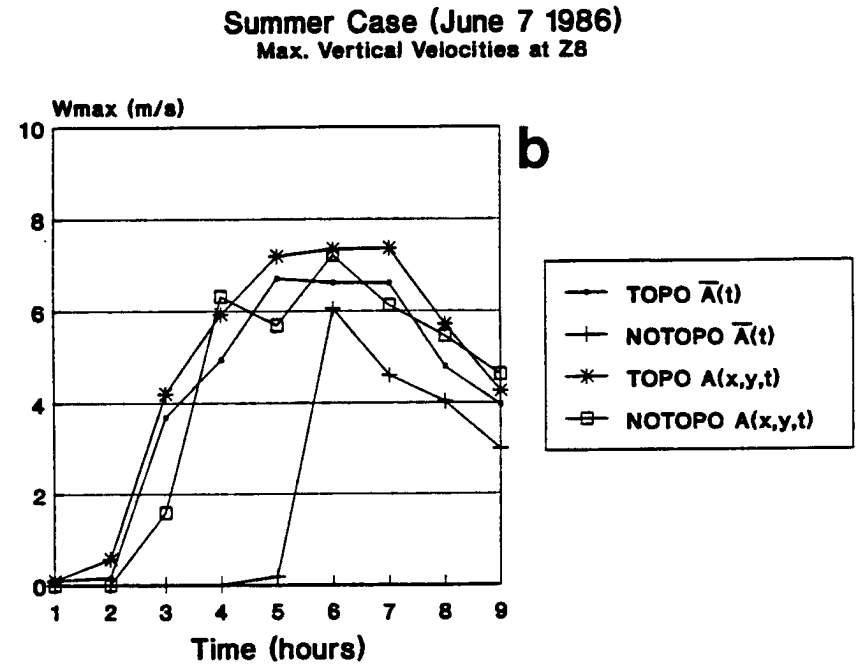

Figure 4.8: Maximum intensities of vertical velocity (w) at model level $Z_8 = 1995$ m for area A_1: (a) winter case, and (b) summer case.

1974; Pielke, 1984; Stull, 1988). The height of the boundary layer ranges from a few hundred meters to few kilometers depending on the condition of the overlaying atmospheric stability. The planetary boundary layer tends to be well mixed when the surface receives more heat during the summer which can cause deeper convective currents than during the winter. Pielke (1984) defines the Z_i as *the lowest level in the atmosphere at which the ground surface no longer influences the dependent variables through the turbulent transfer of mass.*

In this study the domain-averaged value of Z_i ($< Z_i >_D$) was used to calculate $< \overline{w''\theta''} >_D$ by interpolation (see Chapter 4), using the surface heat fluxes. The analysis of the heights of the boundary layer showed that the maximum depth of Z_i in the winter case was reached by the NOTOPO events even thought these cases had smaller values of w than the TOPO cases (Figure 4.9). Maximum heights of 1535.32 m at $t = 9$ for the case of NOTOPO $A(x, y, t)$ and 1317.69 m at $t = 5$ for the NOTOPO $\overline{A}(t)$ event were obtained. The TOPO cases had lower heights than the NOTOPO cases (Figure 4.9a). In general, profiles for the winter case showed that the Z_i in the NOTOPO $\overline{A}(t)$ and NOTOPO $A(x, y, t)$ cases started to grow from about 400 m at 0900 LST until they reached their maximums 5 and 9 hours after the initial time, respectively. The TOPO cases showed smoother growth than the NOTOPO events; also Z_i started to decrease after 1600 LST.

In the summer case, all profiles showed similar shapes and heights since they started to grow from the first hour of simulation. Nevertheless, 7 hours after the initial time, the Z_i for the NOTOPO cases continued growing until it reached maximums of about 3500 m at $t = 9$, meanwhile, the TOPO events decreased their rate of growth to only reach maximums around 3000 m (Figure 4.9b). The earth's surface gains more heat in the summer than winter, which explains the seasonal variations in the profiles of Z_i and magnitudes of the heat fluxes. However, the points of interest continue being the atmospheric responses which were simulated when the albedo variability was taken into account over a flat and a complex terrains (NOTOPO and TOPO respectively), for the same climatic conditions. For instance, in the winter case an outstanding feature was that

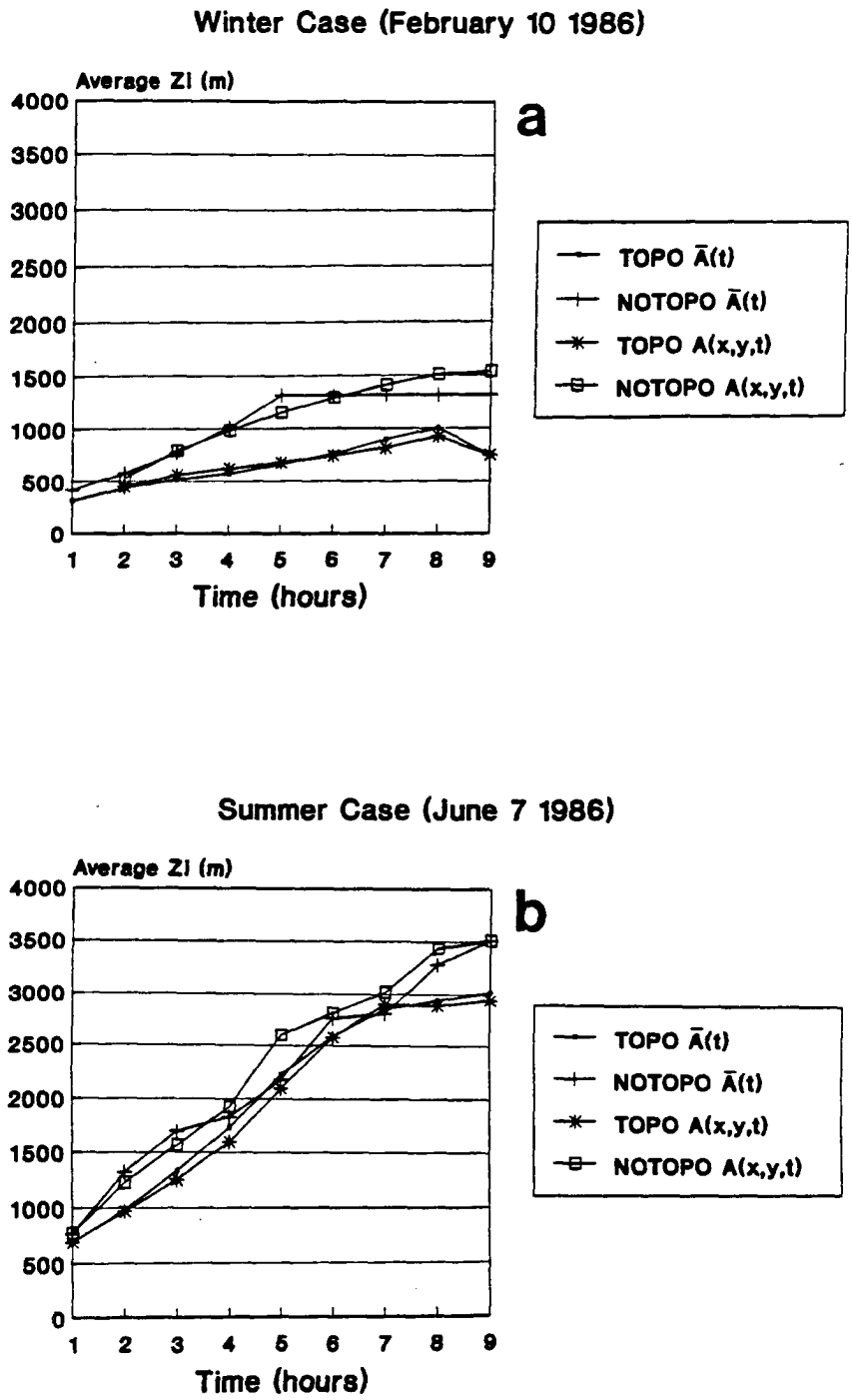

Figure 4.9: Time cross sections of the maximum average Z_i for the entire domain (A_1) for: (a) winter case, and (b) summer case. Here $\overline{A}(t)$ is the mean albedo, $A(x, y, t)$ is the real albedo, TOPO means real topography, and NOTOPO means flat terrain.

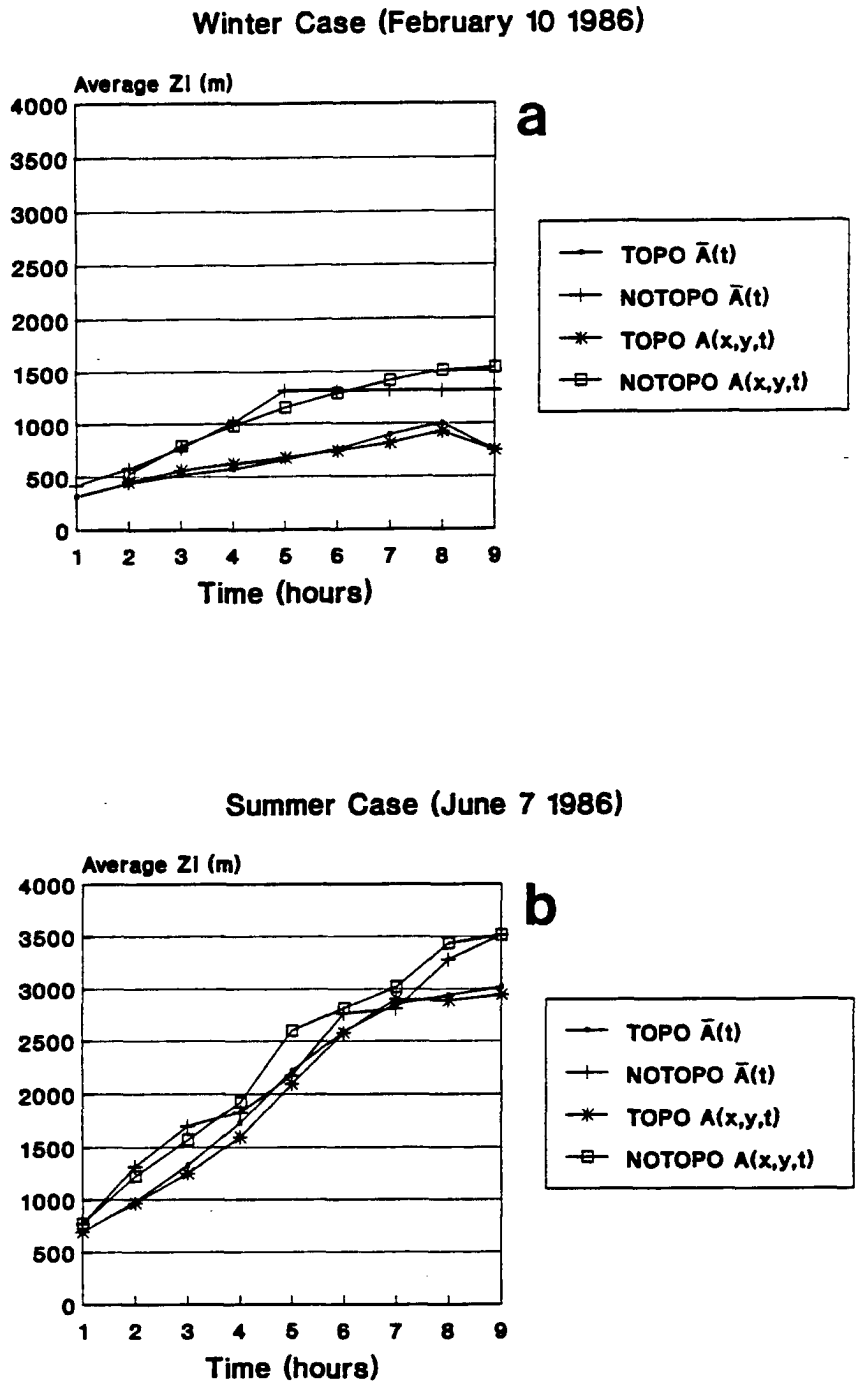

Figure 4.9: Time cross sections of the maximum average Z_i for the entire domain (A_1) for: (a) winter case, and (b) summer case. Here $\overline{A}(t)$ is the mean albedo, $A(x, y, t)$ is the real albedo, TOPO means real topography, and NOTOPO means flat terrain.

the NOTOPO cases resulted with deeper Z_i than the TOPO cases. The winter case had shallower boundary layer depths consistent with the weaker turbulent sensible heat fluxes at this time of the year (Table 4.5). The values of Z_i obtained in the simulations agree the PBL depths observed in the real atmosphere. For instance, it has been found that Z_i can vary from 100 m up to 3000 m or more. However, over some desert areas the PBL can reach heights around 5000 m (Stull, 1988).

Table 4.5: Absolute maximum values of $< Z_i >_D$ for the entire domain (A_1) for winter and summer cases, and time at which they occurred. Here $\overline{A}(t)$ is the mean albedo and $A(x,y,t)$ represents the real albedo.

Case	Topography Type	Albedo	$< Z_i >_{D_{max}}$(m)	Time(LST)
Winter	Complex	$\overline{A}(t)$	1002	1600
Winter	Flat	$\overline{A}(t)$	1317	1300-1700
Winter	Complex	$A(x,y,t)$	924	1600
Winter	Flat	$A(x,y,t)$	1535	1700
Summer	Complex	$\overline{A}(t)$	3016	1700
Summer	Flat	$\overline{A}(t)$	3510	1700
Summer	Complex	$A(x,y,t)$	2941	1700
Summer	Flat	$A(x,y,t)$	3510	1700

Chapter 5

DISCUSSION OF VERTICAL HEAT FLUXES

The vertical distribution of the domain-averaged mesoscale vertical heat flux or resolvable heat flux ($< w'\theta' >_D$) and the domain-averaged subgrid-scale heat flux or turbulent flux ($< \overline{w''\theta''} >_D$) is shown at different model levels in time cross sections for the winter and summer cases. The lower level chosen was $Z_1 = 60$ m and the highest was $Z_7 = 1548$ m (Figures 5.1 to 5.4). The relationships used to calculate the $< w'\theta' >_D$ and the $< \overline{w''\theta''} >_D$ were stated in Chapter 4. To express the heat fluxes in W m^{-2} units, the values obtained from Equations 4.4 and 4.7 were multiplied by the factor $\tilde{\rho}C_p$ (air density and specific heat).

5.1 Vertical Heat Fluxes: Winter Case

Interesting features were found when the mean albedo was included as a function of time but with no spatial variation over complex and flat surfaces. For example, the subgrid-scale fluxes ($< \overline{w''\theta''} >_D$) for the TOPO and NOTOPO cases showed more diurnal symmetry than the profiles of the mesoscale vertical heat fluxes ($< w'\theta' >_D$) (Figure 5.1). The mesoscale heat fluxes in the case NOTOPO $\overline{A}(t)$ were almost negligible. This result is consistent with the fields of $\vec{V}_h$ and w (Tables 4.3 and 4.4). The subgrid-scale fluxes were about three times larger than the values obtained for the mesoscale fluxes for the TOPO cases. The maximum peak reached by the subgrid-scale fluxes was around 145 W m^{-2} for the model level $Z_1 = 60$ m for both topography types. Meanwhile, in the mesoscale heat fluxes the maximum peak was 50 W m^{-2} which occurred for the level $Z_4 = 676$ m for the TOPO case.

The time at which the simulations of heat fluxes reached their maximums also is interesting. In general, the $< \overline{w''\theta''} >_D$ gained its maximums 5 hours after the initial time

(Figures 5.1b and d); and the $< w'\theta' >_D$ reached maximum values 1 to 2 hours later than the subgrid-scale fluxes, about 6 and 7 hours after the initial time (Figures 5.1a and c). This difference in time between these two heat fluxes in reaching the maximums occurred because the simulated atmosphere needs time to develop first, a deep boundary layer and after that, vertical motions to carry the sensible heat from the surface to lower parts of the atmosphere through the result mesoscale circulations.

For the cases where the albedo varied as a function of space and time $[A(x, y, t)]$, the profiles of vertical heat fluxes also showed important features. For instance, they showed more diurnal symmetry (along the axe x) than those developed in the simulations where the mean albedo was defined as a function of time (Figure 5.2). In these cases, we observed again that $< \overline{w''\theta''} >_D$ reached maximum values around three times larger than the mesoscale heat fluxes. For example, the subgrid-scale heat fluxes gained maximum values of about 150 W m^{-2} for level Z_1. Meanwhile, the mesoscale heat fluxes reached maximum peaks around 60 W m^{-2}, mainly for the model levels of $Z_3 = 346$ m and $Z_4 = 676$ m. In general, the subgrid-scale heat fluxes reached its maximum about 5 hours after the initial time; the $< w'\theta' >_D$ developed their maximums 1 to 2 hours later ($t = 6$ and $t = 7$). The TOPO $A(x, y, t)$ case for the mesoscale heat fluxes displayed less diurnal symmetry in its curves than the other events. The curves where the real topography (TOPO) was taken into account showed greater values than the NOTOPO $A(x, y, t)$ cases (flat terrain). In this case [NOTOPO $A(x, y, t)$], the atmosphere simulated took two to three hours to develop significant heat fluxes before reaching the maximum (Figure 5.2c).

At first sight, and based on results from winter simulations, we can say that the domain-averaged production of mesoscale vertical heat fluxes was weak for that season, as contrasted with the subgrid-scale turbulent fluxes. However, recall that the fluxes were averaged, so, weak does not imply unimportant since in some regions of the domain the differences in heating were capable of generate significant vertical motions that formed coherent ascent cells with depths up to 2 km. In addition, the topography effects seem to also play an important role that works together with the albedo variability to enhance mesoscale circulations.

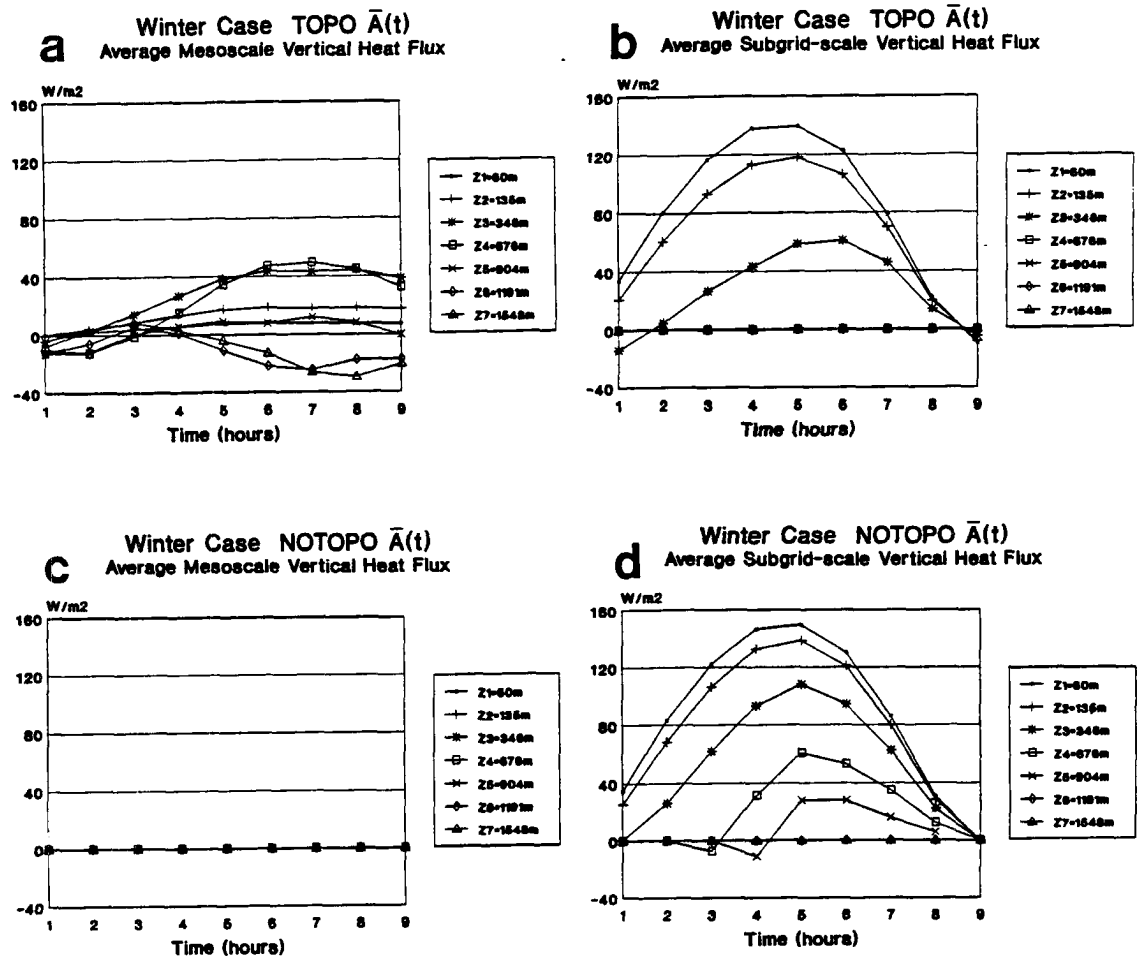

Figure 5.1: Time cross sections of the domain-averaged mesoscale vertical heat fluxes and domain-averaged subgrid-scale heat fluxes for area A_1 for the winter case at model levels $Z_1 = 60$ m, $Z_2 = 135$ m, $Z_3 = 346$ m, $Z_4 = 676$ m, $Z_5 = 904$ m, $Z_6 = 1191$ m, and $Z_7 = 1548$ m for: (a)-(b) TOPO $\overline{A}(t)$ and (c)-(d) NOTOPO $\overline{A}(t)$. Here TOPO represents the real terrain, NOTOPO means flat surface, and $\overline{A}(t)$ is the mean albedo.

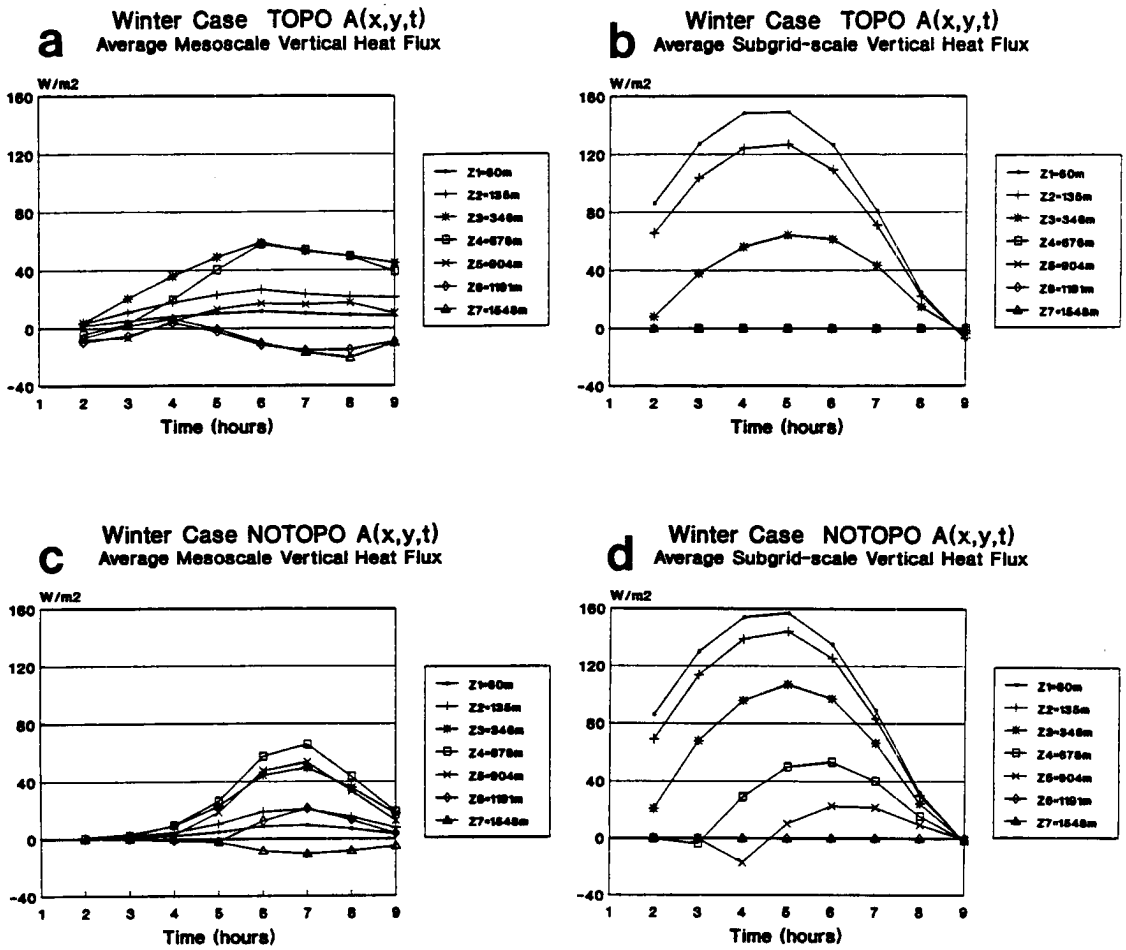

Figure 5.2: Time cross sections of the domain-averaged mesoscale vertical heat fluxes and domain-averaged subgrid-scale heat fluxes for area A_1 for the winter case at model levels Z_1 = 60 m, Z_2 = 135 m, Z_3 = 346 m, Z_4 = 676 m, Z_5 = 904 m, Z_6 = 1191 m, and Z_7 = 1548 m for: (a)-(b) TOPO $A(x, y, t)$ and (c)-(d) NOTOPO $A(x, y, t)$. Here TOPO means real topography, NOTOPO represents flat terrain, and $A(x, y, t)$ is the real albedo.

5.2 Vertical Heat Fluxes: Summer Case

In general, summer heat fluxes simulated for mean albedo as a function of time but with no spatial variation reached greater values than those simulated in the winter case. For instance, the subgrid-scale heat fluxes reached values of the order of 385 W m^{-2} for the TOPO and NOTOPO cases (Figures 5.3b and d). Meanwhile, the mesoscale heat fluxes achieved maxima around 250 W m^{-2} and 275 W m^{-2} for the cases TOPO and NOTOPO, respectively (Figures 5.3a and c). These values make a difference of about 100 W m^{-2} between the two types of heat fluxes. In reference to the shapes, the $< \overline{w''\theta''} >_D$ showed similar profiles to those shown for the winter case. In the case of mesoscale heat fluxes, the TOPO event depicted more diurnal symmetry than the NOTOPO case. For example, in the NOTOPO case, the profiles of mesoscale heat fluxes for the first 5 hours of simulation did not show any significant activity (as shown in the horizontal and vertical wind fields for this event).

Concerning the time at which the maximum peaks were occurred, the subgrid-scale heat fluxes reached their maxima four hours after the initial time (1200 LST). This time was reached for model levels closer to the earth's surface (Z_1, Z_2, and Z_3). The rest of the levels gained maximum peaks at 1300 LST and 1400 LST. Moreover, the $< w'\theta' >_D$ had maxima 5 and 6 hours after the initial time.

Cases in which the albedo was set up as a function of space and time obtained the most diurnal symmetry patterns from all simulations carried out for both seasons (Figure 5.4). The subgrid-scale heat fluxes had substantial values during the first few hours. The maxima were shifted toward higher heights at later times as the boundary layer increased in depth. The subgrid-scale heat fluxes obtained maxima of about 385 W m^{-2} for the level Z_1, which is the same intensity reached when the mean albedo was varied as a function of time for both flat and complex terrain characteristics. On the other hand, the magnitude of the mesoscale heat fluxes for $A(x, y, t)$ gained maximum peaks of about 265 W m^{-2} at level $Z_4 = 676$ m for the NOTOPO event and around 285 W m^{-2} in the TOPO case, also at the same model level. Notice that the difference in magnitude between the $< \overline{w''\theta''} >_D$

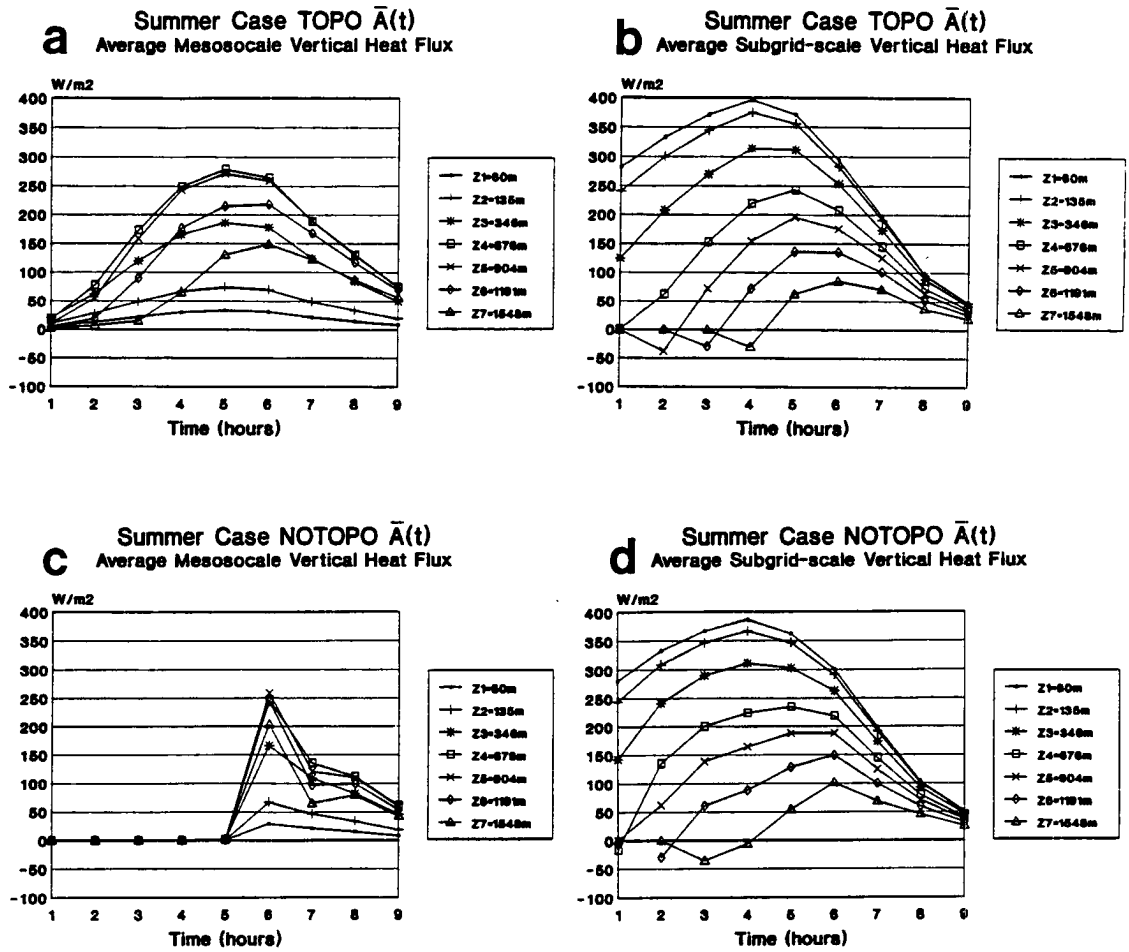

Figure 5.3: Time cross sections of the domain-averaged mesoscale and subgrid-scale vertical heat fluxes for the summer case for area A_1 at model levels $Z_1 = 60$ m, $Z_2 = 135$ m, $Z_3 = 346$ m, $Z_4 = 676$ m, $Z_5 = 904$ m, $Z_6 = 1191$ m, and $Z_7 = 1548$ m for: (a)-(b) TOPO $\overline{A}(t)$ and (c)-(d) NOTOPO $\overline{A}(t)$. Here TOPO means real topography, NOTOPO represents flat terrain, and $\overline{A}(t)$ is the mean albedo.

and $< w'\theta' >_D$ is again about the order of 100 W m^{-2}. The maxima of the subgrid-scale heat fluxes were reached at 1200 LST for the first three levels. André et al. (1990) showed approximately this time for the surface heat fluxes in the HAPEX-MOBILHY Programme (Figure 2.5). Also, they observed and obtained in the computation maximum values of latent heat flux of about 400 W m^{-2}; similar values were found in this study for the summer case. With reference to the mesoscale heat fluxes, the maximum peaks were obtained at 1300 LST for all model levels, with exception of the level $Z_7 = 1548$ m which achieved its maximum at 1400 LST. In the NOTOPO case most levels showed maximums 5 hours after the initial time (1300 LST), but the levels Z_6 and Z_7 gained their maximum peaks at 1400 LST.

Notice here again how the fluxes had slower responses when the albedo varied as a function of space and time over a flat surface, than those obtained over complex terrain in which the profiles displayed significant values since the first hour of simulation. This means that the topography enhances the heat fluxes in the case where the albedo varied over the actual terrain (TOPO). An important conclusion is that the terrain and albedo variations independently produce mesoscale fluxes that are on the same order, but at higher model levels, than simulated for the turbulent heat fluxes.

Tables 5.1 and 5.2 show absolute maximum values of the domain-averaged mesoscale vertical heat fluxes ($< w'\theta' >_D$) and subgrid-scale vertical heat fluxes ($< \overline{w''\theta''} >_D$) which were obtained in the simulations. Also, they show the heights and time at which they occurred for the winter and summer cases.

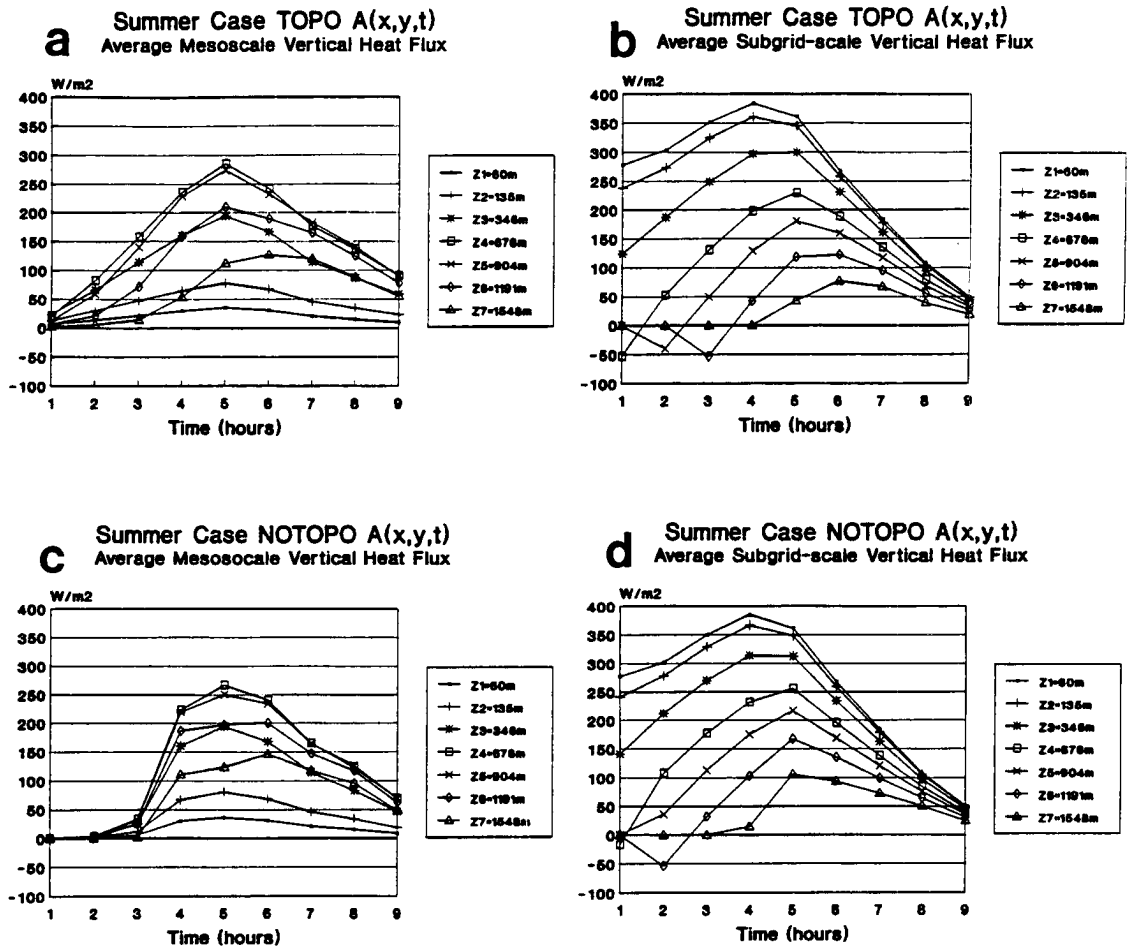

Figure 5.4: Time cross sections of the domain-averaged mesoscale vertical heat fluxes and the domain-averaged subgrid-scale heat fluxes for area A_1 for the summer case at model levels $Z_1 = 60$ m, $Z_2 = 135$ m, $Z_3 = 346$ m, $Z_4 = 676$ m, $Z_5 = 904$ m, $Z_6 = 1191$ m, and $Z_7 = 1548$ m for: (a)-(b) TOPO $A(x, y, t)$ and (c)-(d) NOTOPO $A(x, y, t)$. Here TOPO represents real topography, NOTOPO means flat terrain, and $A(x, y, t)$ is the real albedo.

Table 5.1: Absolute maximum values of the domain-averaged vertical heat fluxes ($< w'\theta' >_{D_{max}}$) for the winter and summer cases over the entire domain (A_1). Also, heights (Z) and time at which they were occurred. Here $\overline{A}(t)$ is the mean albedo and $A(x,y,t)$ is the real albedo.

Case	Topo.Type	Albedo	$< w'\theta' >_{D_{max}}$(W m^{-2})	Z(m)	Time(LST)
Winter	Complex	$\overline{A}(t)$	49.40	676	1500
Winter	Flat	$\overline{A}(t)$	00.04	676	1700
Winter	Complex	$A(x,y,t)$	58.95	346	1400
Winter	Flat	$A(x,y,t)$	65.63	676	1500
Summer	Complex	$\overline{A}(t)$	279.38	676	1300
Summer	Flat	$\overline{A}(t)$	246.68	676	1400
Summer	Complex	$A(x,y,t)$	285.87	676	1300
Summer	Flat	$A(x,y,t)$	267.31	676	1300

Table 5.2: Absolute maximum values of the domain-averaged subgrid-scale heat fluxes ($< \overline{w''\theta''} >_{D_{max}}$) for the winter and summer cases over the entire domain (A_1). Also, heights (Z) and time at which they were occurred. Here $\overline{A}(t)$ is the mean albedo and $A(x,y,t)$ is the real albedo.

Case	Topo.Type	Albedo	$< \overline{w''\theta''} >_{D_{max}}$(W m^{-2})	Z(m)	Time(LST)
Winter	Complex	$\overline{A}(t)$	139.34	60	1300
Winter	Flat	$\overline{A}(t)$	149.16	60	1300
Winter	Complex	$A(x,y,t)$	149.10	60	1300
Winter	Flat	$A(x,y,t)$	157.09	60	1300
Summer	Complex	$\overline{A}(t)$	396.51	60	1200
Summer	Flat	$\overline{A}(t)$	386.84	60	1200
Summer	Complex	$A(x,y,t)$	383.55	60	1200
Summer	Flat	$A(x,y,t)$	385.46	60	1200

Chapter 6

SUMMARY AND CONCLUSIONS

6.1 Summary

Real albedo data from a region of 100×100 km^2 located in the Coconino Plateau in northern Arizona were used in RAMS to simulate the effects that mesoscale variations in land surface albedo have on the averaged vertical heat fluxes. The results showed that domain-averaged mesoscale and subgrid-scale vertical heat fluxes ($< w'\theta' >_D$ and $< \overline{w''\theta''} >_D$ respectively) both had important contribution to the sensible heating of the atmosphere. For example, in the winter case the maximum values obtained for $< w'\theta' >_D$ were around 60 W m^{-2}; for $< \overline{w''\theta''} >_D$ about 150 W m^{-2}. In the summer, the mesoscale heat fluxes had maxima of about 270 W m^{-2}, and the subgrid-scale heat fluxes reached maximum peaks of around 385 W m^{-2}. Thus, in the summer case, the total vertical heat fluxes were approximately three times larger than those generated in the winter case. Therefore, this work demonstrates the importance that the albedo and terrain variability have in the generation of vertical heat fluxes and consequently in the weather and climate. In my opinion, these fluxes need to be included in the General Circulation Models (GCM) and in operational numerical weather prediction models (NWPM) as well, because the actual results of those models do not resolve yet these mesoscale features due to albedo and terrain variability. For instance, in the NWPM for operational use, the forecast of airports, which are really points on a weather map, it's a difficult task due to lack of appropriate resolution of the mesoscale meteorology elements that could give us more information for a better weather predictions.

More specific conclusions about the vertical heat fluxes are given in the next section.

6.2 Conclusions

- Albedo and terrain variability work together to enhance in important ways the production of heat fluxes and the development of mesoscale circulations. In general, these cases [$A(x, y, t)$ and TOPO] achieved the greatest values of vertical heat fluxes.
- The terrain and albedo variations, independently produce mesoscale vertical heat fluxes that are on the same order, but higher model levels, than simulated for the turbulent heat fluxes.
- Both types of vertical heat fluxes showed in general, similar shapes but with different vertical structure.
- The time of maximum occurrence of $< w'\theta' >_D$ was in general 1 or 2 hours later than the time at which the $< \overline{w''\theta''} >_D$ occurred (1200-1300 LST).
- In the winter case the maximum values reached for the mesoscale heat fluxes were about 60 W m^{-2}, while the subgrid-scale heat fluxes were around 150 W m^{-2}.
- In the summer case the maximum peaks achieved values of about 270 W m^{-2} for the mesoscale fluxes, with maximum values of 385 W m^{-2} for the subgrid-scale fluxes.

6.3 Future Work

Additional regions of the earth's surface which consider different elevations and latitude locations, and diverse albedo patterns should be considered. Also, the relative influence of the landscape effects such as surface wetness and transpiration patterns from vegetation need to be analyzed.

REFERENCES

André, J.-C., J.-P. Goutorbe, and A. Perrier, 1986: HAPEX-MOBILHY: A Hydrologic Atmospheric Experiment for the Study of Water Budget and Evaporation Flux at the Climate Scale. *Bull. Amer. Meteor. Soc.*, **67**, 138-144.

André, J.-C., P. Bougeault, and J.-P. Goutorbe, 1990: Regional Estimates of Heat and Evaporation Fluxes over Non-Homogeneous Terrain. Examples from the HAPEX-MOBILHY Programme. *Bound.-Layer Meteor.*, **50**, 77-108.

Brook, R.R., 1978: The Influence of Water Vapor Fluctuations on Turbulent Fluxes. *Bound.-Layer Meteor.*, **15**, 481-487.

Businger, J.A., 1982: The Fluxes of Specific Enthalpy, Sensible Heat and Latent Heat near the Earth's Surface. *J. Atmos. Sci.*, **39**, 1889-1892.

Conover, J.H., 1965: Cloud and Terrestrial Albedo Determinations from TIROS Satellite Pictures. *J. Appl. Meteor.*, **4**, 378-386.

Dalu, G.A. and R.A. Pielke, 1992: Vertical Heat Fluxes Generated by Mesoscale Atmospheric Flow Induced by Thermal Inhomogeneities in the PBL. *J. Atmos. Sci.*, (in press).

Deardorff, J.W., 1966: The Counter-Gradient Heat Flux in the Lower Atmosphere and in the Laboratory. *J. Atmos. Sci.*, **23**, 503-506.

Deardorff, J.W., 1972: Parameterization of the Planetary Boundary Layer for Use in General Circulation Models. *Mon. Wea. Rev.*, **100**, 93-106.

Deardorff, J.W., 1974: Three-Dimensional Numerical Study of the Height and Mean Structure of a Heated Planetary Boundary Layer. *Bound.-Layer Meteor.*, **7**, 81-106.

Charney, J.G., 1975: Dynamics of Deserts and Drought in the Sahel. *Quart. J. Roy. Meteor. Soc.*, **101**, 193-202.

Ellis, J.S. and T.H. Vonder Haar, 1976: Zonal Average Earth Radiation Budget Measurements From Satellites For Climate Studies. Atmospheric Science Paper No. 240, Colorado State University.

Frank, W.M. and G.D. Emmitt, 1981: Computation of Vertical Total Energy Fluxes in a Moist Atmosphere. *Bound.-Layer Meteor.*, **21**, 223-230.

Fritz, S., 1948: The Albedo of the Ground and Atmosphere. *Bull. Amer. Meteor. Soc.*, **29**, 303-312.

Gadd, A.J. and J.F. Keers, 1970: Surface Exchanges of Sensible and Latent Heat in a 10-level Model Atmosphere. *Quart. J. Roy. Meteor. Soc.*, **96**, 297-308.

Gautier, C., G. Diak, and S. Masse, 1980: A Simple Physical Model to Estimate Incident Solar Radiation at the Surface from GOES Satellite Data. *J. Appl. Meteor.*, **19**, 1005-1012.

Hadfield, M.G., W.R. Cotton, and R.A. Pielke, 1991: Large-Eddy Simulations of Thermally Forced Circulations in the Convective Boundary Layer. Part I: A Small-Scale Circulation with Zero Wind. *Bound.-Layer Meteor.*, **57**, 79-114.

Idso, S.B., R.D. Jackson, R.J. Reginato, B.A. Kimball, and F.S. Nakayama, 1975: The Dependence of Bare Soil Albedo on Soil Water Content. *J. Appl. Meteor.*, **14**, 109-113.

Kelly, P.M., P.D. Jones, C.B. Sear, B.S. G. Cherry, and R.K. Tavakol, 1982: Variations in Surface Air Temperatures: Part 2, Arctic Regions, 1881-1980. *Mon. Wea. Rev.*, **110**, 71-83.

Klaassen, W., 1992: Average Fluxes from Heterogeneous Vegetated Regions. *Bound.-Layer Meteor.*, **58**, 329-354.

Kuhn, P.M. and V.E. Suomi, 1958: Airborne Observations of Albedo with a Beam Reflector. *J. Meteor.*, **15**, 172-174.

Kukla, G.J. and H.J. Kukla, 1974: Increased Surface Albedo in the Northern Hemisphere. *Science*, **183**, 709-714.

Kung, E.C., R.A. Bryson, and D.H. Lenshow, 1964: Study of Continental Surface Albedo on the Basis of Flight Measurements and Structure of the Earth's Surface Cover over North America. *Mon. Wea. Rev.*, **92**, 543-564.

Lipton, A.E., 1991: Effects of Slope and Aspect Variation on Satellite Surface Temperature Retrievals and Mesoscale Analysis in Mountainous Terrain. *J. Appl. Meteor.*, **31**, 255-264.

Louis, J.-F., 1979: A Parametric Model of Vertical Eddy Fluxes in the Atmosphere. *Bound.-Layer Meteor.*, **17**, 187-202.

MacCracken, M.C. and M.I. Budyko, 1990: Prospects for Future Climate. A Special US/USSR Report on Climate and Climate Change, 235 pp. US Department of Energy and NOAA.

McCumber, M.C. and R.A. Pielke, 1981: Simulation of the Effects of Surface Fluxes of Heat and Moisture in a Mesoscale Numerical Model. 1. Soil Layer. *J. Geophys. Res.*, **86**, 9929-9938.

Mahrer, Y. and R.A. Pielke, 1978: The Meteorological Effect of Changes in Surface Albedo and Moisture. *Israel Meteor. Research Papers*, **2**, 55-70.

Mahrt, L., C. Berthou, P. Marquet, and J.C. André, 1986: Time-averaging the Flux-profile relationship. *Annales Geophysicae. 4, B*, 4, 411-416.

Mahrt, L., 1987: Grid-Averaged Surface Fluxes. *Mon. Wea. Rev.*, **115**, 1550-1560.

Mekler, Y. and J.H. Joseph, 1983: Direct Determination of Surface Albedo from Satellite Imagery. *J. Climate Appl. Meteor.*, **22**, 530-536.

Minnis, P. and E.F. Harrison, 1984a: Diurnal Variability of Regional Cloud and Clear-Sky Radiative Parameters Derived from GOES Data. Part I: Analysis Method. *J. Climate Appl. Meteor.*, **23**, 993-1011.

Minnis, P. and E.F. Harrison, 1984b: Diurnal Variability of Regional Cloud and Clear-Sky Radiative Parameters Derived from GOES Data. Part II: November 1978 Cloud Distribution. *J. Climate Appl. Meteor.*, **23**, 1012-1031.

Minnis, P. and E.F. Harrison, 1984c: Diurnal Variability of Regional Cloud and Clear-Sky Radiative Parameters Derived from GOES Data. Part III: November 1978 Radiative Parameters. *J. Climate Appl. Meteor.*, **23**, 1032-1051.

NASA Conference Publication 2100, 1978: Earth Radiation Budget Science 1978. *Proceedings of a workshop held at Williamsburg, Virginia.* March 28-30, 1978. 72 pp.

NASA ERBE, 1985: Earth Radiation Budget Experiment (ERBE) Data Management System. The Regional, Zonal and Global Averages, S-4, User's Guide. ERBE 3-3-12-3-85-1-10. NASA Langley Research Center, Hampton, Virginia 23665.

Nicholls, S. and F.B. Smith, 1982: On the Definition of the Flux of Sensible Heat. *Bound.-Layer Meteor.*, **24**, 121-127.

Orlansky, I., 1975: A Rational Subdivision of Scales for Atmospheric Processes. *Bull. Amer. Meteor. Soc.*, **56**, 527-530.

Otterman, J., 1974: Baring High-Albedo Soils Overgrazing: A Hypothesized Desertification Mechanism. *Science*, **186**, 531-533.

Otterman, J., 1977: Anthropogenic Impact on the Albedo of the Earth. *Climatic Change*, **1**, 137-155.

Otterman, J., 1981: Satellite and Field Studies of Man's Impact on the Surface in Arid Regions. *Tellus*, **33**, 68-77.

Otterman, J., 1984: Albedo of a Forest Modeled as a Plane with Dense Protrusions. *J. Climate Appl. Meteor.*, **23**, 297-307.

Otterman, J. and R.S. Fraser, 1976: Earth-Atmosphere System and Surface Reflectivities in Arid Regions from LANDSAT MSS Data. *Remote Sensing Environment*, **5**, 247-266.

Otterman, J. and C.J. Tucker, 1985: Satellite Measurements of Surface Albedo and Temperatures in Semi-Desert. *J. Climate Appl. Meteor.*, **24**, 228-235.

Pielke, R.A., 1974: A Three-dimensional Numerical Model of the Sea Breezes over South Florida. *Mon. Wea. Rev.*, **102**, 115-139.

Pielke, R.A., 1984: *Mesoscale Meteorological Modeling.* Academic Press, 612 pp.

Pielke, R.A. and R. Avissar, 1990: Influence of Landscape Structure on Local and Regional Climate. *Landscape Ecology*, **4**, 133-155.

Pielke, R.A., G.A. Dalu, J.S. Snook, T.J. Lee, and T.G.F. Kittel, 1991: Nonlinear Influence of Mesoscale Land Use on Weather and Climate. *J. Climate*, 4, 1053-1069.

Pielke, R.A., W.R. Cotton, R.L. Walko, C.J. Tremback, W.A. Lyons, L.D. Grasso, M.E. Nicholls, M.D. Moran, D.A. Wesley, T.J. Lee, and J.H. Copeland, 1992: A Comprehensive Meteorological Modeling System - RAMS. *Meteor. Atmos. Phys.*, (accepted).

Pinker, R.T., J.A. Ewing, and A. Gruber, 1986: Diurnal Variation of Planetary Radiation Budget Parameters from Geostationary Satellites. *J. Climatology*, **6**, 389-403.

Pinty, B., G. Szejwach, and J. Stum, 1985: Surface Albedo over the Sahel from METEOSAT Radiances. *J. Climate Appl. Meteor.*, **24**, 108-113.

Rockwood, A.A. and S.K. Cox, 1978: Satellite Infrared Surface Albedo Over Northwestern Africa. *J. Atmos. Sci.*, **35**, 513-522.

Sikula, G.J. and T.H. Vonder Haar, 1972: Very Short Range Local Area Weather Forecasting Using Measurements From Geosynchronous Meteorological Satellites. Atmospheric Science Paper No. 185, Colorado State University (CSU). 73 pp.

Stull, R.B., 1988: An Introduction to Boundary Layer Meteorology. Kluwer Academic Publishers, P.O. Box 17, 3300 AA Dordrecht, The Netherlands, 666 pp.

Sud, Y.C. and W.E. Smith, 1984: Ensemble Formulation of Surface Fluxes and Improvement in Evapotranspiration and Cloud Parameterizations in a GCM. *Bound.-Layer Meteor.*, **29**, 185-210.

Tremback, C.J. and R. Kessler, 1985: A Surface Temperature and Moisture Parameterization for Use in Mesoscale Numerical Models. *7th Conference on Numerical Weather Prediction*, AMS, Montreal, June 17-20, 355-358.

Tremback, C., G. Tripoli, R.W. Arritt, W.R. Cotton, and R.A. Pielke, 1986: The Regional Atmospheric Modeling System. *Proceedings of the International Conference on Development and Application of Computer Technique to Environmental Studies.*, 601-607.

Tripoli G.J. and W.R. Cotton, 1982: The Colorado State University Three-Dimensional Cloud/Mesoscale Model-1982. Part I: General Theoretical Framework and Sensitivity Experiments. *J. de Recherches Atmospheriques.*, **16**, 185-219.

Troen, I.B. and L. Mahrt, 1986: A Simple Model of the Atmospheric Boundary Layer; Sensitivity to Surface Evaporation. *Bound.-Layer Meteor.*, **37**, 129-148.

Vonder Haar, T.H. and J.S. Ellis, 1974: Atlas of Radiation Budget Measurements From Satellites (1962-1970). Atmospheric Science Department at Colorado State University, Fort Collins, CO 80523.

Vonder Haar, T.H., 1991: AT 622 Lecture Notes. Department of Atmospheric Science at Colorado State University, Fort Collins, CO 80523.

Wetzel, P.J. and J.-T. Chang, 1987: Concerning the Relationship between Evapotranspiration and Soil Moisture. *J. Climate Appl. Meteor.*, **26**, 18-27.

Wetzel, P.J. and R.H. Woodward, 1987: Soil Moisture Estimation Using GOES-VISSR Infrared Data: A case Study with a Simple Statistical Method. *J. Climate Appl. Meteor.*, **26**, 107-117.

Wetzel, P.J., 1990: A Simple Parcel Method for Prediction of Cumulus Onset and Area-Averaged Cloud Amount over Heterogeneous Land Surfaces. *J. Appl. Meteor.*, **29**, 516-523.

Pinker, R.T., J.A. Ewing, and A. Gruber, 1986: Diurnal Variation of Planetary Radiation Budget Parameters from Geostationary Satellites. *J. Climatology*, **6**, 389-403.

Pinty, B., G. Szejwach, and J. Stum, 1985: Surface Albedo over the Sahel from METEOSAT Radiances. *J. Climate Appl. Meteor.*, **24**, 108-113.

Rockwood, A.A. and S.K. Cox, 1978: Satellite Infrared Surface Albedo Over Northwestern Africa. *J. Atmos. Sci.*, **35**, 513-522.

Sikula, G.J. and T.H. Vonder Haar, 1972: Very Short Range Local Area Weather Forecasting Using Measurements From Geosynchronous Meteorological Satellites. Atmospheric Science Paper No. 185, Colorado State University (CSU). 73 pp.

Stull, R.B., 1988: An Introduction to Boundary Layer Meteorology. Kluwer Academic Publishers, P.O. Box 17, 3300 AA Dordrecht, The Netherlands, 666 pp.

Sud, Y.C. and W.E. Smith, 1984: Ensemble Formulation of Surface Fluxes and Improvement in Evapotranspiration and Cloud Parameterizations in a GCM. *Bound.-Layer Meteor.*, **29**, 185-210.

Tremback, C.J. and R. Kessler, 1985: A Surface Temperature and Moisture Parameterization for Use in Mesoscale Numerical Models. *7th Conference on Numerical Weather Prediction*, AMS, Montreal, June 17-20, 355-358.

Tremback, C., G. Tripoli, R.W. Arritt, W.R. Cotton, and R.A. Pielke, 1986: The Regional Atmospheric Modeling System. *Proceedings of the International Conference on Development and Application of Computer Technique to Environmental Studies.*, 601-607.

Tripoli G.J. and W.R. Cotton, 1982: The Colorado State University Three-Dimensional Cloud/Mesoscale Model-1982. Part I: General Theoretical Framework and Sensitivity Experiments. *J. de Recherches Atmospheriques.*, **16**, 185-219.

Troen, I.B. and L. Mahrt, 1986: A Simple Model of the Atmospheric Boundary Layer; Sensitivity to Surface Evaporation. *Bound.-Layer Meteor.*, **37**, 129-148.

Vonder Haar, T.H. and J.S. Ellis, 1974: Atlas of Radiation Budget Measurements From Satellites (1962-1970). Atmospheric Science Department at Colorado State University, Fort Collins, CO 80523.

Vonder Haar, T.H., 1991: AT 622 Lecture Notes. Department of Atmospheric Science at Colorado State University, Fort Collins, CO 80523.

Wetzel, P.J. and J.-T. Chang, 1987: Concerning the Relationship between Evapotranspiration and Soil Moisture. *J. Climate Appl. Meteor.*, **26**, 18-27.

Wetzel, P.J. and R.H. Woodward, 1987: Soil Moisture Estimation Using GOES-VISSR Infrared Data: A case Study with a Simple Statistical Method. *J. Climate Appl. Meteor.*, **26**, 107-117.

Wetzel, P.J., 1990: A Simple Parcel Method for Prediction of Cumulus Onset and Area-Averaged Cloud Amount over Heterogeneous Land Surfaces. *J. Appl. Meteor.*, **29**, 516-523.